ABSTRACT

Title of Dissertation: COMPUTATIONAL STUDIES OF MEMBRANE MODELS AND THEIR INTERACTION WITH A PERIPHERAL PROTEIN IN YEAST, AND DISRUPTION OF THE WATER-OIL INTERFACE BY A HYDROTROPE

Viviana Monje-Galvan, Doctor of Philosophy, 2017

Dissertation directed by: Dr. Jeffery B. Klauda
Associate Professor
Department of Chemical and Biomolecular Engineering

Biological and non-biological interfaces were studied using all-atom molecular dynamics simulations to understand the interaction between different molecules. Simulation were run to analyze the dynamics and structure of cell membrane models and their interaction with a protein. Additionally, the effect of a small alcohol at the water-oil interface was examined as a model for amphiphilic molecules, which are relevant in chemistry and biology.

Previously developed organelle-specific membrane models for yeast *S. cerevisiae* (*Biochem*. **54**:6852-6861) were improved to reflect leaflet asymmetry of the trans-Golgi network (TGN) and plasma membranes. Each model was built based on experimental trends to study interleaflet coupling and lipid clustering. The (previous)

symmetric endoplasmic reticulum (ER) and TGN models were further used to study the effect of sterol type in the structural properties of the membrane, and lipid-protein interactions with a lipid transport protein in yeast, Osh4. The protein's phenylalanine loop was determined to have the strongest interaction with the bilayer among the protein's six binding regions (*BBA-Biomemb.* **1858**:1584-1593). The protein's lid, the ALPS-like motif (Amphipathic Lipid Packing Sensor), was also simulated with simple (2-lipid) bilayers and with the symmetric ER and TGN models. Key residues for peptide-membrane interaction were identified based on their interaction energy, and a time scale of ~1μs determined for stable peptide binding.

The interfacial dynamics between water and cyclohexane were examined in the presence of a hydrotrope - an amphiphilic molecule that reduces the interfacial tension between two liquids. Simulations were run for water-cyclohexane systems and all butanol isomers separately to understand the effect of this hydrotrope's chemical structure on the interface. The results reproduced experimental data trends, showing that a hydrotrope concentration of as little as 0.6mol% in the aqueous phase reduces the interfacial tension to nearly half the value of a binary water-cyclohexane mixture. *Tert*-butanol was further compared with experimental studies showing that at low concentrations (< 10mol%) the simulations accurately reproduce experimental data. In addition, theoretical correlations from simulation data show the system follows van der Waals theory of smooth interfaces, and describe the crossover behavior of this hydrotrope from surfactant-like to co-solvent based on its concentration in solution.

COMPUTATIONAL STUDIES OF MEMBRANE MODELS AND THEIR INTERACTION WITH A PERIPHERAL PROTEIN IN YEAST AND DISRUPTION OF THE WATER-OIL INTERFACE BY A HYDROTROPE

by

Viviana Monje-Galvan

Dissertation submitted to the Faculty of the Graduate School of the
University of Maryland, College Park, in partial fulfillment
of the requirements for the degree of
Doctor of Philosophy
2017

Advisory Committee:
Professor Jeffery B. Klauda, Chair
Professor Mikhail Anisimov
Professor Panagiotis Dimitrakopoulos
Professor Amy Karlsson
Professor Garegin Papoian

Dedication

I dedicate my PhD Dissertation to my husband for his encouragement, especially during the last months of my studies, and to my son for his cheering smile in my busiest days.

Acknowledgements

I thank my adviser, Dr. Jeffery Klauda, for his mentorship and ever useful discussions throughout the duration of my PhD training. I thank him for giving the opportunity to grow as a scientist by supporting my attendance to scientific conferences and guiding me patiently as I progressed in my studies. His willingness to discuss anything from career paths to challenges in my research projects created a reassuring environment for me to become the scientists I am today.

I also acknowledge the Center for Minorities in Science and Engineering of the University of Maryland for their support and motivation past the duration of my LSAMP Bridge to the Doctorate Fellowship at the beginning of my training.

Finally, I thank the staff and faculty members of the Chemical and Biomolecular Engineering Department at the A. James Clark School of Engineering. They have all seen me grow as a person as well as a researcher since I started my undergraduate studies at this institution; their helping hand and motivation have meant a lot throughout my studies. A special thank you to Dr. Mikhail Anisimov for our discussions on interfacial dynamics and the collaboration stablished through him with international researchers for the work of the water-oil interface.

Table of Contents

List of Tables

List of Figures

List of Abbreviations

CHOL Cholesterol

DOPC 1,2-dioleoyl-sn-glycero-3-phosphocholine

DPPC 1,2-dipalmitoyl-sn-glycero-3-phosphocholine

DYPC 3-palmitoleoyl-2-palmitoleoyl-D-glycero-1-Phosphatidylcholine

DYPE 3-palmitoleoyl-2-palmitoleoyl-D-glycero-1-Phosphatidylethanolamine

EDP Electron density profile

ER Endoplasmic reticulum

ERG Ergosterol

FA Fatty acid

FOC Frequency of contact

FF Force field

IPC Inositol phosphoceramide

Ld Liquid disordered domain in membranes

Lo Liquid ordered domain in membranes

LTP Lipid transport protein

MD Molecular dynamics

M(IP)2C Mannose-(inositol-P)2-ceramide

PA Phosphatidic acid

PBC Periodic boundary conditions

PC Phosphatidylcholine

PE Phosphatidylethanolamine

PI Phosphatidylinositol

PM Plasma membrane

PME Particle mesh Ewald

POPA 3-palmitoyl-2-oleoyl-D-glycero-1-Phosphatidic acid

POPE 1-palmitoyl-2-oleoyl-sn-glycero-3-phosphoethanolamine

POPI 1-palmitoyl-2-pleoyl-inositol

POPS 3-palmitoyl-2-oleoyl-D-glycero-1-Phosphatidylserine

PS Phosphatidylserine

PYPE 3-palmitoyl-2-palmitoleoyl-D-glycero-1-phosphatidylethanolamine

PYPI 1-palmitoyl-2-palmitoleoyl-sn-glycero-3-phosphoinositol

SA Surface area per lipid

SANS Small angle neutron scattering

SAXS Small angle X-ray scattering

SCD Deuterium order parameters

SDP Scattering density profiles

SM Statistical mechanics

TGN Trans Golgi network

YOPA 3-palmitoleoyl-2-oleoyl-D-glycero-1-phosphatidic acid

YOPC 3-palmitoleoyl-2-oleoyl-D-glycero-1-phosphatidylcholine

YOPE 3-palmitoleoyl-2-oleoyl-D-glycero-1-phosphatidylethanolamine

YOPS 3-palmitoleoyl-2-oleoyl-D-glycero-1-phosphatidylserine

Chapter 1: Introduction

1.1 Biological Interfaces

1.1.1 Biological membranes

Membranes are essential dynamic barriers for biological cells, both from their surroundings and to allow internal compartmentalization [1, 2]. Membranes are mainly made of lipids, amphiphilic molecules that self-arrange into a bilayer. Cell membranes have different lipid composition to allow the interaction of specific proteins and small molecules [3]. The diversity of each membrane ensures cell's health and survival; even a single membrane has different regions with their own the lipid distribution, enabling the formation of lipid rafts or domains that have different functionality. This ensures only certain proteins interact with a section of the membrane so the cell functions properly [4].

There is a wide variety of membrane lipids; single-cell organisms like yeast *Saccharomyces cerevisiae* have hundreds of them in their lipidome, while higher-order eukaryotes have thousands of them [5]. The amphiphilic character of these molecules, hydrophobic tail and a hydrophilic head, is the driving force for them to organize into

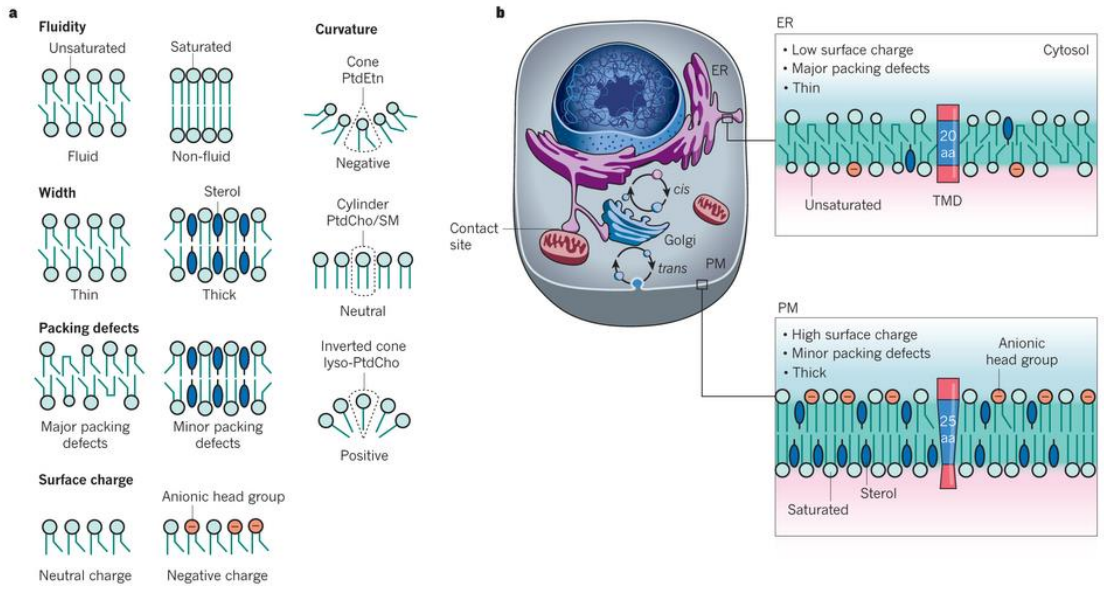

Figure 1 – Lipid diversity in membranes (Fig. 1 in [3])

bilayers. The hydrophobic environment of the bilayer creates a suitable environment for transmembrane proteins. Furthermore, membrane lipids store energy in the form of fatty acids (FAs) and sterols in mammalian cells, but act as membrane protectants in single-cell organisms like yeast [6, 7]. These lipids are made of a combination of FA tails and a headgroup; the length and unsaturation degree of the FAs allow them to adopt different phases when forming the bilayer structure (see **Figure 1**). By convention, FAs in the *sn*-2 position are those attached to the oxygen atom of the second carbon of the glycerol group, while the other tail is the *sn*-1 chain. [8-12]. Lipid headgroups are neutral, charged, or have ring structures and sugars that influence the dynamics of the membrane and its surface potential, affecting its interaction with other molecules [13]. Since lipids are free to move laterally in the membrane, they can form

clusters with other lipids to form distinct phases or domains. The chemical structures and names of the lipids used in this research are shown in **Figure 2** [1, 14].

Experimental techniques are used to study the lipid profile of cells, but these cannot yet examine detailed information on how lipids interact with each other or how they are regulated [15]. The role of lipid composition in cell signaling processes, lipid synthesis and trafficking is not fully understood, nor is the transport of lipids or their assembly into organelle membranes [7, 16]. Computational modeling is a tool to study some of these concepts at the molecular level. Simulation studies can be used to understand lipid-lipid interactions at the atomic level, learn the effect of lipid composition on a bilayer's mechanical and dynamical properties, and lipid lateral organization and clustering [17]. Given the importance of lipid composition for membrane structure and function, it is desirable to have accurate simulation models to understand these properties in terms of lipid-lipid interactions.

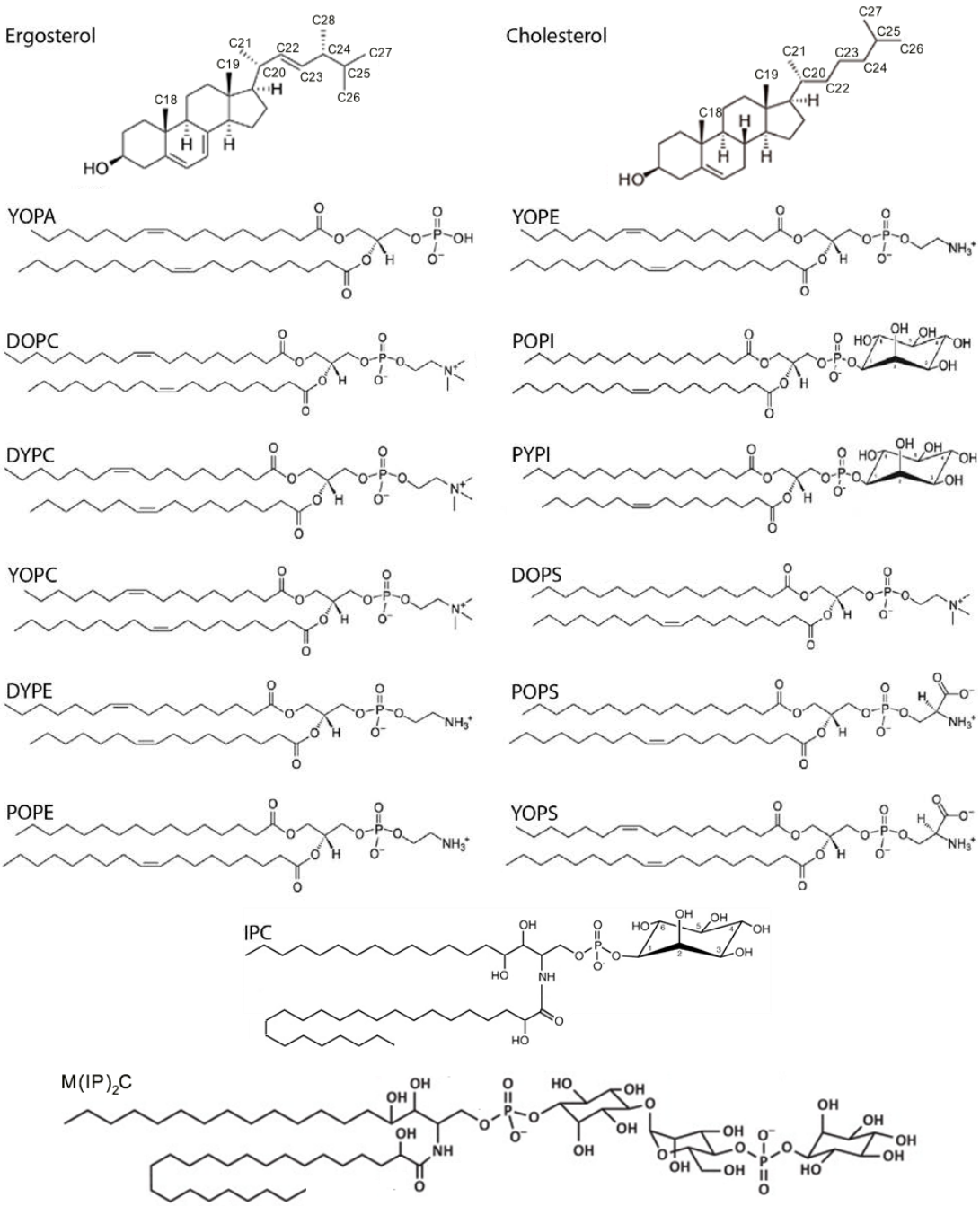

Figure 2 – Chemical structure of the lipid species used in this work

1.1.2 Symmetric membrane models

Simulation studies have used simple symmetric bilayers as models in the past to mimic the hydrophobic environment of a membrane with a mixture of two or three lipids [18-20]. Usually a model with a single lipid type is employed in the study of transmembrane proteins to reduce the complexity of the system. Studies of membrane phase separation into liquid ordered (L_o) and liquid disordered (L_d) domains have received more attention in the past 20 years [21, 22], with both experiments and simulations using only phosphatidylcholine (PC) lipids and cholesterol [23]. While it is remarkable to learn valuable information from such simple models, more recent studies aim to understand the lipid dynamics that drive and stabilize the formation of lipid domains, lipid phase coexistence, and the lateral organization of lipids in a bilayer using more detailed models [24, 25].

My MS thesis work focused on developing more accurate models for the ER, TGN, and PM of yeast, a very common reference organism in modern biology [7, 26]. These models were symmetric bilayers based on experimental compositions for each organelle [27]. Most lipids, and proteins, are synthesized at the ER, the starting point of the secretory pathway that expands from the nucleus to the PM [1, 27]. However, the majority of these lipids are then delivered to their final locations at the PM or TGN. The TGN is a sorting station for lipids that resists many of fluxes coming to and from the ER and PM. The Golgi apparatus is also known as a major producer of

sphingolipids, structural lipids of eukaryotic cells [1, 15, 28, 29]. As part of the secretory pathway, sphingolipids and ceramides are transferred to the PM, the outermost and most rigid membrane of the cell [14, 27]. These membrane models, although limited, allowed me to expand the study of lipid-lipid and protein-lipid interactions in yeast (Chapters 4 and 6).

The symmetric models show lipid diversity and composition affect the structural and mechanical properties of a bilayer. Additionally, symmetric models can be used to study cluster domain formation. Total lipid extracts from yeast membranes were studied with fluorescent probes and showed phase segregation into L_o and L_d domains [21]. C-laurdian spectroscopy studies found that a mixture of inositol phosphoceramide (IPC) and ERG induced more ordered bilayers than those with cholesterol, but adding a third lipid reduced the order for ERG-containing membranes [21]. This third lipid was either phosphatidylinositol (PI) or phosphatidylcholine (PC). This work presents simulations of three-component membranes to study membrane structure in IPC/ERG/POPI and IPC/ERG/POPC systems in Chapter 4.

1.1.3 Asymmetric membrane models

Lipids are distributed unevenly across leaflets in some membranes. Symmetric models were a good enough simplification for the ER membrane, but the PM and TGN show distinct composition in their cytosolic and non-cytosolic leaflets [1]. In order to understand more complex events like the dynamics of lipid domain formation,

asymmetric models are needed to describe the bilayer environment of these organelles. For example, sphingolipids (SMs) are in higher quantities in the non-cytosolic leaflet in the PM and TGN, while PS and PE lipids enrich the cytosolic leaflet [1]. SMs are of special importance in protein-bilayer interaction as well as cell signaling and are the most common phospholipid in the PM [7, 30-33]. These usually have long fully saturated tails that facilitate the formation of sterol-rich domains. Specific mixtures of SMs with saturated chains, unsaturated phospholipid tails, and cholesterol can result in phase separation of L_o and L_d domains [1]. Interest on lipid domain formation has increased in the past twenty years, and has been associated with membrane curvature as well as signaling processes [30, 34]. Experimentally, these domains are known as lipid rafts that are large enough to be studied with fluorescence techniques in model membranes. Nonetheless, these domains may be on the nm scale *in vivo* and may be dynamic and impossible to isolate for detailed study [1, 35-37].

Chapter 5 describes the first all-atom study of asymmetric bilayers with updated PM and TGN model membranes for yeast (see Figure 3). These new models contain IPC and mannose-(inositol-P)$_2$-ceramide (M(IP)$_2$C), the most abundant IPC lipid [38]. IPC lipids constitute 8% and 30% of all lipids in the TGN and PM, respectively [1, 38, 39]. Long chains are suggested to induce leaflet coupling in membrane order and diffusion, although this effect is not completely clear [40]. The most common chains for yeast IPC lipids are 18:0/26:0 [41], and a total chain length of 46, followed by 44,

for M(IP)$_2$C [39]. These SMs are the only ones with two fully saturated chains, and may be needed for coexisting L_o and L_d domains in the presence of high sterol concentrations, which modulate relevant membrane dynamics [1, 42-44]. Asymmetric bilayers were not built in the previous study because the ceramides and sphingolipid parameters were under development at the time [45].

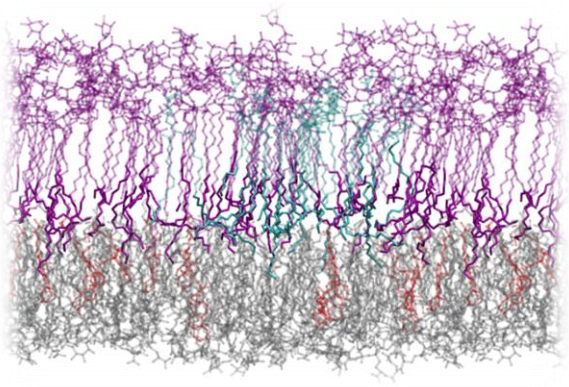

Figure 3 – Asymmetric TGN model
IPC and M(IP)2C lipids on the non-cytosolic leaflet shown in cyan an purple respectively, the other lipids in this leaflet are omitted for clarity; ERG in the cytosolic leaflet is shown in red and the other cytosolic lipids shown in gray

1.1.4 Role of sterol in membranes

Small molecules such as ions and smaller lipids like sterols also contribute to the proper function and mechanical properties of the cell membrane. Sterols influence the fluidity and order of the bilayer, and may affect the cell's response to disease. At high concentrations they modulate lipid domains, and separate the membrane into L_o sterol-rich and L_d sterol-poor phases. This phase separation gives rise to important membrane dynamics and changes in its mechanical properties that determine how the cell responds to its environment [1, 42-44]. Cholesterol (CHL) is an important regulator of cell properties in mammalian cells [14, 42], and its homologue ERG is also crucial for cell

survival in fungal cells like yeast. ERG and CHL differ in the number of double bonds in the sterol tail and center six-membered ring [46].

Sterols are the predominant non-polar lipids in biological membranes; cholesterol (CHL) and its homologue ergosterol (ERG) are the major representatives in mammalian and yeast cells, respectively [14, 42]. The interaction of sterols with other lipids has been extensively studied in the past through experiments using NMR measurements as well as neutron and X-ray scattering techniques, and with molecular dynamics (MD) studies to characterize the interactions in terms of structure and thermodynamics [47]. The effect of sterol molecules on membrane structure and dynamics varies according to the amount in which they are present [48-50]. Now it is known that lipid environment also has an influence on the sterol molecule [51], specifically on the location of the sterol molecule within the hydrophobic core of the bilayer [47, 52].

CHL is known to affect the bilayer thickness, surface area per lipid, lateral fluidity, and mechanical strength [47, 53], properties that also affect the interaction with other molecules in the cell and proteins. In addition, it has been well stablished that CHL increases order and surface density in a bilayer, also known as the condensing effect (reduction in surface area) [49, 53]. Common systems of study to understand CHL's influence on membrane properties use pure lipid or binary mixtures of lipids like 1,2-Dimyristoyl-sn-glycero-3-phosphocholine (DMPC), 1,2-Dipalnitoyl-sn-glycerol-3-

phosphocholine (DPPC), 1-Palmitoyl-2-oleoyl-sn-glycero-3-phosphocholine (POPC) and 1,2-dioleoyl-sn-glycero-3-phosphocholine (DOPC) [47, 49, 53-55]. From the experiments and simulation studies on this molecule, it is known that chemical structure affects its function and relationship with other lipids in a bilayer [56]. Even sterols with minor differences in chemical structures to that of CHL affect membrane mechanical properties and dynamics differently [57, 58].

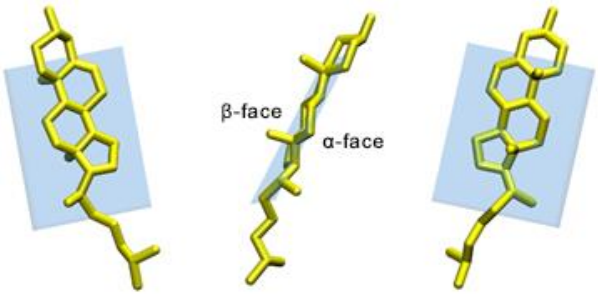

Figure 4 – Faces of CHL distinguished by the presence/absence of methyl groups.
(left) Sterol α-face (smooth), **(center)** side view showing the ring plane, **(right)** sterol β-face (rough) with its two methyl groups pointing out of the ring plane.

The chemical structures of CHL and ERG consists of an asymmetric ring plane with a hydroxyl group in one end (C3) and a branched six-carbon tail in the opposite end (C20-C26), see Figure 2. The asymmetry about the ring plane results in two distinct faces, one smooth and one rough face also known as α and β faces respectively [47, 56, 59]. The β-face has two methyl groups while the α-face has none (see **Figure 4**). Additionally, the extra double bond in the tail of ERG tilts it with respect to the ring plane, which, on average, does not occur in the fully saturated tail of CHL that is almost parallel to its ring plane [60]. The double bond on the ring plane of ERG makes it more rigid and restricts its motion, which in turn modulates membrane properties [61]. ERG has been much less studied than CHL and

the results are not always in agreement, i.e., vary upon the lipid membrane environment [61]. Moreover, limited MD studies have compared the effects of these sterols on membrane properties at the molecular level [55], and current studies are not in agreement with each other [62]. Clear understanding of sterol influence on membrane structure and dynamics is of interest to study biological process, such as cell signaling pathways [54], and to understand sterols' biosynthesis [55].

1.2 Protein-membrane interactions

Proteins are essential for all biological processes; they range from small peptides to complex structures formed by subunits. They performed a variety of roles in the cell, from catalyzing reactions to transporting cargo or serving as mechanical support. The secondary structure of proteins is determined by its sequence of amino acids, their polar, non-polar, hydrophobic, neutral, or charged character drives their arrangement into α-helices, β-sheets, and loops or random coils. The spatial configuration of a protein, relative orientation of its secondary structures, may vary according to its surroundings to activate or deactivate its function [63]. Current research examines protein folding, docking, and protein-membrane interactions.

Protein-membrane interactions have become a popular research area; of particular interest are amphiphilic molecules, given their relevance and how ubiquitous they are nature and biology. They are at the core of studies on drug delivery [64] and cell toxicity due to element insertion into the bilayer [65]. Amphiphilic helical peptides

have received more attention in the past years due to interesting effects they seem to have on cell membranes. Their interaction with biological bilayers has been linked to membrane stress response, cell signaling, and lipid trafficking among others [66]. Examples of helical peptide-membrane studies in the recent years include curvature sensors like ArfGAP1 [67-69], CRAC peptides [70], model alpha-helices to study peptide structure and bound conformation (MP-X study) [71], and hairpin virus peptides to study membrane fusion processes [72]. In addition, current research is looking into the mechanism of peptide binding to identify the key forces and dynamics of peptide-membrane interaction.

Protein distribution in the bilayer is highly influenced by membrane lipids that modulate protein the binding, activation, and signaling in and around the bilayer. Transmembrane proteins localize to specific regions of the bilayer depending on their size and the electrostatics [1]. Protein domains outside the bilayer can also bind to the surface of the bilayer or interact with peripheral proteins; these later ones act as enzymes, lipid transporters, or facilitators of membrane contact sites [73]. Lipid-transport proteins (LTPs) are a specific subcategory of peripheral proteins that provide alternate means to vesicular transport [74].

1.2.1 Lipid transport proteins, Osh4 in yeast

LTPs have received more attention in the past few years and are identified as key players in non-vesicular transport [75]. Non-vesicular transport mechanisms have been

studied for the past thirty years, but substantial progress has been made in the past fifteen years with the emergence of more accurate experimental techniques and the rapid growth of computational biology [76, 77]. Several studies show that lipid transport from the ER to the PM, TGN, and mitochondria is not impaired when vesicular transport is blocked, suggesting non-vesicular pathways are readily available in the cell [78-80]. Lipids like sterols, phosphatidylcholine (PC), phosphatidylethanolamine (PE), phosphatidylinositol (PI), and phosphatidylserine (PS) have been shown to be transported by this method, but the extent and their precise mechanism of transport is still unknown [3].

A comprehensive review by Lev [75] summarizes the role of LTPs in different organelles of the cell as well as proposed mechanisms for their operation. These mechanisms are currently under study, and some LTPs are thought to be recruited to the bilayer surface at membrane contact sites (MCS) to facilitate lipid exchange between two membranes that are within 30nm of each other [3, 81]. LTPs follow a general mechanism of embedding into the cytosolic leaflet of an organelle when they approach it in an open conformation; some may act as lipid sensors instead of transporters, and even bind two membranes simultaneously [79]. However, several LTP families are yet to be fully characterized, and their functions have been expanded beyond lipid transport due to the conservation of protein domains related to cell migration control and carcinogenesis, among others [3].

A family of seven oxysterol binding homologue (Osh) LTPs in yeast has received increased attention in the past fifteen years [82-84]. Osh1-3 are large proteins (800-1600 residues) and contain a PH domain, while Osh4-7 are shorter (<450 residues) and lack the PIP-binding domain [85]. Out of the seven Osh proteins in yeast, only Osh3, Osh4, and Osh6 have crystalized structures [86-88]. In addition, studies showed Osh6 and Osh7 regulate PS through PI4P signaling [89, 90]. However, the precise mechanisms driving protein-membrane interactions are not well characterized. Studies show Osh4 transports sterol in the opposite direction to PI4P using the same binding pocket [87], and sterol binding to Osh4 acts as a regulator of PI4P levels in cells [91]. The current hypothesis of Osh4's function is that sterols are delivered from the ER to the TGN, and PI4P is delivered from TGN to the ER [92, 93]. A recent study by LeBlanc *et al.* has also suggested that Osh4 indirectly contributes to maintain the levels of sphingolipids in the cell [94].

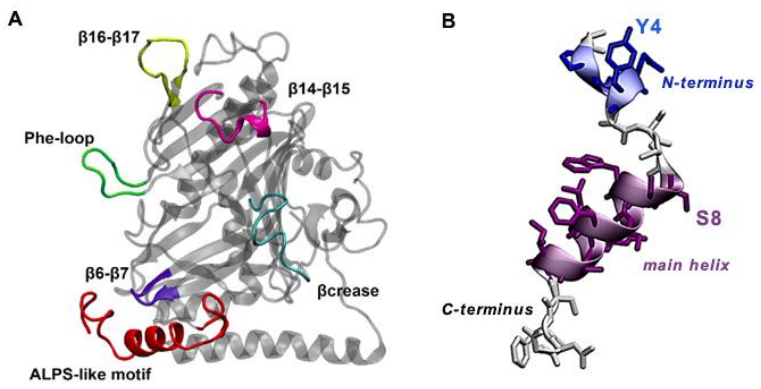

Figure 5 – Snapshots of Osh4 and its ALPS-like motif
(A) Osh4 protein and its six binding regions (Fig. 2 in [73]) (B) ALPS-like motif of Osh4 and relevant residues identified in the binding studies presented in this work.

Crucial to understanding lipid transport via Osh4, shown in **Figure 5**.a, is understanding how it binds to membranes for lipid uptake/release. Potential membrane binding sites on Osh4 were found using cross-linking and fluorescence studies, which along with Osh4's ability to bind two liposomes containing PS lipids simultaneously led Schulz *et al*. to conclude sterol transport might occur at MCS where Osh4 facilitates lipid transport by a pivot-like mechanism [95]. Computational studies showed Osh4 binding to lipids [96] and model membranes [97] with 0-10% anionic lipids, and were in general agreement with the experiments published by Schulz *et al.* These studies identified six membrane binding regions in Osh4 (shown in **Figure 5**.a), and established protein binding occurs through nonspecific interactions with anionic lipids. Moser von Filseck *et al.* further showed the relevance of Osh4 lid, the amphipathic lipid packing sensor (ALPS)-like motif, in the transport of sterols, and the difference in protein behavior when the ligand is a sterol vs. a PI lipid [98]. Despite the advances, the protein's binding mechanism to a membrane in a conformation that accounts for lipid uptake/release has not yet been attained.

1.2.2 The ALPS-like motif of Osh4

Membrane curvature sensing occurs mainly by hydrophobic and/or electrostatic interactions, and sometimes is dictated by protein geometry or membrane surface packing defects [99]. Eukaryotes' cell membranes need to constantly reorganize their components to function properly; membrane curvature sensors contribute to this fact

facilitating reactions such as lipid transfer or membrane contact sites [66, 99]. Amphipathic helices that act as membrane curvature sensing domains in larger proteins are 20 to 40 amino acids in length, and have a distinct hydrophobic face and charged residues that also contribute to peptide-membrane interaction [69, 99, 100]. In addition, it has also been suggested that ALPS and ALPS-like peptides bind to specific targets [100]. In the case of ALPS motifs, their interaction with a membrane surface seems to be rather driven by lipid packing defects on the surface of the interacting leaflet [69].

The ALPS-like motif of Osh4 (see **Figure 5**.b) is a 29 amino acid peptide which also forms the lid to protect sterols. It has also been identified as a membrane curvature and/or lipid packing sensor, and has one of the lowest hydrophobic densities with respect to its hydrophobic residues [69, 100]. Experiments show that Osh4 does not bind to small vesicles when this motif is not present [99]. However, it is not clear whether this peptide binds to membranes due to their packing defects, or if it instead creates packing defects upon binding and thus facilitates lipid extraction for Osh4.

1.3 Non-biological interfaces

Phase behavior at water-oil and water-air interfaces has received increased attention in the past sixty years [101]. A tension force develops when these two liquids come in contact because they are immiscible, this tension at the interface is known as interfacial tension [102]. Surfactant molecules reduce the tension at the interface, but so do small alcohols can act as surface tension reducing agents of the hydrophobic and hydrophilic

interface [103]. Such molecules are known as hydrotropes, amphiphilic molecules, with both a hydrophobic and a hydrophilic moieties, that reduce the interfacial tension and increase the solubility of weakly soluble compounds in water [104, 105]. The study of these molecules is relevant in the chemical, pharmacological, and biological fields because of their amphiphilic character [106]. In addition, understanding the behavior of hydrotropes in aqueous solutions will contribute to the overall understanding of the role of water in both chemical and biological systems, and mesoscale phenomena [103, 107].

Tert-butyl alcohol (TBA) is a widely studied hydrotrope, but its behavior is not yet completely understood at low molar compositions in aqueous solution or at the limit of liquid-liquid equilibrium (critical phenomena) [103]. TBA cannot self-assemble into micelles, but molecular dynamics studies have shown they do form short-lived clusters in aqueous solution [103] [106]. Chapter 7 discusses the study of the water-cyclohexane interface and its disruption by varying amount of TBA. Furthermore, all four isomers of butanol (**Figure 6**) were examined to understand the effect of chemical structure on interfacial tension disruption.

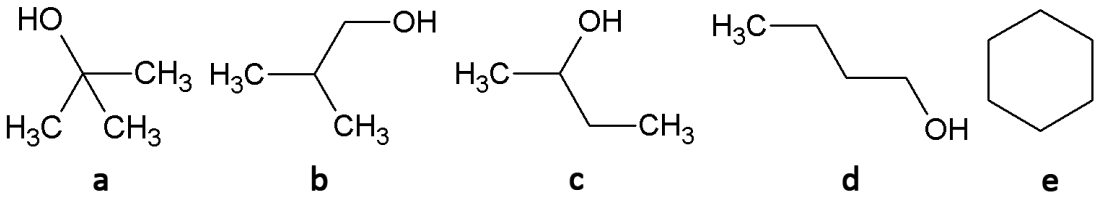

Figure 6 – Chemical structure of butanol isomers
(a) TBA, (b) isobutanol (IBUT), (c) secbutanol (SBUT), (d) n-butanol (NBUT), and (e) cyclohexane (CHX, the organic phase)

1.4 Molecular Dynamics

Molecular dynamics (MD) simulations can be used to understand the interactions and forces of a given system at the molecular level and their influence on macroscopic properties. MD simulations facilitates the study of processes that take place over very short time scales, predict trends or mechanisms, and can be helpful in the selection of experimental targets. This simulation technique is deterministic, based on statistical mechanics and empirical energy functions known as force fields (FFs). It works by modeling the interactions within a system based on forces acting on its atoms. Given a set of initial coordinates for a system, random initial velocities are assigned for atom using equation 1, the Maxwell-Boltzmann distribution for a given temperature, where v_α is the α component of the velocity at time *t* [108]. Newton's laws of motion are solved for each atom based on its velocity (*v*) and forces acting over it, generating simulation trajectories that specify each atom's position (*r*) with respect to time. Equations 2 and 3 result by integrating Newton's equations results for the position and velocity of each atom in the system respectively. The chemical structure of a molecule or crystallographic structures for proteins can be used to set the coordinates of a system [109].

$$\langle v_\alpha^2 \rangle = \left(\sum_{i=1}^{N} {mv_{\alpha,i}^2(t)}/{N_t} \right)/m \quad \textbf{(1)}$$

$$r(t+\Delta t) = 2r(t) - r(t-\Delta t) + \left({f(t)}/{m} \right) \Delta t^2 \quad \textbf{(2)}$$

$$v(t) = {\{r(t + \Delta t) - r(t - \Delta t)\}}/{2\Delta t} + O(\Delta t^2) \quad \textbf{(3)}$$

The first stage of a MD simulation is to equilibrate the properties of the system, like total energy and temperature such that they stochastically fluctuate over a constant value over time. Structural and dynamic analysis is done over the equilibrated portion of the simulation trajectory. Different properties can be calculated in terms of the position and momenta of each atom in the system over this section of the trajectory. Multiple simulation trajectories (replicates) for a system are highly desirable to obtain statistically relevant results [108].

Atomistic models used in MD techniques have evolved in the past 60 years. Complex models use a continuous potential to describe the forces acting on an atom every time it changes position. In this case, the integration of the laws of motion is made by finite difference method. To avoid large errors due to fast motions in a molecule, the integration time step is commonly set to 1-2fs for biological systems depending on the molecule of study [108].

1.4.1 Force Fields (FFs)

FFs are empirical energy functions MD uses to describe inter- and intramolecular forces in a given system. These are evaluated through a potential energy function, $V(\hat{R})$, where $\hat{R}$ stands for the position of atoms in the system see (equation 4). Different terms in a FF account for bonded and non-bonded interactions, attractive and repulsive forces,

angles bending, and torsional and rotational energies. The FF is as complex as the molecules of study, i.e. simpler molecules do not require as many terms in the FF as complex ones [108]. Intramolecular forces are evaluated looking at the bond and angle energy terms in the energy function. Non-bonded interactions specify the relationship of every atom in the system with its far-neighboring atoms. Attractive and repulsive forces are accounted for by the van der Waals (VDW) potential, evaluated using a 6-12 Lenard-Jones potential with cut-off values set by the user; typical cutoffs in biological systems range between 8 and 16 Å [109].

$$V(\hat{R}) = \sum_{bonds} K_b (b - b_0)^2 + \sum_{angles} K_\theta (\theta - \theta_0)^2 + \sum_{cross\,\mathrm{UB}} K_{UB} \left(r_{1,3} - r_{1,3}^0\right)^2 + \sum_{improper} K_{im} (1 - \cos(2\phi)) + \sum_{dihedrals} \left[\sum_j K_{\varphi,j} \left(1 + \cos(n_j \varphi - \delta_j)\right) \right] + \sum_{\substack{nonbonded \\ pairs i,j}} \varepsilon_{ij} \left[\left(\frac{R_{\min,ij}}{r_{ij}} \right)^{12} - \left(\frac{R_{\min,ij}}{r_{ij}} \right)^{6} \right] + \sum_{\substack{nonbonded \\ pairs i,j}} \frac{q_i q_j}{\varepsilon_D r_{ij}} \quad (4)$$

The set of parameters used in a FF to determine the energy contributions of the different terms in the empirical function is unique and of critical importance to the accuracy of the FF. These parameters are set to reproduce experimental properties of different chemical structures. The choice of FF is left to the user according to the study target [108], currently some commonly used FFs in biological studies are CHARMM [110], AMBER [111, 112], GROMOS [113], MARTINI [114], and OPLS[115].

1.4.2 Thermodynamic ensembles

MD simulations use statistical thermodynamics to predict the macroscopic properties of a system from the molecular structure and interactions of a given system. The macroscopic properties are computed from the longtime average of the corresponding microscopic property. The average value of a given property is evaluated considering all possible states of the molecules taking into account the constraints imposed on the overall system. These constraints can be a fixed temperature (T), pressure (P), volume (V), number of molecules (N), or energy (E). In statistical thermodynamics, the group of possible constraints is called an ensemble. Some common ensembles used in simulations are the canonical ensemble (constant N, V, T), isobaric-isothermal ensemble (constant N,P,T), and the microcanonical ensemble (constant N, V, E). One will be preferred over the rest depending on the macroscopic properties that want to be evaluated; all of the ensembles should result in the same value of that properties, but the computation process will differ [116, 117]. The NPT ensemble is one of the most common in MD, and all thermodynamic properties are derived from the Gibbs energy (*G*) of the system [108, 116].

1.4.3 Temperature and pressure control

The temperature of a system is related to its average kinetic energy over time. CHARMM software package [118], used to analyze the trajectories of all the present studies, uses a method developed by Nosé in 1984 that was further improved by

Hoover, known as the Nosé-Hoover thermostat. A thermal bath and extended Lagrangian methods with artificial coordinates and velocities for the system are used to keep its temperature constant. To achieve this, the position of each atom times a parameter that determines the coupling between the real and extended systems is computed at the desired interval. NAMD, another software package used for this dissertation [119], uses Langevin dynamics to maintain the temperature constant throughout simulation [108, 109].

For constant pressure control, the volume is the dynamic variable and the appropriate equation is added to the set of equations to be integrated for the simulation. CHARMM controls the pressure isotropically using the Nosé-Hoover piston. In NAMD, the pressure is controlled using the Langevin piston Nosé-Hoover method coupling the piston controls to a temperature bath controlled by Langevin dynamics [119-121].

Long simulation trajectories were run on the Anton [122] and Anton2 [123] machines. These run using the Anton-software, based on the simulation package Desmond [124]. Pressure control is achieved using the Martyna-Tobias-Klein method that combines a constant pressure an enthalpy piston and a constant volume a temperature Nosé-Hoover thermostat, while temperature is kept constant with Langevin dynamics. These two controls are most commonly setup using the multigrator integrator [125].

Chapter 2: Computational Methods

2.1 General simulation settings

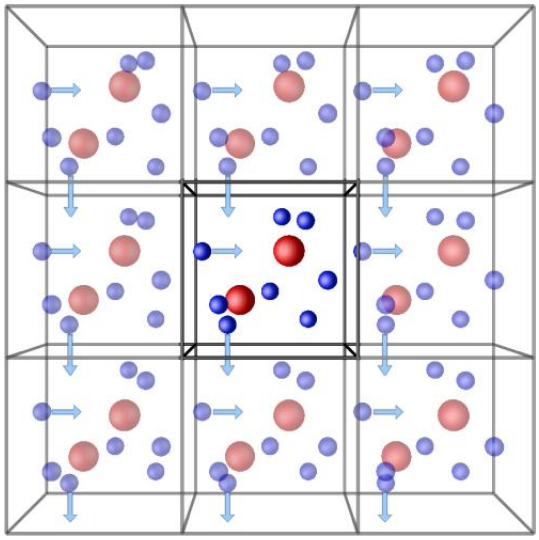

Figure 7 - Periodic boundary conditions illustration (http://isaacs.sourceforge.net/phys/pbc.html)

Most of the systems in this work were simulated and/or analyzed using CHARMM [110] and NAMD [119] software packages. Long trajectories (microsecond length) were obtained running on the Anton [122] and Anton2 [123] machines at the Pittsburgh Supercomputing Center. Some of the data analysis of these long trajectories was done using the Anton software or Desmond software package [124]. The Anton machines run simulations using their own software (*anton_software/versionx.x)*, which is based on Desmond software. Specific analysis, like the interaction energies, was done using Desmond package. The present simulations used the CHARMM36 (C36) FF that takes on the general form in equation 4; the membrane simulations used the most updated parameters for PI and SM lipids

[45, 126, 127]. All systems were neutral to meet the requirements of NAMD for long-range electrostatic calculations using the Particle Mesh Ewald (PME) summation method [128]. Simulations were run using periodic boundary conditions (PBC), which use the central box of a simulation and 26 images of it on all faces to prevent erroneous calculation due to the interaction of atoms with the walls of the system [128]. PBC allow an atom moving out of the central box to appear on the opposite side as it comes out of the neighboring image (see **Figure 7**). Simulation settings for specific systems are detailed below.

2.2 Membrane systems

2.2.1 Building membrane models

The membrane systems for this work were constructed using the *Membrane Builder* of CHARMM-GUI (www.charmm-gui.org), an automated graphical user interface to build heterogeneous bilayer and bilayer-protein systems [46, 129, 130]. It has a wide biologically relevant lipid library with over 200 lipids classified by headgroup structures and sterols [131]. The user inputs the number of lipids per leaflet, or their relative ratio, and the level of hydration for the system (number of water molecules per lipid) or water thickness above and below the bilayer. The system is built based on estimates for the area per lipid for each component, which can be modified by the user if desired. The area per lipid estimate is very important to avoid clashes or ring penetration issues in the model. Lipid orientations in the bilayer are randomly chosen

from a set of 1000 orientations for each molecule to prevent biased results. For this study, replicate systems were built separately to start simulation trajectories from different configurations. Subsequent building steps include setting a preferred temperature, thermodynamic ensemble, and the addition of ions to render a neutral system, or as specified by the user.

Each system undergoes a short equilibration and check for ring penetration or bond breakage occurrences on CHARMM-GUI before the coordinates and structure files (PDB and PSF respectively), along with the topology, parameter, restraint, and equilibration input files are output for the user. The *Membrane Builder* provides CHARMM and NAMD input scripts ready to be used or modified at the user's discretion. Typical membrane equilibration is achieved in a series of 6 consecutive steps, the first two steps run using the NVT ensemble. The remaining four steps use the NPT ensemble with decreasing restraint force constants to prevent FA double bonds from changing its *cis*/*trans* conformation, keep PI lipids in the chair conformation, maintain C2 chirality in each lipid, and hold the lipid head groups in position along the z-axis [131]. CHARMM-GUI uses the C36 FF because it allows heterogeneous MD simulation runs in the isobaric-isothermal (NPT) ensemble with no surface tension, and accurately reproduces experimental properties of lipid bilayers such as deuterium order parameters (S_{CD}) and lipid rotation rates from NMR measurements [46, 132]. The user can use a different FF if desired for the equilibration and production runs.

The topology files for IPC and $M(IP)_2C$ lipids (shown in **Figure 2**) were not originally included in the topology files of C36 FF. The coordinates for these molecules were built from a ceramide template (CER240) obtained from the Glycolipid Modeler [129], a new tool under development in CHARMM-GUI. The ceramide template was modified using PyMol [133] and Chimera [134] to obtain PDB and PSF files for the two SM lipids, and the topology file for CER240 was modified manually to match the resulting PSF for IPC and $M(IP)_2C$. A minimized structure for each molecule was obtained by running a short vacuum simulation of a single lipid molecule in CHARMM. The short trajectory was then used to save a library of lipid coordinates with slightly different configurations to be used in the membrane models. Bilayers including these lipids were built in CHARMM-GUI using CER240 as place holder for the SM lipids; its area per lipid was increased 30% to ensure enough space for the bulkier SM lipids. The CER240 containing bilayers were equilibrated from 50ns and then the lipid switch for IPC or $M(IP)_2C$ according to the lipid concentrations desired in the models.

2.2.2 Symmetric ER/TGN with CHL

Table 1 - Model lipid types by headgroup and unsaturation content of the sn2-sn1 tails. **Figure 2** shows the corresponding chemical structures.

Lipid		**Unsaturation** ***(sn2-sn1)***	**ER**	**TGN**
sterol	CHL		7	18
PA	YOPA	18:1-16:1	6	4
PC	DYPC	16:1-16:1	42	40
	YOPC	18:1-16:1	28	12
PE	DYPE	16:1-16:1	10	8
	YOPE	18:1-16:1	10	8
PI	POPI	18:1-16:0	21	13
	PYPI	16:1-16:0	14	42
PS	POPS	18:1-16:0	12	-
	YOPS	18:1-16:1	-	5
lipids per leaflet			*150*	*150*
% unsaturation			*68.9*	*79.2*
mol% sterol			*4.67*	*12.00*
water molecules			*9127*	*17261*
potassium ions			*106*	*128*
total # of atoms			*65.1K*	*88.2K*

Simulations from the previous ER and TGN symmetric models [27] were extended to examine the effect of sterol type on the structure and dynamics of bilayer models. These models have lipid composition characteristic to each organelle based on experiments [135, 136] using phosphatidic acid (PA), phosphatidylcholine (PC), phosphatidylethanolamine (PE), phosphatidylserine (PS), and phosphatidylinositol (PI) lipids. **Table 1** summarizes the lipid types and quantities used in each model along with the amount of water and neutralizing ions for each system. None of the lipids in these models are fully saturated but have at least one monounsaturated tail, and the chains length varies between 16 or 18 carbons.

These models used CHL instead of the ERG molecules of the original ER and TGN models for yeast. The systems were built replacing the ERG molecules on the final coordinates of each equilibrated trajectory (previous study) by CHL, and the TIP3P model was use for water [137]. Two replicate trajectories were run for the new models for 100ns each on NAMD. The simulation setup was kept identical to that of the ERG models [27]: NPT ensemble with a 2 fs time-step, using the Nosé-Hoover thermostat [138] and Langevin dynamics [108, 109] to keep the temperature constant at 303.15K and a Langevin piston [120] to control the pressure and keep it at 1bar. The SHAKE algorithm was used to constraint hydrogen atoms [139], a Lennard-Jones force-switching function [140] with a 8-12 Å cut-off was used to evaluate van der Waals and electrostatic interactions. 150 lipids per leaflet were used to ensure the lateral dimensions were big enough to avoid image atoms of a given lipid interacted with itself.

2.2.3 Symmetric IPC models

Ternary systems containing IPC/ERG and either POPI or POPC were used to study the influence of this third lipid in the interactions and lateral organization of IPC and ERG. The models were first equilibrated for 50ns prior to running two replicates for each model on the Anton machine, each 5μs long. The systems were equimolar, with 48 lipids for each species in both the top and bottom leaflet. The NPT ensemble was also used to study these models at 1bar of pressure and a temperature of 296.15K to replicate experimental conditions of yeast extracts that examined IPC/ERG domains

[141]. Temperature and pressure controls for NPT dynamics on Anton were set by the *multigrator*, the latest integrator for MD simulations on this machine [125]. Lennard-Jones interactions cut-off was set to 10 Å for all systems using Anton software (*ark* files) to meet its requirements. Long-range electrostatics were computed using the Gaussian split Ewald algorithm [142] with cutoffs of 7.743 Å and 8.094 Å for the POPI and POPC systems respectively. Simulation trajectories were saved every 200.04ps to minimize trajectory file size for these long simulations.

2.2.4 Asymmetric yeast membrane models

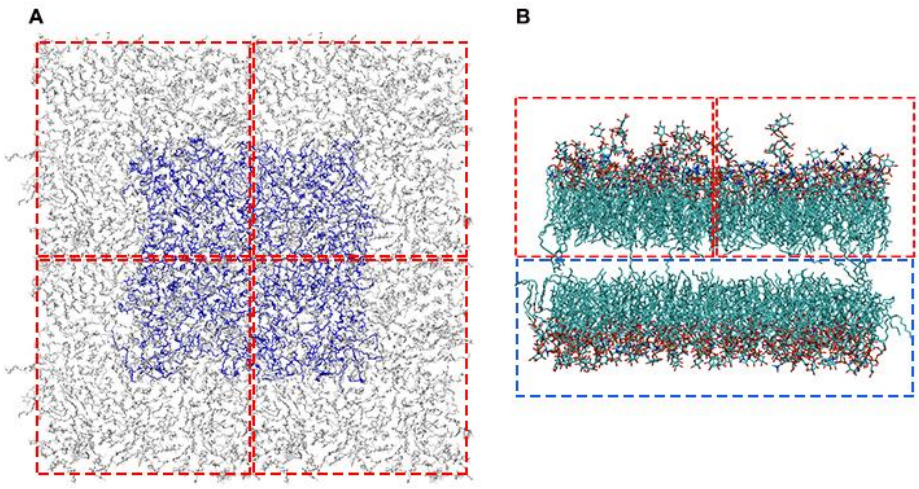

Figure 8 – Building blocks for the asymmetric membrane models
(A) Top view of the cytosolic (blue) and non-cytosolic (gray) leaflet blocks; (B) side view with trimmed top (non-cytosolic) layer

Models for the PM and TGN of yeast were improved incorporating SM lipids and asymmetry. Symmetric models or the non-cytosolic and cytosolic leaflets were first built and equilibrated for 100ns and 80ns respectively; the non-cytosolic leaflet was equilibrated longer due to the presence of saturated SM lipids. The coordinates of the

Table 2 – Asymmetric models composition per leaflet and overall in mol%

	PM			TGN		
Lipid	Cyto %	Noncyto %	Overall % (total)	Cyto %	Noncyto %	Overall % (total)
ERG	21.64	46.21	34.41	3.33	24.4	14.47
DYPC	5.97	4.83	5.38	6.67	31.55	19.81
DYPE	-	-	-	10	-	4.72
POPE	13.43	7.59	10.39	-	-	-
POPI	13.43	-	6.45	27.33	-	12.89
POPS	14.93	-	7.17	-	-	-
PYPI	9.7	-	4.66	30.67	-	14.47
YOPA	-	-	-	-	5.36	2.83
YOPC	5.97	4.83	5.38	5.33	22.62	14.47
YOPE	10.45	-	5.02	10	-	4.72
YOPS	4.48	-	2.15	6.67	-	3.14
IPC	-	9.66	5.02	-	6.55	3.46
$M(IP)_2C$	-	26.9	13.98	-	9.52	5.03
# lipids	134	145	279	150	168	318
# ions			149			149
# waters			14121			14422
# atoms			76682			83466

top leaflet from the non-cytosolic model were saved to be merged with the opposite leaflet from the cytosolic models. The later one had a larger surface area per lipid and was used as a base to merge the other leaflet. The non-cytosolic leaflet coordinates were replicated 4 times and the four blocks positioned on top of the cytosolic leaflet like Lego-blocks (see **Figure 8**). Lipids from the non-cytosolic blocks exceeding the dimensions of the bottom leaflet (cytosolic model coordinates) were deleted. The non-cytosolic lipid blocks were positioned 8 Å away from the other leaflet to prevent lipid

tails clashes. The asymmetric systems were equilibrated for 80ns before running 7μs trajectories on the Anton and Anton2 machines. **Table 2** lists the lipids and composition of each leaflet.

2.3 Membrane-protein systems

2.3.1 ALPS-motif studies

The binding mechanism of the ALPS-like motif of Osh4 was studied with a simple two lipid-component model and with the symmetric ER and TGN models previously developed [27]. The simpler systems consisted of a mixture of DOPC and DOPS lipids in a 3:2 ratio (60:40 mol%) in bilayers of 80 lipids per leaflet, the complex models had the lipid composition listed in Table 1. The coordinates for the peptide were extracted from the full protein, PDBID: *1zhz* [143]. The peptide was inserted in the aqueous phase using CHARMM [110] software package at least 8 Å away from the bilayer, and overlapping water molecules were deleted. Two initial peptide orientations were used to avoid biased binding events, either perpendicular or parallel to the bilayer normal (see **Figure 9**). A block of water was added using Packmol [144] for the parallel orientation to allow enough room for the peptide to freely rotate without forcing peptide-membrane interactions. After a 100-ns equilibration in NAMD, 2-μs trajectories were run on Anton in triplicates for each system for a total of 42μs of simulation (21 systems in total). Given that a previous study showed ALPS peptides bind to membranes with surface-packing defects [69], systems with and without surface

tension were examined. The NPT ensemble was used to run simulations without surface tension, and the NPγT ensemble (where γ stands for surface tension) was used with 20 dyn/cm of tension to increase the lipid packing defects on the binding surface and examine the effects on binding time scale.

The NAMD runs kept the temperature constant at 303.15K to ensure a fluid phase membrane using the Nosé-Hoover thermostat [138] and Langevin dynamics [108, 109] with an integration time-step of 2fs. The cell box size varied semi-isotropically (X=Y but not Z) with constant pressure of 1bar using a Langevin piston [119-121]. Upon initial thermal equilibration the systems were converted into DESRES formant to run on the Anton machine. C36 parameters for ERG and PI lipids were added as custom parameters to the viparr library in Anton as these were not yet included in this format.

Temperature and pressure controls for NPT dynamics were set using Anton's multigrator, and the cut-off values for neighboring atoms was selected using Anton's *ark* files (scripts to optimize the parameters for the integration

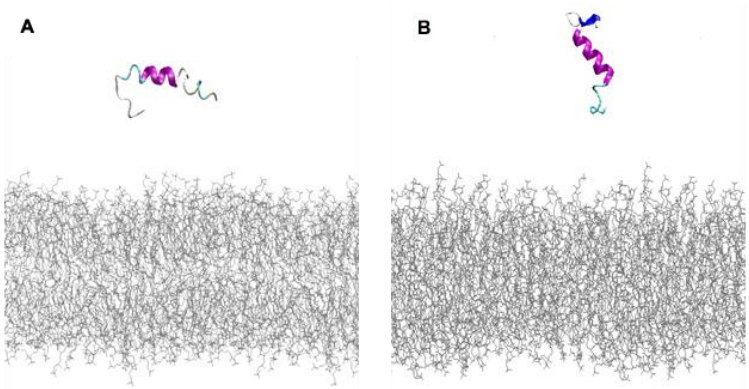

Figure 9 – Initial setup for the peptide-membrane systems
(A) horizontal and (B) vertical orientation of the ALPS-like motif

algorithms of the simulation). Long-range electrostatics were computed using the Gaussian split Ewald algorithm on Anton [142] with cutoffs also set by Anton guesser

Table 3 – ALPS-like motif simulation systems sizes, initial and final configuration

system	Initial peptide orientation away from the membrane	lipids per leaflet	# atoms	γ (dyn/cm)	Final orientation of peptide upon binding	First contact with the bilayer (ns)
o-npt	horizontal	DOPS:48 DOPC:32	54992	0	tilted	1141.14
2					none	none
3					horizontal	180.18
o-nvt				20	vertical (tilt)	1121.12
2					tilted	1747.75
3					horizontal	714.71
z-npt	vertical		54916	0	vertical (not stable)	1301.30
2					none	none
3					vertical	160.16
z-nvt				20	horizontal	932.93
2					horizontal	260.26
3					horizontal	130.13
er	horizontal	ER/TGN models for yeast see **Table 1**	85835	0	vertical (tilt)	580.58
2					vertical (tilt)	400.40
3					horizontal	316.32
20er				20	tilted	340.34
2					horizontal	706.36
tgn			110331	0	vert-hor-vert	360.36
2					horizontal	320.32
20tgn				20	horizontal	300.30
2					horizontal	385.38

scripts. Replicate runs used the same cut-off values as the first run for consistency. Anton software does not support surface tension ensemble, therefore the systems equilibrated with NPγT dynamics on NAMD were extended using the NVT ensemble on Anton. **Table 3** lists the 21 systems of study and their bound conformation.

2.3.2 Full protein studies

The full Osh4 protein was simulated with the symmetric ER and TGN models starting from equilibrated systems with and without surface tension (NPT and NPγT dynamics respectively). Protein coordinates where obtained from crystal structure *1zhz* on the protein data bank (PDB) [143, 145]. The protein was placed vertically at least 10Å above the bilayer, with its mouth region facing the membrane in similar fashion as the peptide described in the previous section. A block of water was added using Packmol [144] to allow enough space for the protein to move in the aqueous phase. The intention of placing its mouth towards the bilayer was to probe lipid uptake, but none was observed. As with all the systems of study in this work, neutralizing ions were incorporated to the system after insertion of the protein. The protein-membrane system was equilibrated on NAMD for 50ns using the NPT ensemble using the same settings as for the peptide-membrane studies described in the previous section. 2-μs trajectories were run on Anton like the peptide-membrane runs with two replicates per system, but the data saving frequency was changed to 100.02ps to examine interaction energies more frequently.

2.4 Water-oil systems

Ternary mixtures of water, cyclohexane (CHX), and butanol were studied to understand the effect of this hydrotrope (butanol) at the water-oil interface. All four butanol isomers where examined for this study to understand the influence of chemical

structure on interfacial dynamics. Topology files for NBUT and IBUT were made using coordinates for these molecules from ChemSketch [146], PyMOL [133], and Visual Molecular Dynamics (VMD) [147] because these were not available in the topology files of CHARMM general FF [148]. The TIP4P-EW water model [149] was used for all these systems to be consistent with previous computational studies [107, 150] and given its superior accuracy compared to TIP3P for these type of studies. NPAT dynamics (where A stands for constant area) were carried at 298.15K and 1bar on NAMD. The area (x and y dimensions) of the basic simulation cell was fixed, but the system was allowed to vary in the z-axis direction (direction perpendicular to the water-oil interface). VDW and electrostatics interactions were computed using a Lennard-Jones force-switching function over 8 to 10 Å [140].

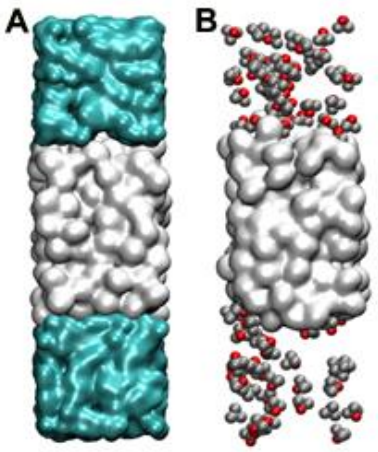

Figure 10 – Simulation setup for the water-cyclohexane-hydrotrope
(A) Bulk water is shown in cyan and bulk cyclohexane in white for the main simulation box. (B) TBA at the beginning of the simulation is shown explicitly with C atoms in gray and O atoms in red, water is omitted for clarity.

Initial system setups were build using Packmol software [144, 151] with a box of water-alcohol mixture on top and bottom of a box containing cyclohexane (see Figure 10) to mimic bulk phases when running with PBC. Five systems were built for each isomer ranging from 0.7 to 20 mol% of alcohol in the aqueous phase (equilibrium

values). A system of pure water and cyclohexane was also simulated to use as reference. TBA studies were extended to test even lower concentrations of hydrotrope, as low as 0.01 mol% in the aqueous phase and compare with experimental values to test the accuracy of our models. **Table 4** lists the system size for these simulations; the systems with a star indicate the systems that were run for all four butanol isomers, the rest were only simulated for TBA. All systems were run in triplicates for 75ns.

Table 4 – System size for hydrotrope studies
(*indicates systems run for all butanol isomers)

system	TBA in water (at equilibrium)		# molecules in simulation			overall mass % compositions			total atoms
	mol%	mass%	water	chx	tba	water	chx	tba	
wat-chx	0.00	0.00	1600	250	0	57.81	42.19	0.00	10900
T1	0.01	0.05	1650	220	8	60.87	37.92	1.21	10680
T2	0.11	0.46	1650	220	26	59.25	36.91	3.84	10950
T3	0.18	0.73	1650	220	34	58.56	36.48	4.96	11070
T4	0.44	1.80	1650	220	44	57.72	35.95	6.33	11220
T5*	0.67	2.68	1600	220	50	56.47	36.27	7.26	11110
T6	1.89	7.34	1500	220	64	53.74	36.82	9.43	10920
T7*	2.64	10.04	1500	220	80	52.50	35.97	11.52	11160
T8	3.48	12.92	1500	220	96	51.32	35.16	13.51	11400
T9	4.47	16.14	1500	220	114	50.05	34.30	15.65	11670
T10	5.54	19.44	1500	220	132	48.85	33.47	17.69	11940
T11*	7.23	24.29	1400	220	156	45.61	33.48	20.91	11900
T12*	12.09	36.13	1300	220	230	39.71	31.39	28.90	12610
T13*	18.59	48.44	1260	220	316	35.12	28.65	36.24	13740
T14	24.05	56.59	1200	220	410	30.65	26.25	43.09	14910
T15	29.79	63.59	1100	220	484	26.71	24.95	48.34	15620
T16	34.24	68.20	1000	220	550	23.31	23.95	52.74	16210
T17	38.91	72.40	1000	220	650	21.27	21.86	56.88	17710
T18	44.61	76.83	900	220	750	17.95	20.50	61.55	18810

Chapter 3: Analysis Methods

3.1 Membrane systems

The following sections describe typical analysis done for membrane simulations, these calculations were performed for all membrane systems in this work unless stated otherwise.

3.1.1 Lateral Membrane Properties

The overall surface area per lipid (SA) was computed for each simulation to determine thermal equilibrium; this is a common metric to establish the stability of lipid-lipid interactions and lipid packing. The trajectory SA was measured on the x-y plane of the simulation box and divided by the number of lipids per leaflet. Component lipid areas (CA) were calculated for all the symmetric membrane models using Qhull [152], a software package that uses a triangulation technique to estimate the volume and surface area of a molecule based on the coordinates of three atoms in the phospholipid tails or one atom in sterol lipids (C2, C21, and C31 in the lipid, and O3 in the sterol). Additionally, the compressibility modulus (K_A) was calculated using equation 5 to measure the resistance of each membrane to uniform compression; where k_B is the Boltzmann constant, A_L is the SA, and σ_A^2 its variance

$$K_A = k_B T * {A_L}/{\sigma_{A_L}^2} \quad \textbf{(5)}$$

3.1.2 Electron density profiles

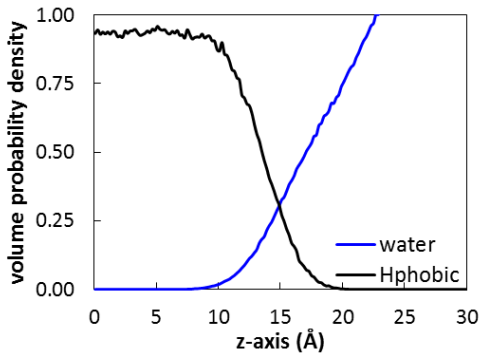

Figure 11 – Sample curves to estimate membrane thickness from EDPs data.

Neutron and X-ray scattering experiments such as small angle neutron scattering (SANS) and small angle X-ray scattering (SAXS) [153, 154] are used to study bilayer structures. These scattering profiles compute the electron density of lipids in a bilayer, which are readily available from MD simulations. Simulation EDPs were plot using SIMtoEXP software package following the procedure of Kučerka *et al* [155]. The head-to-head distance of the bilayer (D_{HH}), the Luzzati thickness (overall bilayer thickness) (D_B), and its hydrocarbon region or core ($2D_C$) were calculated for each system. The half point of the overall volume probability distributions of water and fatty acid (FA) tails (CH_2 and CH_3 groups, hydrophobic region) was used to determine D_B and $2D_C$, respectively. **Figure 11** shows an example of these curves for the ER-CHL system. Estimates from the Orientation for Proteins in Membranes (OPM) database [156] were used to compare the hydrophobic thickness from simulation ($2D_C$) with the hydrophobic length of transmembrane proteins in the ER and PM of *S. cerevisiae* for the ERG containing models, and the ER of *H. sapiens* for the CHL models.

3.1.3 Deuterium order parameters (S_{CD})

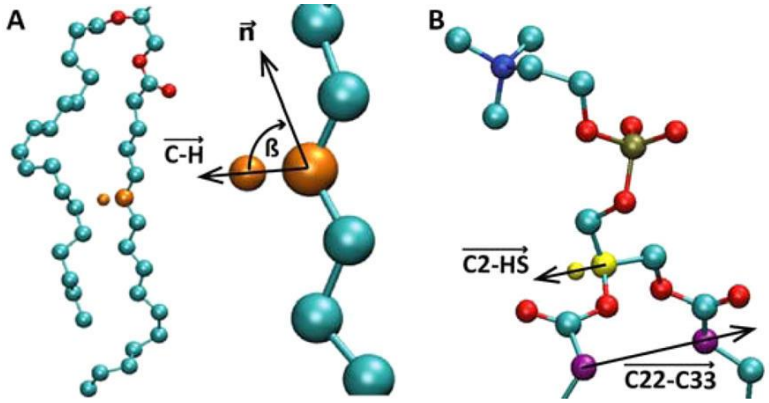

Figure 12 – Diagram of (A) S_{CD} and (B) lipid wobble calculations (Figure 2 in [27])

NMR experiments are commonly used to study the structure and order of lipids in pure or mixed bilayers [157]. S_{CD}s are segmental parameters used to measure the order inside a bilayer; equation (6) is used to compute the S_{CD}s of simulation data,

$$S_{CD} = \left|\left\langle \frac{3}{2}\cos^2\beta - \frac{1}{2}\right\rangle\right| \qquad \textbf{(6)}$$

where β is the angle between each C-H bond (defined by a vector) in the lipid tail and the bilayer normal (see **Figure 12**). As mentioned in Chapter 1, the FA in the *sn*-2 position is the one attached to the oxygen atom of the second carbon of the glycerol group, while the other tail is the *sn*-1 chain. The hydrogens attached to the second carbon in the FA tails in the *sn-2* position reproduce two experimental signals that are also differentiated in simulation data [8-12].

3.1.4 Sterol tilt

The tilt angle of the ring-plane was computed as described by Lim *et al.* [127]; additionally, the tilt angle of the sterol tail with respect to the bilayer normal (z-axis) was computed for the CHL/ERG comparison studies. The ring-plane was defined by a vector from C17 (base of the sterol) to C3 (carbon with the hydroxyl group), and the tail by a vector from C20 (first carbon in the tail) to C25 (the last carbon in the tail attached to two methyl groups). Atom names are the same as those shown in the sterol structures in Figure 2.

3.1.5 Sterol plane orientation

The spatial orientation of the sterol was analyzed in the CHL/ERG comparison studies by computing the frequency of contact between the carbon atoms in the two methyl groups on the rough face of the sterol and the lipid tails. CHARMM was used to count the number of times hydrogens from saturated and unsaturated tails were within 3 Å of C18 and C19 atoms in the sterol (the two methyl groups on the sterol's β-face, see **Figure 4**). These data were obtained and blocked averaged for the last 70 ns of equilibrated trajectory to determine a contact preference between the rough face of the sterol and a saturated or unsaturated environment (lipid tails).

3.1.6 2D Radial distribution function (2D RDF)

These distributions were used to better understand the lateral organization of lipids in membranes by measuring how the density of an atom varies with distance with

respect to a reference atom. This allows the analysis of lipid-lipid interactions on the x-y plane. The RDFs between the hydroxyl oxygen of all sterols in a given model over the equilibrated trajectory (last 70 ns of simulation) were computed for the symmetric models, and for several μs of trajectory in the asymmetric models. Additionally for the IPC ternary systems and the asymmetric models, 2D RDFs were calculated between the SM phosphorus atoms (the closest one to the lipid tail in the case of $M(IP)_2C$) and between the amine group of the SM lipids and the hydroxyl group of the sterol.

3.1.7 Lipid Relaxation Times

Reorientational correlation functions are of special interest for computational studies because they can be directly compared to NMR relaxation parameters [157]. A notion of bilayer dynamic motions can be obtained from axial relaxation time constants, which are measured by the second rank reorientational correlation function $C_2(t)$, equation (7), for specific atoms in the simulation data [158],

$$C_2(t) = \langle P_2\big(\hat{\mu}(0) \cdot \hat{\mu}(t)\big)\rangle \qquad \textbf{(7)}$$

where P_2 is the second Legendre polynomial, and $\hat{\mu}$ is a particular heavy atom-hydrogen vector.

The correlation function from simulation was computed defining a cross-chain vector between the first carbons of each FA tail (C22-C32) in the lipids of the CHL/ERG systems (see **Figure 12**). This vector was selected to estimate the slow

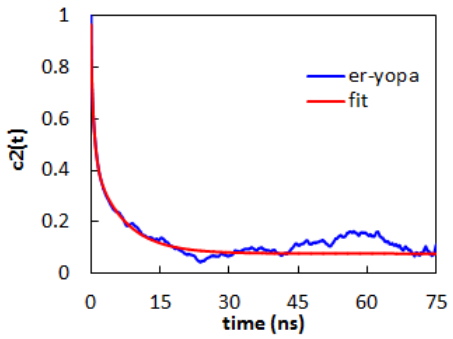

Figure 13 – Sample fitting for the correlation function $C_2(t)$ between the cross-chain vector (C22-C32 carbons) of YOPA lipids in the ER model (blue)

relaxation time, lipid wobble, instead of the true rotational motion [158]. A three exponential fitting was done to determine time constants for each lipid type in the membranes; equation 8 shows the general form of the fitting function. The three time constants obtained by fitting the simulated data correspond to the fast and slow relaxation times associated with the lipid's fast isomerization and wobble respectively [11].

$$C_2(t) = a_o + \sum_{i=1}^{3} a_i e^{-t/\tau_i} \qquad \textbf{(8)}$$

The independent coefficient a_o in equation 8 was estimated from the average value of the plateau reached by the correlation function over at least 35 ns of trajectory (see **Figure 13** for an example).

3.2 Membrane-protein systems

3.2.1 Binding events

Binding events were examined qualitatively using VMD to determine the time scale and bound configuration of the peptide and protein. In addition the interaction energies (ΔE^{bind}) between the peptide/protein and membrane were computed using Anton software 2.12.4 (a package based on Desmond) [124, 159]. Block averages were

computed between systems bound in the same conformation (horizontal vs. vertical), and compared between the simple and complex models. The peptide, each protein region (refer to Figure 5), the full protein, and the membrane were respectively defined as a separate groups in a DMS file (topology and parameters file in Anton and Desmond), and Anton computed the ΔE^{bind} between each group independently using the same settings as those used during the simulation. The reported values are estimates of the enthalpic contribution to the free energy of binding; the entropic contributions require far more sophisticated calculations and these were out of the scope of this study.

In addition to the qualitative analysis on VMD, this software was used to track the rotation of the main helix o the peptide about itself. A normal vector was defined for the non-polar face of the peptide (red arrow in **Figure 14**.**B&C**) and a time series generated to observe the orientation of the non-polar side chains as the simulation progressed with respect to the positive z-axis (blue arrow) (**Figure 14**.**A**). This figure also illustrates the definition of the helix tilt angle upon stable binding. As discussed in Section 6.1 the decrease in interaction energy time series shows more stable binding occurs when the non-polar face of the peptides is oriented towards the hydrophobic core of the membrane. Finally, EDPs, computed as described in the previous section, were used to show the peptide's location at the end of the simulation. The profiles were computed for the full protein, N-terminus (residues 1 to 7), C-terminus (residues 19 to 27), and main helix (residues 8 to 18) to compare the bound configurations observed in

the trajectories (refer to **Figure 5**). The phosphate region profile is also shown to facilitate comparison of the peptide location between the two bound conformations found in this study.

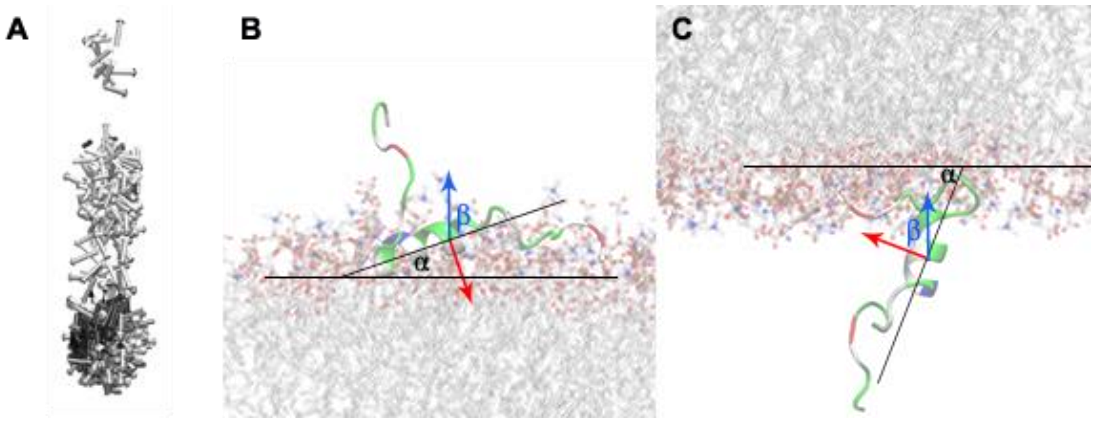

Figure 14 –Orientation of the ALPS-like motif with respect to the bilayer
(A) Time progression (white to black) of the side chains as the peptide interacts with the bilayer; the arrow represents the normal vector to the non-polar residues for the z-nvt trajectory as an example. (B) Definition for **α**, the helix tilt angle with respect to the membrane surface upon stable binding; and **β** the angle between the normal vector to the non-polar face of the peptide (red arrow) and the bilayer normal (solid red line) for a trajectory where the peptide bound to the top leaflet (z-nvt), and the (C) bottom leaflet (o-npt)

3.2.2 Protein-lipid interactions

The frequency of contact of each amino acid in the ALPS-like motif was computed during the last microsecond of simulation and blocked averaged every 60ns. CHARMM was used to count the number of times phosphorus atoms from the membrane where within 5Å of the peptide's heavy atoms (center of mass of each residue) as well as the C_α atom of each peptide residue. Averaged values between all the simulations sharing a binding conformation (horizontal vs. vertical/tilted) are reported in Chapter 6, these are compared between the simple and complex models.

Similar analysis was carried for the full protein; non-hydrogen protein-membrane atoms within 10 Å of each other were counted after stable protein binding for all the residues studied in experimental cysteine-replacement cross-linking studies performed by Schulz *et al* [95]. These residues were also examined on a previous computation study that also obtained matching results to experimental data [97]. The contact distance of 10 Å was selected to mimic the distance required for experimental cross-linking between a cysteine in the protein and a liposome.

3.2.3 Peptide structure

Helical character was determined using CHARMM as the percent of amino acids with this secondary structure, data was collected every 0.2ns for the entire trajectory and then blocked every 10ns. Comparison was done between horizontal and vertical bound conformations as well as between simple and complex systems. The tilt angle of the main helix with respect to the membrane surface was also computed for the last microsecond of simulation to corroborate the bound conformation of the peptide. Results were averaged across systems sharing a bound conformation. The main helix vector for these measurements was defined between the alpha carbons of residues SER8 and SER18. The tilt angle was measured between the vector defining the main helix of the peptide and the bilayer normal, then subtracted from 90° to obtain the angle between the main helix and the membrane surface.

3.3 Water-oil systems

3.3.1 Interfacial tension

The interfacial tension was calculated from the components of the pressure tensor at each time step using equation 9 and blocked averages reported in Chapter 7.

$$\gamma_{simulation} = {}^{P_{plane\ of\ contact}}/_{L} = \frac{L_z}{2} * \left(P_{zz} - \frac{(P_{xx}+P_{yy})}{2}\right) \quad \textbf{(9)}$$

This measurement was compared against experimental trends for ternary systems with TBA and other small alcohols and different organic phases (figures included in Chapter 7). Direct comparison was available with experimental measurements from collaborators in Russia who used the Wilhelmy plate method to measure the interfacial tension of ternary systems with the same TBA overall concentrations as the simulation systems. Measurements with higher TBA concentration, approaching the critical point of the ternary system, were performed using the spinning drop method.

3.3.2 Hydrotrope structure at the interface

Hydrotrope orientation at the interface was characterized according to the tilt angle between the z-axis and the vector defined by the carbon to which the hydroxyl group is attached and its oxygen. Additionally, 2D RDFs were computed between the oxygens in the alcohol molecule to examine patterns in the lateral organization of hydrotropes.

3.3.3 Thickness of the interface

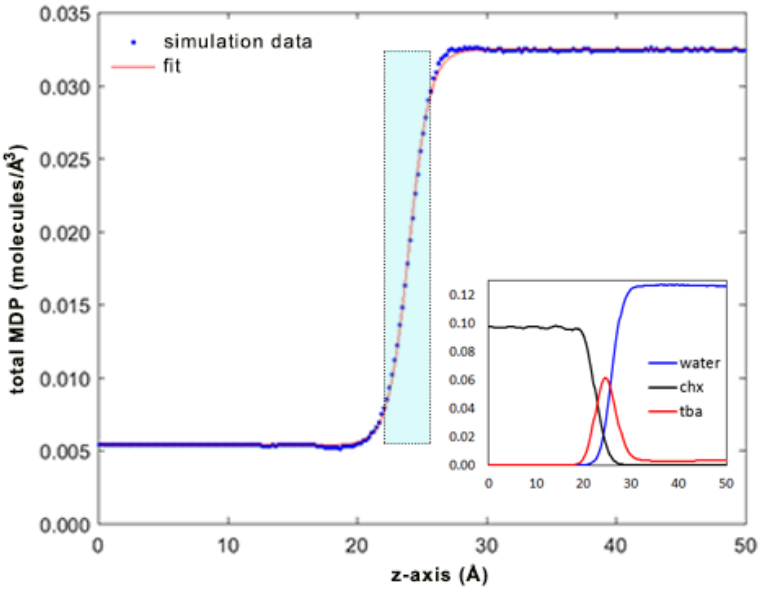

Figure 15 – Sample curve fitting to estimate the thickness of the interface (cyan box) The ADP for this system (S1) is shown in the insert as an example of the location of each species in the simulation box at equilibrium.

Atom density profiles (ADP) were computed using CHARMM in similar fashion as the EDPs for membrane simulations. These were used to study the thickness of the interface with decreasing interfacial tension (i.e. increasing hydrotrope concentration) Symmetrized molecule density profiles (MDP; atom density profiles (ADP) divided by the corresponding number of atoms per molecule) were used to estimate the interfacial thickness by fitting a hyperbolic tangent function to the total density profile (see **Figure 15**) following the van der Walls (VDW) theory of smooth interfaces [160]. The MDP profiles were recentered to have the center of the interface in the simulation box at the origin of the Cartesian coordinates. Equation 10 describes the fitted function, where *z*

is z-axis coordinate of the simulation box, ζ is the characteristic length of the thickness of the interface (*thickness=2* ζ)*, Δρ is the density profile, and $\Delta\rho_o$ is the difference between the bulk densities of the liquids. The characteristic length of the interface, ζ, approaches the correlation length of the fluctuations of the interface (ξ) as the mixtures approaches its critical point, but it is not the same far away from it.

$$ADP_{fit} = \Delta\rho = \Delta\rho_O * tanh\left(\frac{z}{\zeta}\right) \qquad \textbf{(10)}$$

Relationships between the interface thickness and $\Delta\rho_o$ were computed to corroborate theoretical expressions; and a universal density profile was derived by reducing Δρ and *z* by $\Delta\rho_o$ and ζ (plots are shown in Chapter 7). One of the theoretical relationships suggested by VDW states the inverse of the thickness of the interface has a linear dependence on the square root of the interfacial tension near the critical point of a given mixture [161]. This relationship was examined based on both experimental and simulated mixtures both near and far away from the critical point. The results are discussed in Chapter 7.

Chapter 4: Symmetric Membrane Simulation Results

4.1 Symmetric Yeast ERG/CHL

The following results summarize the behavior of the simulated systems to examine the effect of CHL versus ERG in a bilayer. The analysis was done in the last 70 ns of simulation for each trajectory; the results were block-averaged for each replicate, and averaged values between the replicate runs are reported with their respective standard error. The results are independent of initial lipid configuration on the x-y plane.

4.1.1 Lateral Membrane Properties

Table 5 – Lateral membrane properties for the symmetric models with ERG and CHL
Average and standard error of the surface area per lipid, compressibility modulus, and sterol tilt angle (values calculated from the time series of equilibrated data).

	model	SA/lipid (Å^2)	SA/sterol (Å^2)	KA (N/m)	ring plane tilt (º)	sterol tail tilt (º)
ERG	er	63.6 ± 0.4	25.1 ± 0.3	0.28 ± 0.02	25.1 ± 0.7	39.9 ± 0.5
	tgn	60.9 ± 0.4	32.0 ± 0.9	0.27 ± 0.02	23.9 ± 0.2	37.2 ± 0.3
CHL	er	63.6 ± 0.4	33.4 ± 1.5	0.40 ± 0.07	24.5 ± 0.3	38.1 ± 0.7
	tgn	60.9 ± 0.3	22.6 ± 0.1	0.36 ± 0.07	22.6 ± 0.4	36.3 ± 0.1

The CHL systems started from an equilibrated configuration of the models containing ERG; thus, the new systems reached equilibrium in the first 25 ns of simulation. **Table 5** summarizes the results for the overall SA, sterol surface area, K_A,

and sterol tilt angles (ring-plane and tail) for each membrane. There is no statistical difference between the overall surface area between the ERG and CHL systems, probably due to their low to moderate concentrations in the ER and TGN models respectively. There is, however, a difference between their K_A values; the models with CHL have 42% and 33% larger K_A than those with ERG in the ER and TGN respectively (**Table 5**). In addition, the CA analysis reveals the structural differences between ERG and CHL does impact their individual areas per molecule (see **Table A.1**). These values vary in opposite direction for CHL and ERG depending on membrane model (unsaturation degree); ERG hast a larger CA than CHL in the TGN, a more unsaturated environment, but a lower CA than CHL in the ER, which has 10% more saturated lipid tail than the TGN model. This results contradicts experimental results [62, 162] that concluded CHL induces more condensation than ERG. It is important to know that, as mentioned repeatedly in the literature [60, 62], unsaturation degree is not the only variable on sterol-lipid interactions; lipid headgroup also influences the dynamics of the sterol molecule and modulates the location of the molecule in the membrane core. Most experimental and simulation studies have been done using the PC headgroup, but limited work has been done with membranes containing PE or PS lipids [60], i.e., headgroups included in the models presented in this study.

4.1.2 Sterol tilt

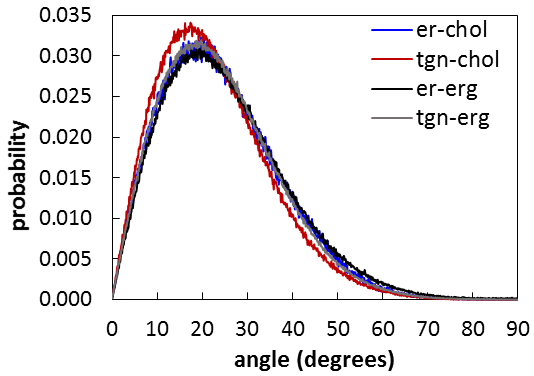

Figure 16 - Average sterol tilt angles for all membrane models
(angle between the bilayer normal and the sterol vector defined from the carbon at the base of the molecule to the carbon with the hydroxyl group, C17-C3)

There is no statistical difference between the tilt angles of the sterol tails in the ER and TGN models with either ERG or CHL, (p-values of 0.40 and 0.17 respectively). Yet, the orientation of the sterol ring-plane in the CHL-containing models seems to be slightly more vertical with respect to the bilayer normal (z-axis) than the ERG models. The same trend is observe for the sterol tails, they are more tilted with respect to the bilayer in the ERG models possibly due to its extra double bonds. **Figure 16** shows the sterol ring-plane tilt angle probability distributions for all the systems in this study and Table 4 lists the average values.

The average ring plane angles are lager in the ERG models, expected due to additional double bonds in its structure that make the ring more rigid and educe tail flexibility. Even though there is no statistical difference between the average tilt angles in the ER or TGN with the respective sterol molecule, the angle decreases (i.e. the molecule aligns better with the vertical axis) with increasing sterol content as expected. The sterol molecules cause a more ordered environment due to their interaction with the lipid tails (straightening). Sterol tilt seems to also be modulated by the methyl

groups on the rough face of the molecule [56, 59]. The α-face of the sterol tends to interact more with fully saturated lipid tails, while the methyl groups on the β-face prefer to be in a more unsaturated environment [47]. **Figure 17** shows the frequency of contact between the methyl groups on the β-face (C18 and C19) with either saturated or unsaturated tails. In agreement with known trends, the unsaturated chains have more interaction with the rough face of the sterol, while the smooth face interacts with saturated tails with comparable frequency across all systems [47].

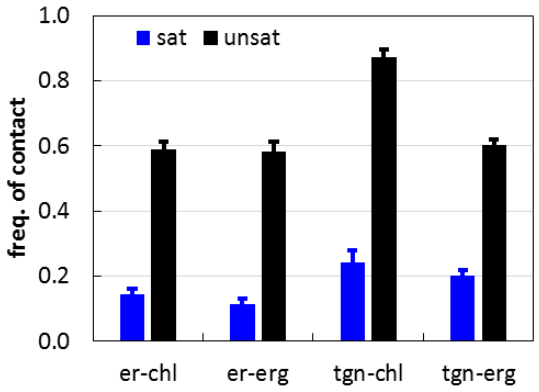

Figure 17 – Frequency of contact between the sterol's β-face and lipid tails.

4.1.3 Electron density profiles

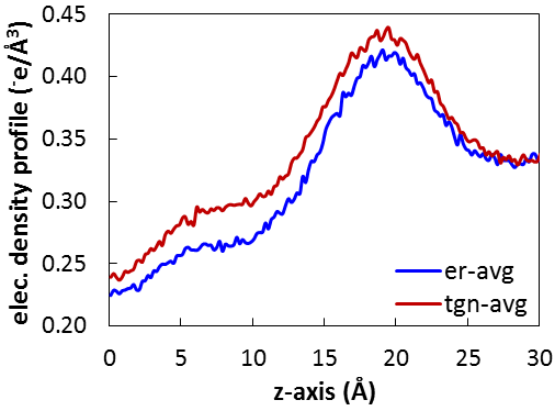

Figure 18 - EDPs for the ER and TGN models with cholesterol

Figure 18 shows the symmetrized EDPs for the ER and TGN systems with CHL; these profiles result from the summation of the individual lipids EDPs and that of water. D_{HH} was estimated from the peak values of each profile in this figure. **Table 6**, summarizes the bilayer thicknesses

for all systems (ERG and CHL models). From the D_{HH} thickness there is a slight increase in membrane thickness for the CHL models, in agreement with experimental and computational trends of CHL [53, 163] having a condensing effect on the bilayer, making it stiffer (higher K_A) and thicker. This difference is more noticeable in the ER models, which contain 13% more saturated FA than the TGN models. Unsaturation degree in the bilayer also influences the effect of sterol type on membrane properties; for example, $2D_C$ increases with increasing sterol concentration and even more so with CHL than with ERG.

Table 6 – Bilayer thicknesses D_H-H, DB, and 2DC for the models comparing sterols
The estimates from the OPM database, compared with the simulation 2DC, were averaged among those available for the ER membranes of yeast S. cerevisiae and Homo sapiens to compare with the ERG and CHL models respectively.

	model	D_{H-H} (Å)	D_B (Å)	$2D_C$ (Å)	Hydrophobic thickness (OPM)
ERG	er	37.8 ± 0.1	34.1 ± 0.2	29.1 ± 0.2	29.6 ± 0.2*
	tgn	38.4 ± 0.1	35.8 ± 0.2	29.7 ± 0.2	-
CHL	er	39.0 ± 0.8	33.5 ± 0.4	26.4 ± 0.4	31.7 ± 1.3**
	tgn	38.8 ± 0.2	35.6 ± 0.4	27.9 ± 0.4	-

(* average between PDBIDs: 2wwa, 2ww9, 4wmz, 5eqb; **average between PDBIDs: 5fn4, 5fn3, 5gky, 4uis, 5a63)

While there is almost no change in the hydrophobic thickness between the ER and TGN models containing ERG, $2D_C$ increases in the CHL systems with larger sterol concentration ($2D_{C\text{-}TGN} > 2D_{C\text{-}ER}$). Additionally, the hydrophobic thickness is higher in the ERG systems, contrary to the stronger condensation effect of CHL vs. ERG shown by D_{HH} and data trends available in the OPM database [156]. Estimates for the hydrophobic thicknesses in the OPM are predicted by the crystal structure of

transmembrane helices (last column on Table 2), and can be directly compared to our estimates of $2D_C$. The estimated thicknesses from the OPM for the ER of yeast are a good reference for our ER-ERG model because it is the same reference organism. This is not the case for the ER-CHL model; the proteins selected to evaluate our estimate are from human ER membranes (more saturated environment), which have different lipid composition than yeast ER. Therefore, the OPM estimate for the ER-CHL model, 31.7±1.3 Å is not a precise reference for the hydrophobic thickness of the CHL models, but it rather gives an idea of the membrane-sterol effect in a bilayer. This last trend seem to be more related to the membrane environment. There is a 9% reduction in $2D_C$ in the ER model (70% unsaturation) and 6% reduction for the TGN (80% unsaturation), in agreement with experimental studies on pure-lipid-sterol membranes that concluded increase unsaturation in a bilayer mitigates cholesterol's effect in the mechanical and structural properties [162].

4.1.4 Deuterium order parameters (S_{CD})

Comparison of the S_{CD}s between the ER and TGN models show there is more order (higher parameter value) for the lipids in the TGN model despite its higher unsaturation degree (**Table A.2**). The higher order results from the TGN's sterol content, i.e., more than twice than that in the ER models. Moreover, the parameter values between the CHL and ERG models show that CHL induces more order than ERG in lipids where both FAs tails are monounsaturated. The C10-C18 values in the *sn-2* tail in DYPE lipids

and *sn*-1 tail in POPI lipids as well as the C2-C9 values in the *sn-2* tails of YOPA and DYPE lipids in the ER-ERG model have lower values. There is no statistical difference among the S_{CD}s of the fully saturated tail in POPI, PYPI, and POPS lipids. **Figure 19** shows sample S_{CD}s for YOPA in all models as it is one of the systems that better shows the differences in bilayer order that arise from lipid diversity, unsaturation, and sterol content.

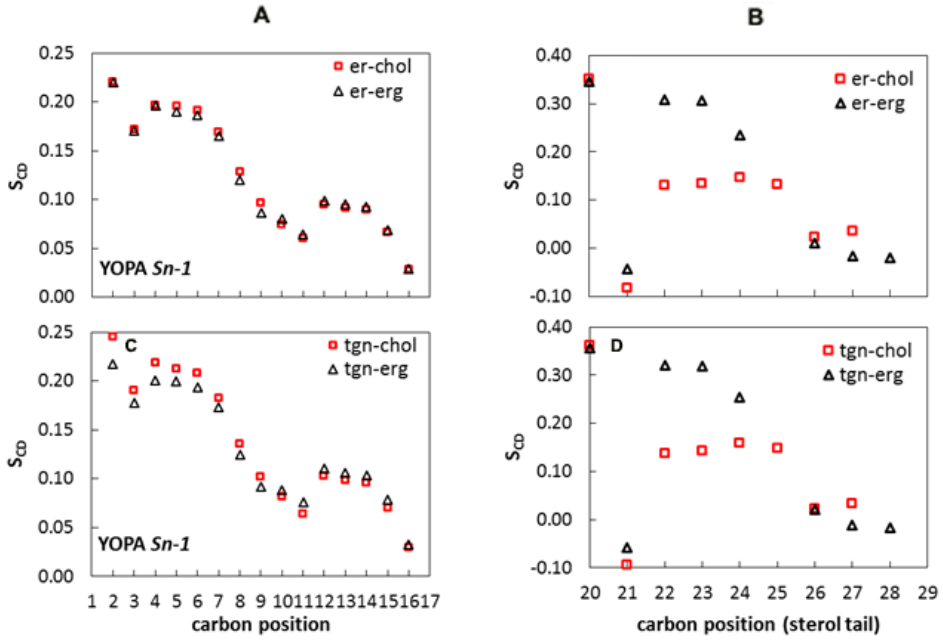

Figure 19 – S_{CD} values in the ER and TGN models with ERG and CHL
Comparison for the (A) sn-1 chains of YOPA in the ER and TGN models with ERG and CHL respectively, and between the (B) sterol tails.

Moreover, **Figure 19** also shows the order parameters for the sterol tails (carbon numbering shown in **Figure 2**). There is no statistical difference between the values of the closest carbon to the ring plane, C20, which has the highest order parameter being

the one that is more restricted to move. As expected, the methyl groups have the lowest parameter values, and the alkene groups' values in between the two extremes. Similar to the lipid tail parameters, the TGN model S_{CD}s for the CH_2 carbons are higher than the ones in the ER for either sterol type. As expected from its chemical structure (more rigid ring plane and tail), the ERG tails have higher S_{CD}s (CH_2 groups) than those in the systems containing CHL.

4.1.5 Sterol plane orientation

The sterol's ring plane is located in the middle of the hydrophobic region of the bilayer, interacting directly with the lipid tails. Examination of the environment around the ring plane shows sterols, independent of type and concentration in the bilayer, prefer to orient themselves with their β-face facing unsaturated FA. CHL is a more saturated molecule than ERG, when present in low concentration there is no statistical difference vs. the ERG systems in the frequency of contact with either saturated or unsaturated lipids (95% confidence interval). However, at moderate concentration (>10 mol%) there is more interaction with unsaturated lipids between the β-face of CHL than that of ERG (p-value=0.011). Typically sterols rather interact with a saturated environment, which drives sterol-rich domain formation. The interaction of sterols with saturated lipids has no statistical difference between each model with ERG and CHL respectively (refer to **Figure 17**).

4.1.6 Radial distribution functions

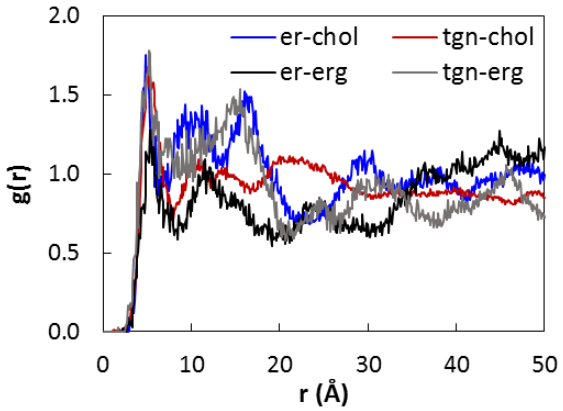

Figure 20 - 2D RDFs for the hydroxyl groups interactions among sterols

The 2D RDF computed for these systems indicate there is no preferred lateral organization for CHL over ERG in their immediate vicinity. There are not, however, a measure of sterol clustering due to the short time scale of these trajectories and lack of sphingolipids in the models (important molecules in cluster formation). **Figure 20** shows the first solvation shell around 5.3±0.2 Å for the ERG systems and 4.9±0.2 Å for the CHL systems, which suggests that the ERG's unsaturated tail increase the distance of sterol contact. There is a second solvation shell for the ERG systems between 12 and 15 Å, whereas this shell is around 10 Å for the CHL systems. Additionally, there is a third shell for the CHL systems between 14 and 16 Å. These second and third shells suggest that CHL has a strong preference to form clusters that are linear due to the shell being multiples of 5 Å and similar to web-like structures found from simulations of membranes with high concentrations of sterol [164].

From the sterol-sterol interactions described by 2D RDFs, the first solvation shell in **Figure 20** suggest hydrogen bonding between close-by molecules, and the second and third shells in the CHL systems could be indicators of a parallel configuration

between close-by cholesterols. Interestingly, there is no solvation shell in the ERG systems corresponding to the second shell of CHL, possibly due to the double bond in the sterol tail that makes the molecule more bulky and less favorable for a parallel organization with neighboring ergosterol molecules. The distance of the first solvation shells in **Figure 20** are of comparable magnitude with a study of CHL-DPPC (20-80 mol%) [59] that examined sterol-sterol interactions with 2D RDFs between their center of mass.

4.1.7 Lipid Relaxation Times

Table 7 – Lipid wobble times (ns) derived from the cross-chain correlation function. Longest time constant in the 3-exponential fitting to the $C_2(t)$ correlation between cross-chain carbons, C22-C32 in each lipid tail according to CHARMM topology file nomenclature.

	ER	TGN
ERG	9.70 ± 3.29	11.50 ± 2.59
CHL	7.26 ± 1.27	6.42 ± 1.14

Table 7 lists the longest relaxation time constant from the 3-exponential fits to the $C_2(t)$ correlation function from simulation data (**Table A.3** lists all the time constants); these correspond to the lipid slow rotational motion known as wobble. The cross-chain (CC) vector defined between C22-C32 carbons on the *sn-2* and *sn-1* tails, respectively provides a better idea of lipid wobble (slow rotation) according to the study presented in [158]. The current results show lipid wobble is slower in ERG systems (longer relaxation time) by at least 30% vs. the CHL systems, which can be attributed to the extra double bonds in ERG ("bulkier" molecule) as well as the higher order induced by CHL in the bilayers.

Based on the CA of each lipid, which increased for all lipids when substituting ERG with CHL, lipid wobble times should be smaller for the CHL systems given they have more space to move. From Table 6, this is precisely the case for our systems, lipid wobble decreased at least 25% in the CHL systems vs. those with ERG. However, increasing sterol content had no effect in the ERG and CHL models. The weighted average lipid wobble in the ER and TGN are not statistically different within a 95% confidence interval. Individual lipid wobble followed the same trend, but monounsaturated lipids had larger wobble times for the ER-CHL model vs. that with ERG.

4.2 Symmetric models with IPC lipids

4.2.1 Lateral organization

Ternary systems of IPC/ERG and a third lipid (POPI or POPC) were simulated to examine the effect of this third lipid in the interaction between the sphingolipid (IPC) and the sterol (ERG). PI is a bulkier lipid headgroup, and therefore occupies more space in the bilayer; however, the SA of each membrane, reported on **Table 8**, has no statistical difference between the models with either POPI or POPC lipids. Interestingly, the K_A is affected by the third lipid (POPI/POPC); both models have the same degree of unsaturation in their lipid tails, but the lipid headgroups plays a relevant role in the fluidity of the membrane.

Table 8 – Surface area and K_A for the IPC ternary models

Model	SA (Å^2)	K_A (N/m)
PI-IPC	41.48 ± 0.82	3.57 ± 0.25
PC-IPC	40.94 ± 0.20	2.75 ± 0.32

This can be attributed to the effect of POPI or POPC on the lipid-lipid interactions in each bilayer. Figure 21 shows 2D RDFs computed between IPC-POP*X*, IPC-IPC, ERG-ERG, and IPC-ERG respectively. Panel A shows there is similar interaction between IPC and POPI or POPC lipids. The RDFs were computed between the phosphate atoms of each lipid; the slightly higher distribution for the IPC-PC system could indicate electrostatic interactions between these two lipids are stronger, but it may be more related to the structure of the lipids and steric hindrance. The PI headgroup requires more space and is more rigid than the linear PC headgroup. P-P interactions between IPC-PC may be easier because there is simply more space for them to get closer. For this same reason, as observed in panel C in the same figure, IPC lipids in the PC model have more opportunity to interact with one another, and thus the first solvation shell of the IPC-IPC distribution is higher than the same distribution for the PI model.

A more interesting effect is observed in the ERG-ERG interactions as shown by the O-O interactions on Figure 21.**E**. While the interaction distance remains the same, the frequency is higher for the first solvation shell association of sterols in the PI model. Panel F shows a sterol cluster with interacting distances that are within the first two solvation shells of this distribution. The two crests in the RDF peak seem to arise from

the sterol's spatial orientation with respect to the sterols around it. The β-faces of the sterols in the sample cluster can either align in a clock-wise fashion, or face another β-face, which corresponds to the second crest in the first peak of the distribution. As far as the ERG interaction with IPC, as shown in panel G, the third lipid has minimal influence in the strength and frequency of this interaction. Both distributions, for POPI and POPC, follow the same trend, but there is an additional interaction shell in the PC systems. This small peak in the PC distribution could arise from hydrogen bonding between the sterol and IPC, with any of the four hydroxyl groups (two in the SM chain, and two in the FA chain). There is more accessibility to IPC in the PC model because this is a less bulky headgroup that would allow the sterol to interact with IPC in different orientations. Examining the 2D RDFs between the center of mass of the inositol rings in IPC and PI could provide additional details in ring-ring interactions that prevent IPC-ERG interactions in this model.

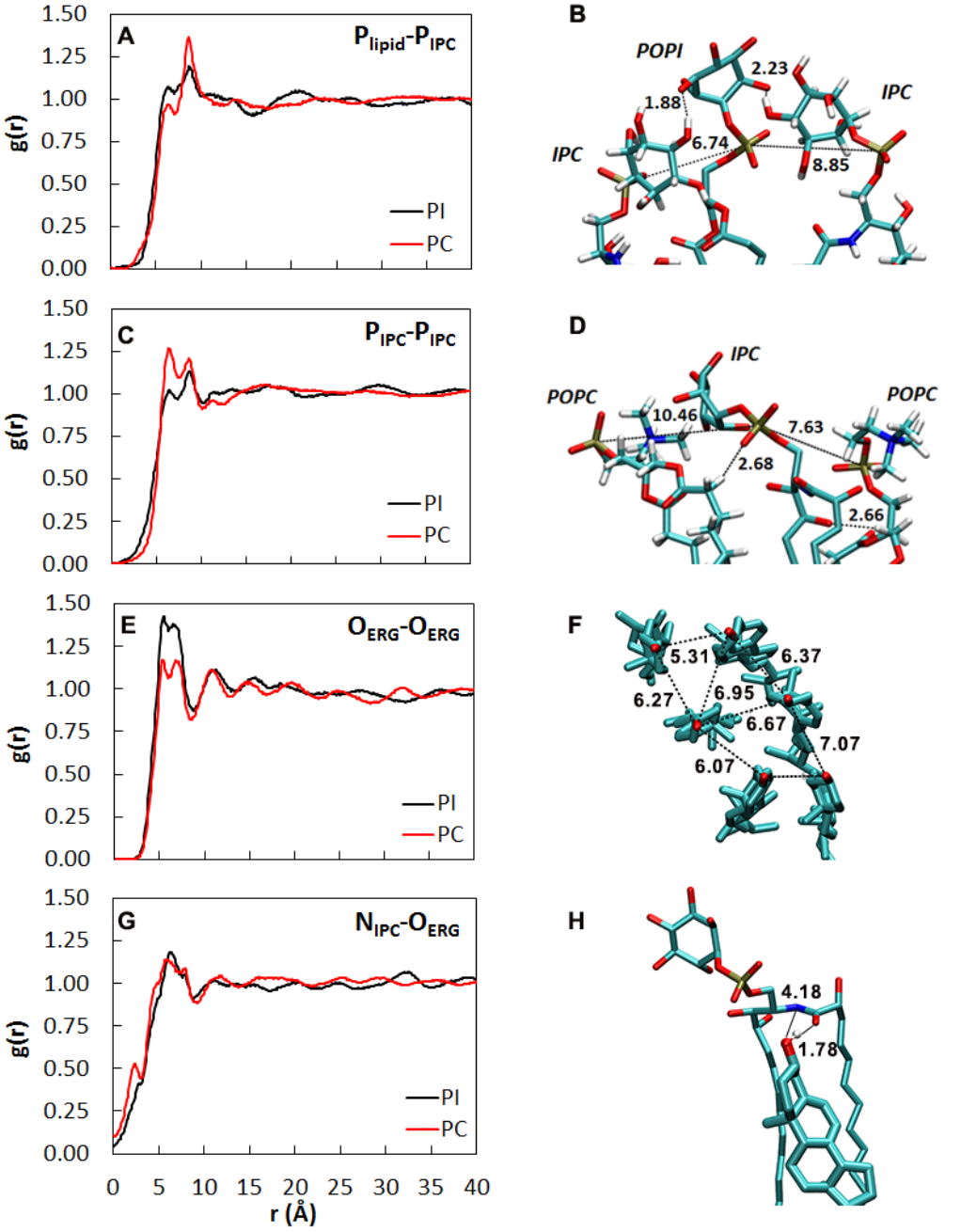

Figure 21 – 2D RDFs among IPC-PI/PC lipids
Inter-lipid interactions between the phosphorus atoms of (A) IPC-POPI and IPC-POPC lipids; (C) IPC lipids; (E) Hydroxyl oxygens of ERG; (G) IPC-ERG molecules. (B) and (D) show the interaction between IPC and POPI and POPC lipids respectively; (F) and (H) show interacting ERG-ERG and IPC-ERG lipids.

4.2.2 Membrane structure

It is well known that sterols induce order in a bilayer [49, 53]. Membrane systems built on CHARMM-GUI have lipids randomly placed in the simulation box with the sole constraint of being in a bilayer conformation. During initial equilibration, these relax into a more natural configuration, but they are still a random mixture of lipids. During the simulation trajectory, the system equilibrates and lipids reorganized as they interact with their neighbors. Figure 22 shows this for one of the PI systems in this study; initially the lipid tails are randomly mixed and disordered, but by the end of the simulation the tails have ordered due to the high sterol content (33 mol%) and also because of their interactions with the fully saturated IPC tails. As it was discussed in Section 4.1, both the sterol type and the membrane environment modulate sterol-lipid interactions and their influence on membrane properties. The sterol's ordering effect is also related to L_o and L_d phase coexistence; sterol rich domains are more ordered (gel-phase like) and known as the L_o phase, and the sterol depleted regions as L_d.

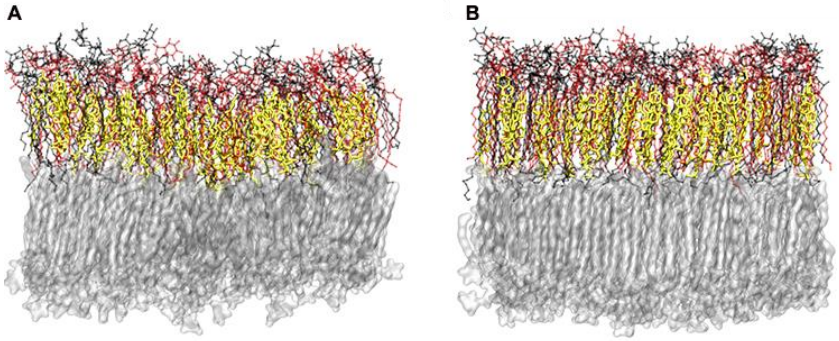

Figure 22 – Lipid chains ordering effect
(A) Beginning and (B) end of the simulation; ERG (yellow), IPC (black), POPI (red); bottom leaflet shown in gray. Snapshots were taken from the PI system

As shown in **Figure 23**, the sterol (shown in yellow) lies between regions of IPC (black) and POP*X* (red) lipids. This results from the sterols' preference to associate with fully saturated lipids like IPC. **Figure 24** shows there is a distinctive preference for ERG to orient its β-face (with two methyl groups sticking out of the ring plane) towards saturated lipid tails; which was also observed in the studies of the yeast models

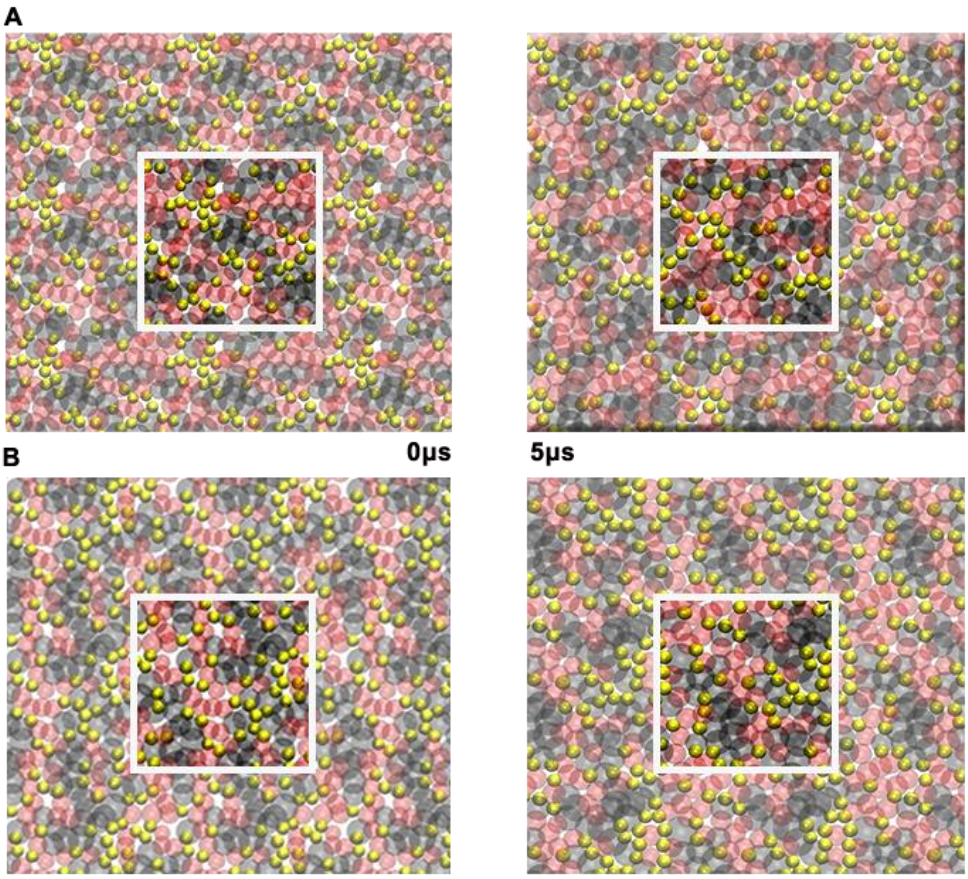

Figure 23 – IPC-ERG domains at the beginning and end of the simulation
The main simulation box is shown by the white square, the rest of each image shows the image atoms for each system to better show the lipid organization.
(A) PI system, (B) PC systems; ERG (yellow), IPC (black), POPI (red)

or the ER and TGN organelles (Section 4.1). There was no statistical difference, within a 95% confidence interval, between the frequencies of contact of the β-face or ERG in the PI or PC models.

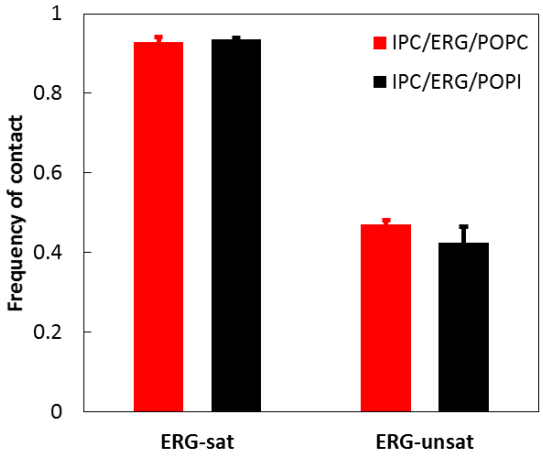

Figure 24 – Frequency of contact between ERG and lipid tails

Nonetheless, it is interesting to note in **Figure 23.B** sterols are more prone to be at the border of IPC-rich regions in the PC system, in agreement with the literature [21]. As mentioned before, the 2D RDF between the IPC amine and the hydroxyl oxygen in ERG has an additional peak around 2.5 Å for the PC system that the PI distribution does not have. ERG-IPC interactions may be facilitated in the PC system more than in the PI systems due simply to having more space to interact. An additional variable in the frequency of interactions between ERG and IPC could be interactions between POPI lipids and ERG. If there are ERG-POPI interactions that compete against ERG-IPC domain-forming interactions, it would explain why the sterol resides at the interface between POPC and IPC better than between POPI and IPC.

Membrane order as expressed by S_{CD}s from simulation was not in agreement with experiment, but showed the opposite trend: more order in the PC containing model [21] (**Figure 25**). The experimental measurements looked at equimolar mixtures of IPC,

ERG, and PI or PC lipids from yeast extracts, but the FA tails for yeast extracts vary and may influence overall lipid order in a different way compared to the IPC/ERG/POP*X* models. It is likely that some discrepancies between this work and the experimental results are due to the use of a different lipids.

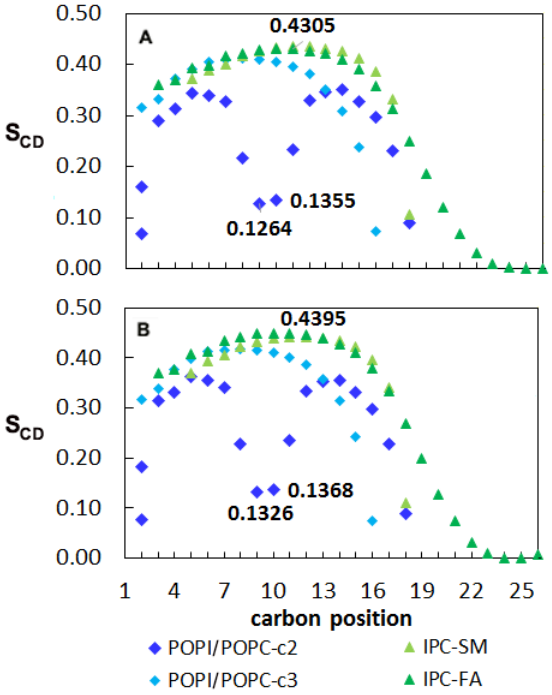

Figure 25 – Order parameters for the IPC ternary systems (A) IPC/ERG/POPI system, (B) IPC/ERG/POPC systems. Maximum and minimum values of the S_{CD} are shown for each systems. Standard errors of these values are of the marker size, or smaller.

ERG-rich domains are known to exist with fully saturated lipids, mainly SM lipids in biological membranes [25, 165, 166]; one of the reasons why there were no domains observed in the symmetric TGN or PM models previously published with lack of lipids with fully saturated tails [27]. Different from the symmetric studies of the ER and TGN models discussed in the previous section, the β-face of ERG in the IPC models was in contact with saturated lipids nearly twice as much as with unsaturated lipids (see **Figure 24**). This arrangement facilitates domain formation with ERG residing at the interface between IPC and the third component. This location allows for the sterol's α-face to interacting

with unsaturated FA, also noticeable in the end-of-simulation snapshots in **Figure 23**. As a result, the methyl groups in its ring plane are in a more suitable (saturated) environment and stabilize lipid domain formation.

The EDPs for these ternary models, shown in **Figure 26**, are very similar. The sterol molecules are situated well inside the hydrophobic core of the membrane, and the POPC groups have a narrower densify profile than the POPI groups as expected (size-wise in the horizontal axis). Interestingly, the interdigitation of the long SM tails from IPC is not as notorious as anticipated. Notice the profile for IPC lipids has a peak at the center of the bilayer, resulting from the bending of several 26-carbon chains in between the leaflets. This is also seen in Figure 22, where the long black tails of IPC are folded at the center of the bilayer and only a few stretch into the other leaflet. There is still analysis to be done to distinguish the percentage of tails that remain in between the leaflets from the tails that do interact with the opposing leaflet.

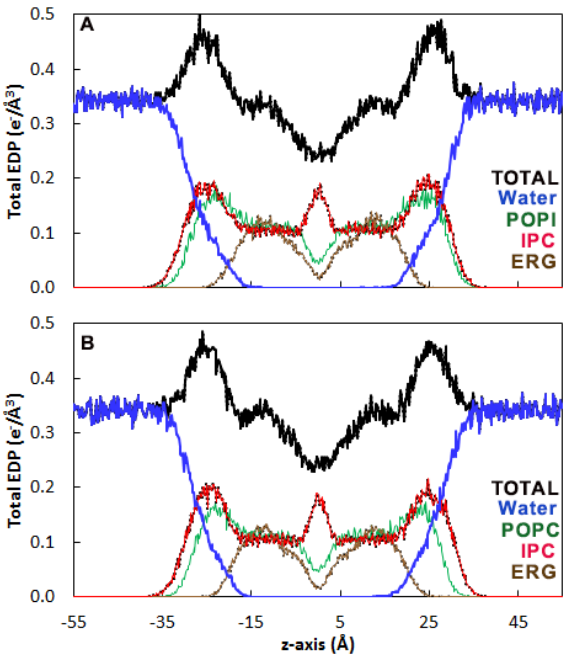

Figure 26 – EDPs for the symmetric IPC models

Chapter 5: Asymmetric Membrane Simulation Results

5.1 Membrane Structure

5.1.1 Leaflet organization

Asymmetric models for the PM and TGN were simulated to examine lipid phase coexistence, domain formation, and interleaflet coupling.

Table 9 lists the overall SA per leaflet in each model as well as the SA of the previous symmetric models for both the PM and TGN as reference. Models 1 and 2 of the symmetric systems only differed in saturation degree by 6.3% in the TGN and 9.4% in the PM. The equilibrium unsaturation degree for the cytosolic and non-cytosolic leaflets in the asymmetric models is also listed in **Table 9**. Notice the reduction in unsaturation degree in the cytosolic leaflet in both models is related to the sterol content in the leaflet. **Figure 27.B** lists the initial and final sterol concentrations per leaflet averaged between the two replicates for each model, and **Figure 27**.**A** shows the time series for this exchange. Sterols were counted at every frame in the simulation using CHARMM; the molecules were selected above and below the center of the bilayer with a buffer of 7 Å for the top and bottom leaflets respectively. The center of the bilayer

was defined by the average position of the membrane in the z-axis of recentered trajectories; these were also used to calculate the EDPs discussed in Section 5.1.3. There is still sterol flip-flop taking place at the end of the simulations, but it is already at equilibrium (same amount of sterols being exchanged between leaflets).

Table 9 – Comparison of overall SA in asymmetric models (at equilibrium)

	Initial unsat. fraction	Final unsat. fraction	Avg. SA (Å^2/lip) (symmetric)	Avg. SA (Å^2/lip) (asymmetric)	previous symmetric models [27]	
PM-cyto	0.67	0.60	53.74 ± 0.10	53.46 ± 0.02	PM1	47.42 ± 0.25
PM-noncyto	0.59	0.68	47.77 ± 0.43	42.08 ± 0.02	PM2	46.76 ± 0.30
TGN-cyto	0.70	0.66	63.18 ± 0.09	58.30 ± 0.02	TGN1	60.56 ± 0.36
TGN-noncyto	0.89	0.85	56.16 ± 0.11	56.14 ± 0.02	TGN2	60.95 ± 0.36
PM-cyto	0.67	0.60	53.74 ± 0.10	53.46 ± 0.02	PM1	47.42 ± 0.25

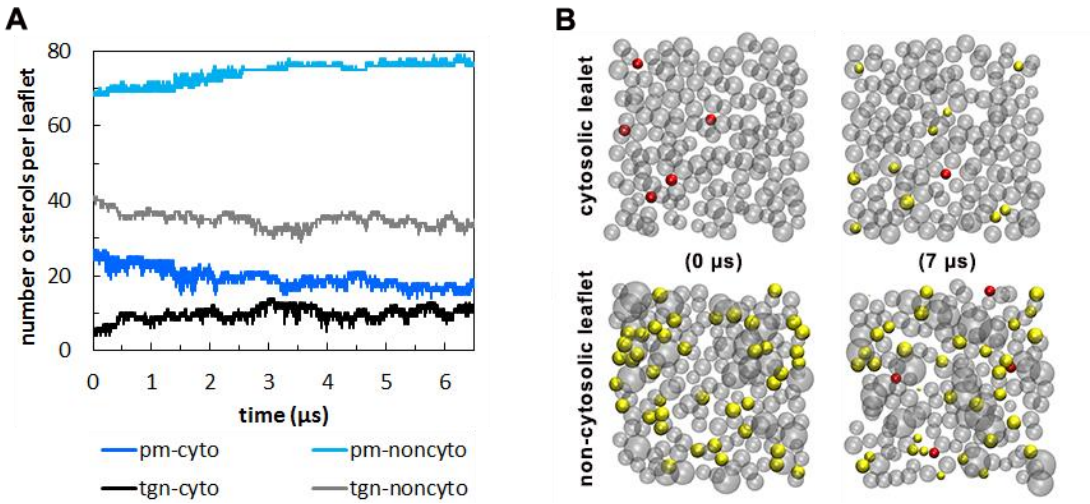

Figure 27 – Sterol exchange between asymmetric leaflets
(A) Time series of ERG in each leaflet; (B) Beginning and final location of sterols in the cytosolic (red spheres) and non-cytosolic (yellow spheres) leaflets in the TGN model.

Table 10 - Change in sterol composition in the asymmetric models

	PM-cyto	PM-noncyto	TGN-cyto	TGN-noncyto
initial sterol %	21.64	46.21	3.33	24.40
Final sterol %	13.93	49.68	7.05	21.60

Figure 27.**B** has snapshots of the initial and final sterol molecules in each leaflet for one of the TGN replicas. The sterol flux is higher towards the cytosolic leaflet in this model, and results in an increase in sterol content in this leaflet. The overall sterol content in the TGN is 42% of that in the PM that has 34.41% ERG content in total. The sterol exchange in the TGN results in all sterol molecules in one or the other leaflet; however, the higher sterol content in the PM results in an equilibrium exchange that leaves on average two sterol molecules at the center of the bilayer that lie horizontally in between the leaflets. Additional analysis is required to quantify the interaction between the horizontal sterols at the center of the bilayer with SM lipids tails, if any. Subsequent analysis of these models was done only in the equilibrated section of the trajectory as established by stable sterol exchange between leaflets.

5.1.2 S_{CD}

The average order parameters were examined in both models; sn-1 and sn-2 tails in the IPC and $M(IP)_2C$ lipids were set to be the sphingomyelin and FA chains respectively (see **Figure 28**). From these values there is more order in the PM, which agrees well with the equilibrium unsaturation degree, i.e. larger unsaturation degree results in a less ordered bilayer. There is also more sterol in both leaflets of this model, which will increase the overall order in the bilayer. **Table 11** lists the weighted average

S_{CD}s for the symmetric templates for the cytosolic and non-cytosolic leaflets along with the values for the asymmetric leaflets at equilibrium. At first glance, the order parameters for the asymmetric models are higher in the cytosolic leaflet, in agreement with a more saturated environment in this leaflet upon equilibration (refer to **Table 9**). Sterol certainly influences membrane order, but also the unsaturation environment and potentially the interaction between leaflets have an effect on the structural properties of a bilayer.

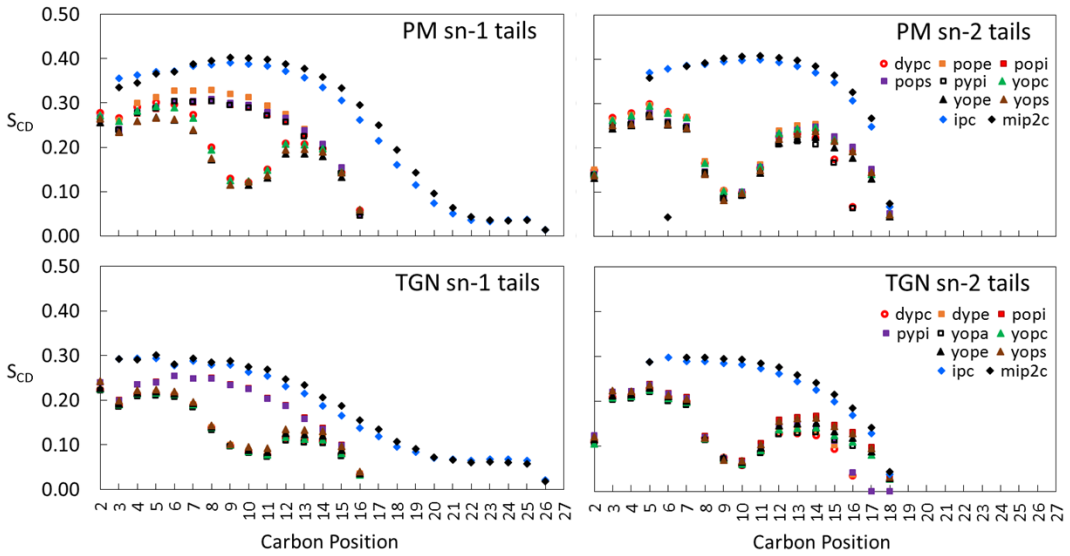

Figure 28 – Order parameters for the lipids in the new PM and TGN models

Table 11 – Comparison between weighted S_{CD} averages of membrane models

Model	system	sn-1	sn-2	system	sn-1	sn-2
Symm.	PM-cyto	0.157	0.122	TGN-cyto	0.148	0.115
	PM-noncyto	0.119	0.163	TGN-noncyto	0.116	0.117
	avg	0.138	0.142	avg	0.132	0.116
Asymm.	PM-cyto	0.171	0.134	TGN-cyto	0.142	0.110
	PM-noncyto	0.111	0.157	TGN-noncyto	0.121	0.122
	avg	0.156	0.150	avg	0.139	0.127

5.1.3 EDPs

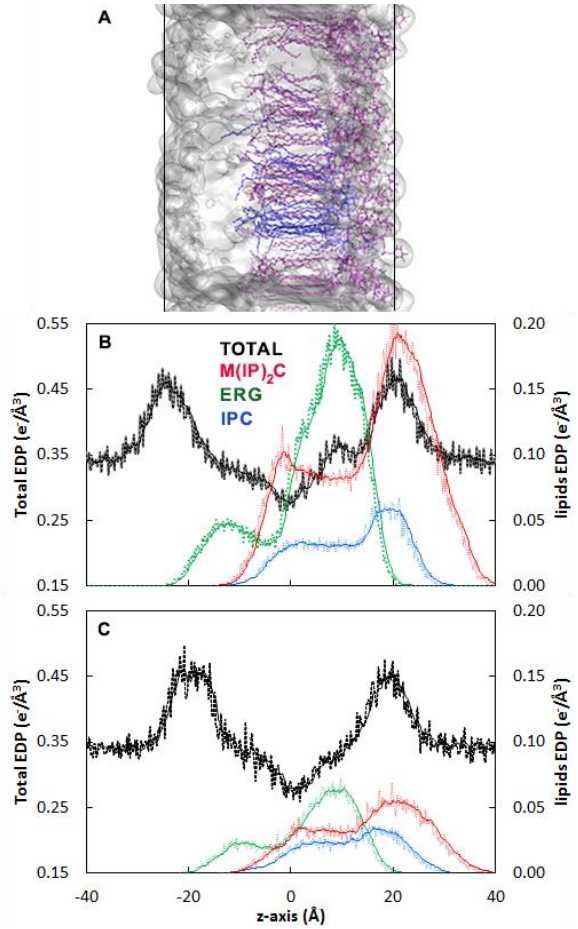

Figure 29 – Total EDPs for the asymmetric models (A) PM model aligned with its corresponding density profile; $M(IP)_2C$ shown in purple and IPC in blue with some of their tails extending into the opposing leaflet and others bended at the center of the bilayer (Solid likes indicate the location of the main peaks in the EDP for this model). Profiles for the (B) PM and (C) TGN models. (Solid lines in the profiles show its moving average)

The EDPs for each system were computed over the last 2μs of trajectory. The location of the SM lipids and ERG in each model is shown in the EDPs for the both systems, PM and TGN (**Figure 29**). The colored profiles, green for ERG, red for $M(IP)_2C$, and blue for IPC also show the relative amounts of these lipids in each model. Notice that both of the SM lipids have a tail that goes into the hydrophobic region of the opposing leaflet, but most of the long SM tails remain in between the bilayers (**Figure 29.A&B**), similar to what was observed for the symmetric IPC models (refer to Figure 22). This is not an artificial or biased result from the way the leaflets were merged when building the systems. The symmetric templates for the non-cytosolic

leaflet had long, extended, tails from the SM embedded in the opposite leaflet. When merging the templates for the cytosolic and non-cytosolic leaflet, a space of at least 8 Å was left between the leaflets to prevent clashing of lipid tails. As the leaflets merged together in an initial equilibration some 26-carbon tails did penetrate into the opposite leaflet, but most remained bended at the center of the bilayer. The same trend of bended SM tails was observed in the IPC ternary systems, which started from a random distribution with some long-tailed lipids extending into the other leaflet.

The peak-to-peak distance for the PM and TGN is 44.4±0.4 Å and 40.8±0.6 Å, respectively. Again, higher sterol content and higher bilayer order in the PM result in a bulkier/thicker bilayer versus the TGN. A notorious difference between the total EDP for the PM is an extra peak in the profile corresponding to the non-cytosolic leaflet (right) due to the large amount of ERG in this model (notice the extra peak aligns with the ERG profile in this model, green curve). This is barely observed around 7 Å in the TGN EDP simply because this model has less sterol. The peak for the M(IP)2C at the center of the PM profile also arises from a higher concentration of this lipid than in the TGN model. The peak shows that significant amount of the long tails in this lipid are bended in between the leaflets, also observed when examining the systems on VMD. However, more analysis needs to be done to quantify the lipid tails that do extend into the other leaflet, and whether this penetration is stabilized by specific lipid-lipid interactions. Most of the interleaflet interaction seems to be related to ERG flip-flop.

5.2.2 Clusters

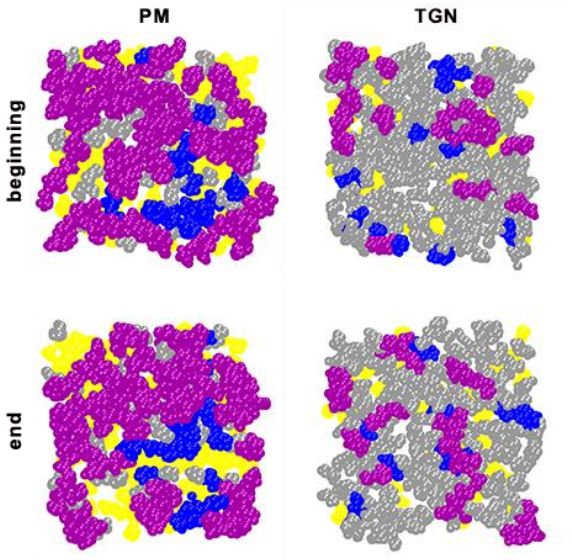

Figure 30 – Snapshots of lipid domains in the asymmetric models ERG (yellow), IPC (blue), and $M(IP)_2C$ (magenta)

Visual examination of lipid clusters in the PM and TGN shows clustering depends, in part, by the amount of lipids in the model. However, even at low concentrations as in the TGN models, SM lipids do aggregate as shown in **Figure 30**. IPC and $M(IP)_2C$ have the same unsaturation degree inside the hydrophobic core. It has been suggested that SM-ERG domains are stabilized by interactions between the amine group in the SM and the hydroxyl group in sterols [165]. There are fewer ERG clusters in the non-cytosolic leaflet of the TGN, and most domains seem to be formed from the interaction of IPC and $M(IP)_2C$ lipids (see **Figure 30**, right panels). Sample lipid-lipid interactions are shown in **Figure 31** for

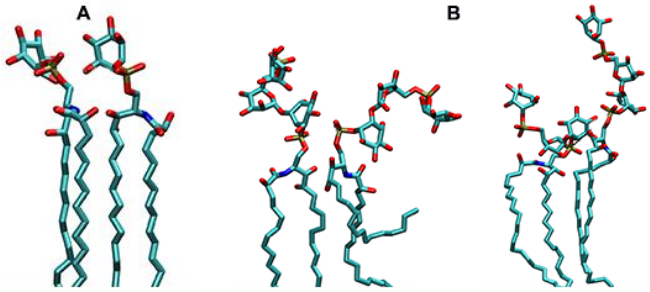

Figure 31 – Lipid-lipid interactions in the asymmetric models between (A) IPC lipids in the PM, and (B) $M(IP)_2C$ lipids in the TGN models.

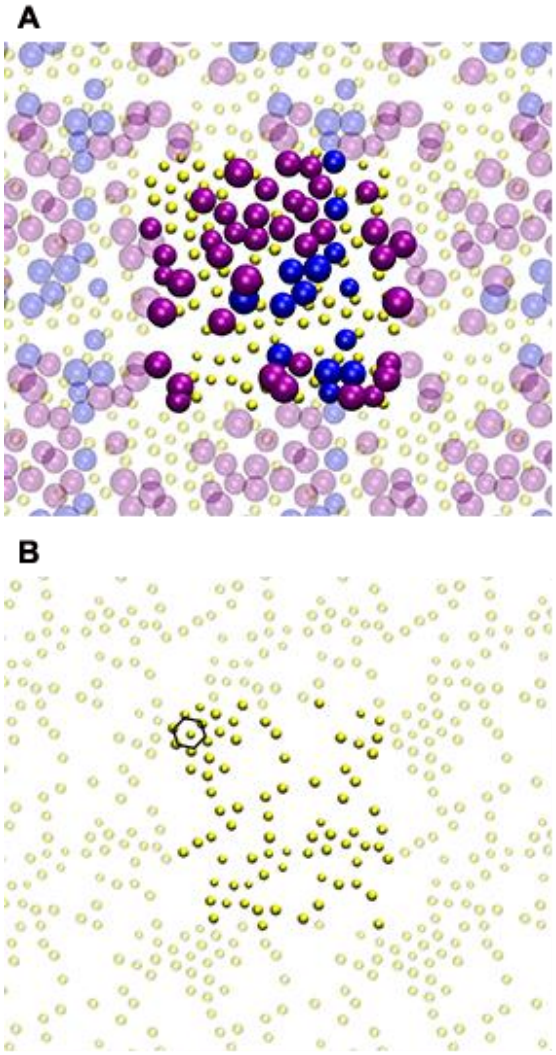

Figure 32 – Lipid clusters in the PM asymmetric model
(A) SM lipids are shown in purple ($M(IP)_2C$) and blue (IPC) and sterols in yellow. (B) Sterol cluster shapes. The spheres represent the center of mass of each molecule and the sizes are relative to the size of each lipid. The main simulation box is shown at the center and faded regions represent the mirror images.

the PM (panel A) and the TGN (B). IPC molecules tend to align to each other better because their headgroups as not as bulky as the $M(IP)_2C$ lipids. Interaction between $M(IP)_2C$ lipids depends on the orientation of the bulky headgroup; it can be extended towards the water as on the left snapshot in **Figure 31.B**, or bended on itself with its sugar closer to the hydrophobic core as one of the molecules in the interacting pair on the right snapshot. Additional analysis will examine the 2D RDFs between the center of mass of the inositol rings to determine if there is a preferred alignment when clusters are formed.

Figure 32 shows qualitatively ERG clusters and their location with respect to IPC (blue) and $M(IP)_2C$ (purple) lipids in panel A. Panel B shows only sterol molecules

represented by their centers of mass and potential cluster shapes. Both, the hexagonal and pentagonal possible configurations for ERG cluster include a sterol molecule at the center. There are some sterol molecules arrange in a linear fashion, which need to be further examine to determine if there is a particular orientation in terms of the β-face of the sterol, like back-to-back or front-to-back spatial arrangement. 2D RDFs analysis will further examine inter-species interactions to determine lateral organization of ERG, IPC, and $M(IP)_2C$ as it pertains to cluster formation. Interactions to be examined include P-P, for both phosphates in the case of $M(IP)_2C$ lipids, and N-O for SM-sterol pairs (amine-hydroxyl groups).

Chapter 6: Membrane-Protein Simulation Results

6.1 ALPS-like Motif of Osh4

6.1.1 Binding events

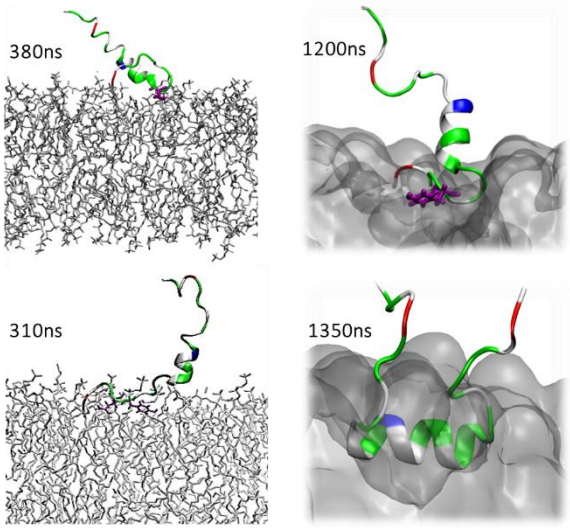

Figure 33 – Binding conformations of the ALPS-like motif of Osh4
(top) vertical conformation for the o-npt system, (bottom) horizontal conformation from the z-nvt system. Non-polar residues are shown in white, polar residues in green, negatively charged residues in red, and positively charged residues in blue.

Two binding conformations were observed for the ALPS-like motif studies; one with the peptide oriented perpendicular to the membrane surface, or slightly tilted, and partially embedded and the other with the peptide lying horizontally on the bilayer embedded at the phosphate region of the interacting leaflet (see **Figure 33**). Binding events were stochastic and no preference was shown for a given bound conformation based on the original orientation of the peptide above bilayer (see **Table 3**). Binding events were characterized

qualitatively using VMD to estimate the binding time scale, and quantitatively from the time series and block averages of ΔE^{bind}.

Initial contact time between the peptide and membrane are listed in the last column of **Table 3.** Interactions were listed if they lasted for at least 50ns, even if stable binding wasn't yet obtained. The use of surface tension had no effect on the final bound conformation, it simply accelerated the binding time scale by nearly 50% in the ER and TGN models, and by 38% in some of the simpler models. From the 21 trajectories obtained in this study, two had no stable binding, and four had peptide-membrane interaction events as early as at 300ns that lasted as much as 230-640ns prior to stable binding, which took place at least after 1.54μs of trajectory (see **Table 3**). Peptide contact times smaller than 300ns in **Table 3** lasted between 50 to 100ns, after which the peptide returned to the aqueous phase before binding to the membrane in its final conformation. It remains still unclear whether the peptide bound to the bilayer due to existing packing defects (i.e. enough exposure of the membrane's hydrophobic core), or if it contributed to the creation of packing defects upon binding. Future analysis based on a probabilistic formalism is underway to determine causation.

Table 12 – ΔE^{bind} between the ALPS-like peptide and model membranes

System	Conformation	ΔE^{bind} (kcal/mol)	
		full peptide	main helix
PC-PS	vertical	-295.06 ± 37.22	-52.76 ± 29.15
	horizontal	-334.53 ± 47.71	-68.87 ± 31.83
ER/TGN	vertical	-366.35 ± 47.83	-83.36 ± 24.50
	horizontal	-438.92 ± 29.57	-144.29 ± 24.21

Table 12 summarizes the block averages for the peptide-membrane interaction energies with simple (PC-PS) and complex (ER/TGN) model membranes. As anticipated, the horizontally bound conformation is enthalpically more stable as it results in the non-polar side changes of the peptide's main helix pointing towards and interacting with the membrane hydrophobic core. The contribution to the interaction energy from the main helix, listed on **Table 12** is only a small fraction of the total interaction energy between the full peptide and the membrane (20.6% and 32.9% in the horizontally bound conformation for the PC-PS and yeast systems respectively). This is because the entire helix was considered in the interaction energy analysis instead of simply the interacting residues. In addition, in both horizontally and vertically bound conformations, the N-terminus was interacting or embedded into the hydrophobic core. Since there are charged residues in this end of the peptide, there may also be electrostatic energy contributions from this terminus that account for a larger fraction of the interaction energy that were not anticipated before. A close examination to the interacting energy per residue is needed to determine quantitatively those that contribute more to peptide binding.

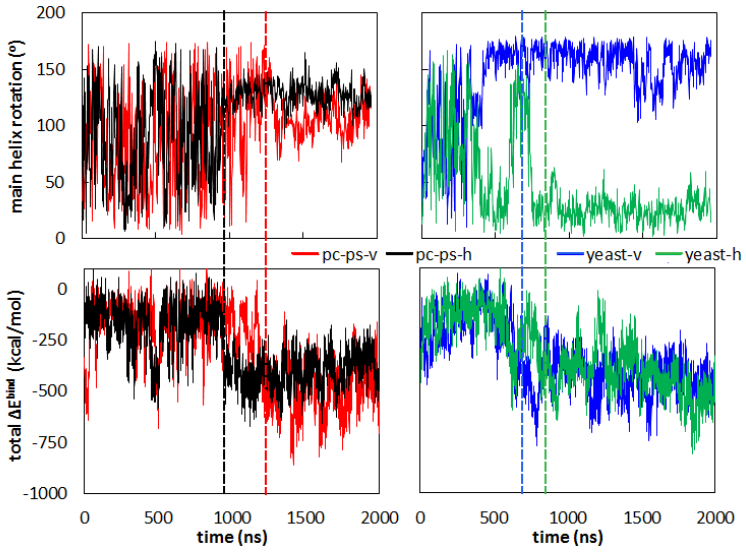

Figure 34 – Helix rotation on itself (top) and the corresponding ΔE^{bind} (bot) The dashed lines show the binding time for representative systems: z-nvt (pc-ps-h), o-npt (pc-ps-v), 20er-1 (yeast-h), 20er (yeast-v)

Figure 34 (top) shows the time series of the vector defined from the polar face of the main helix to its non-polar face to quantify the rotation angle of the main helix on itself throughout the simulation. The data in the first 1000ns is mainly noise, since the peptide rotates freely when in water. Upon binding, shown by the cashed lines in the figure, especially in the horizontally bound conformation, the non-polar residues of the main helix prefer to interact with the hydrophobic core facing downwards (lower binging energy). The rotational angle of the main helix describes its reorientation as the non-polar face rotates to be in direct interaction with the hydrophobic core. This rotational angle is not a measure of peptide tilt with respect to the membrane, which is discussed later; it simply indicates how the peptide rotates on itself if it initially interacted with the bilayer from a different orientation (non-polar face facing the water or sideways).

An angle of 180º indicates the non-polar face of the peptide is oriented downwards with respect to the z-axis, since the angle is measured with respect to the bilayer normal of the top leaflet. Since the simulations use PBC and the peptide is free to move in the solvent (water), it can bind to either leaflet of the bilayer. When it binds to the top leaflet, an angle closer to 180º indicates its non-polar face is pointed towards the hydrophobic core. However, when the peptide binds to the bottom leaflet, and angle of 180º indicates its non-polar phase is looking towards the water. In **Figure 34**, the top panels show angles larger than 100º for the *pc-ps-h*, *pc-ps-v*, and *yeast-v* systems. In **Figure 35**, these systems show the final peptide orientation is with its non-polar residues facing downwards with respect to the positive z-axis. Therefore, the large angle indicates the non-polar residues face the hydrophobic core of the membrane in the case of *pc-ps-h* (**Figure 35.A**), face downwards but not directly to the hydrophobic core for *pc-ps-v* (**Figure 35.B**), and face towards the water in the *yeast-v* system (**Figure 35.D**). For *yeast-h*, **Figure 34**

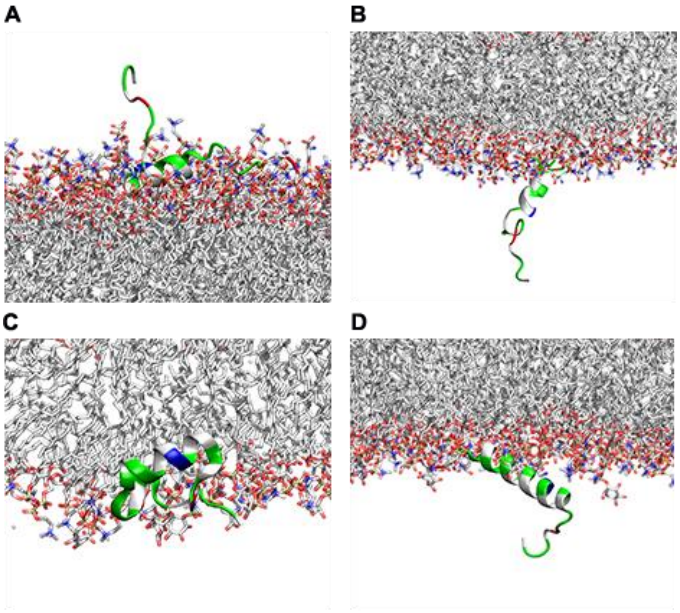

Figure 35 – Final orientation of the peptide in sample systems (A) The pc-ps-h system (z-nvt) bound to the top leaflet of the bilayer; all the others to the bottom leaflet, (B) pc-ps-v (o-nvt), (C) yeast-h (20er-1), and (D) yeast-v (20er)

indicates an angle closer to 45º; note in this trajectory the peptide bound horizontally to the bottom leaflet with its non-polar residues facing towards the bilayer core in agreement with the angle measured.

Notice in the top images in **Figure 33**, TYR4 is a stabilizing residue of the vertical bound conformation as its ring lays flat near the phosphate region of the lipids. LYS15 and SER18 also contribute to the stability of this conformation interacting with the lipid headgroup atoms. Although the vertical conformation was stable for nearly the last 1μs of the simulation, the horizontal conformation shows a more interesting binding mechanism that aligns better to what has been seen in other amphipathic helices [69, 99]. The horizontal conformation was stabilized by the interaction of LYS15, THR11, and SER6 with the bilayer as determined from H-bonding analysis. **Table 13** lists other residues that also interacted significantly with the bilayer as determined from hydrogen bonding analysis on VMD setting the criteria for hydrogen bonding to an angle of 30º and a bond length of 3.2 Å. In all cases, SER8 was a recurring interacting residue and usually the first one to approach the bilayer prior to stable peptide attachment. From visual examination of the systems using VMD, PHE13, THR11, and TRP10 are bulky residues that also stabilize peptide binding. To complete these analysis, interaction energies of individual residues are being computed and will be classified according to bound conformation.

Table 13 –H-bonding analysis upon stable peptide binding

System	Conformation	Interacting residues	% H-bonding (upon stable binding)
PC-PS	vertical	Ser6	6.01
		Ser2	5.51
		Gln3	5.11
		Ala5	4.10
	horizontal	Ser7	8.71
		Thr11	7.06
		Tyr4	6.51
		Ser6	5.51
		Ser8	4.86
		Ser9	4.53
ER/TGN	vertical	Ser2	11.63
		Ser7	10.79
		Asp0	10.20
		Lys15	10.13
		Ser8	9.25
	horizontal	Lys15	14.08
		Ser16	10.15
		Asn21	9.76
		Ser19	7.95
		Ser12	6.38

No direct horizontal binding (solution to horizontal binding state) was observed in the systems with the ER and TGN models due to, apparently, lack of large enough packing defects on the membrane surface. Nearly all of the trajectories with the yeast membrane models had the peptide initially bound the membrane in a vertical conformation that further stabilized into the horizontal configuration for five out of the nine systems. However, two out of the six trajectories run for these systems showed that when a hydrophobic side chain approaches a bilayer packing defect in a particular orientation such that its bulky non-polar residues can interact directly with the hydrophobic core, it embeds itself on the small defect creating a larger one as it assumes

the horizontal bound conformation. This binding mechanism includes first unfolding of the main helix upon approaching the membrane, interaction of the hydrophobic residue with the hydrophobic core, and refolding of the main helix pushing away lipid headgroups around it to effectively create a larger packing defect where it sits horizontally until the end of the simulation.

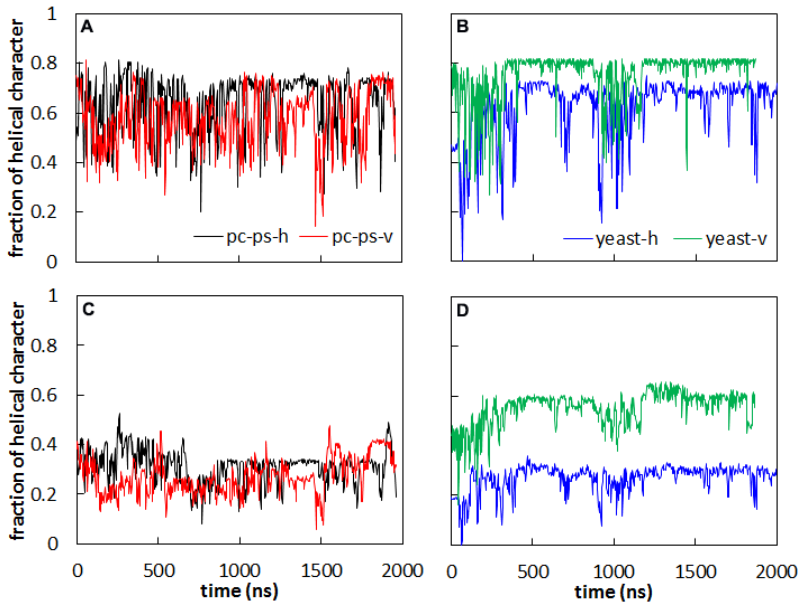

Figure 36 – Helical character of the peptide throughout the simulation
For representative systems of with horizontal (H) and vertical (V) bound conformations at equilibrium (z-nvt for pc-ps-h; o-npt for pc-ps-v; 20er1 for yeast-h; and 20er for yeast-v).
(A) and (B) show the helical character of the main helix in the PC-PS and complex systems respectively; (C) and (D) are the time series or the helical character of the entire peptide in the same systems.

Loss of helical character happens at some point during the all the trajectories, an obvious example is shown in **Figure 36** for the sample systems. Unfolding and refolding of the main helix takes approximately between 300 and 450ns depending on the system, and can be appreciate it examining the time series of the peptide's helical character (**Figure 36.B**). The sample system for the vertically bound conformation in the yeast systems (*20er*) is an

interesting case since the peptide increased its overall helical character once it had stably bound to the bilayer (see also **Figure 35.D**). The peptide lies at an angle at the end of the simulation, with its non-polar face oriented towards the solvent and more residues adopt an alpha-helix secondary structure.

The tilt angle of the main helix with respect to the bilayer surface, as shown in **Figure 14**, was blocked averaged after peptide binging to quantify the bound conformation for each system. **Table 14** lists the average values calculated among the systems sharing a given bound conformation (refer to **Table 3**). As expected, the tilt angle is smaller for the horizontally bound systems.

Table 14 – Tilt angle of the main helix upon stable binding

Bound conformation	Angle with the bilayer surface
pc-ps-h	20.16 ± 1.51
pc-ps-v	37.99 ± 1.28
yeast-h	23.87 ± 1.00
yeast-v	39.41 ± 0.99

6.1.2 Protein-lipid interactions

EDPs were computed for all systems, **Figure 37** and **Figure 38** show examples of the vertically and horizontally bound conformations for both the PC-PS and the ER/TGN models. The peptide is more embedded into the leaflet of the yeast membranes when bound horizontally, shown in the side view of **panels A** and **B** of both figures. The frequency of contact (FOC) plots shown on **Figure 39** also describe

the interaction between the peptide (C_α atoms) and leaflet to which it bound. The peptide seems to be more comfortable when it is at the phosphate region (panel A) of

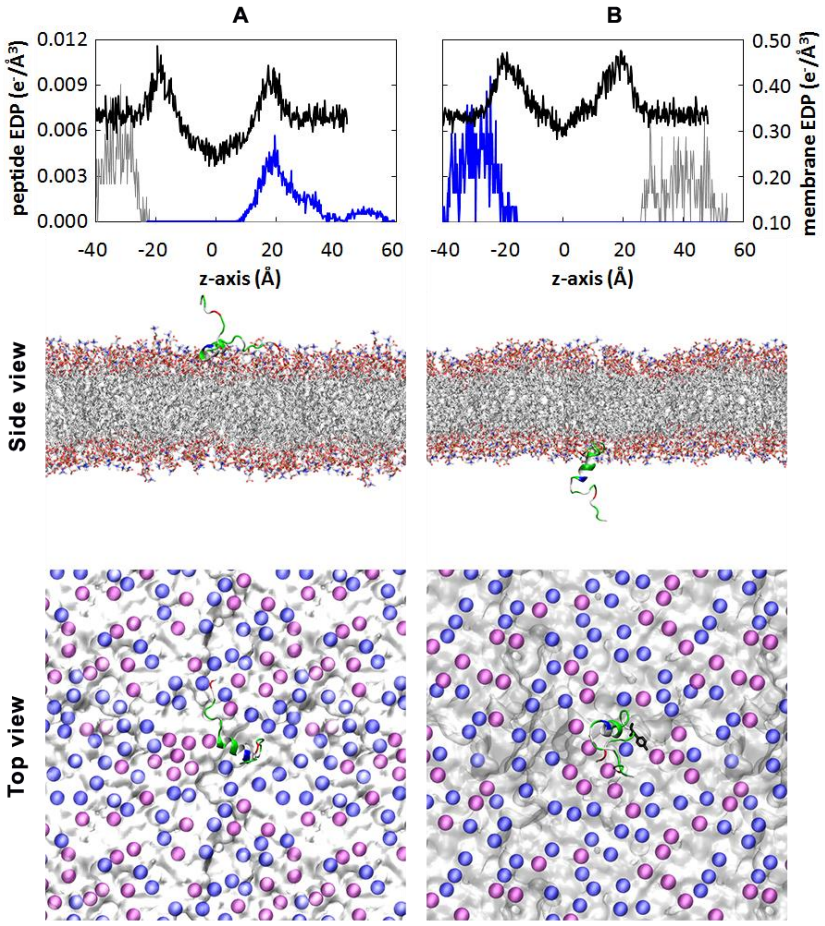

Figure 37 – EDPs of the peptide at its initial and final positions (PC-PS systems) Total membrane (black), bound peptide (blue), and initial peptide location (gray) for the (A) horizontally and (B) vertically bound conformations in the o-npt and z-nvt systems. The top view shows the hydrophobic core in white and the phosphorus atoms of DOPC (blue) and DOPS (purple) of the interacting leaflet (membrane images included)

the bilayer instead of further out around the glycerol region of the lipids (panel B). It is interesting to see that for all bound conformations the N-terminus (residues 1 to 7) is, on average, always interacting or embedded into the bilayer, which was also observed

when examining the systems visually on VMD. However, the C-terminus is in more contact with the complex bilayer models, suggesting the peptide is more deeply

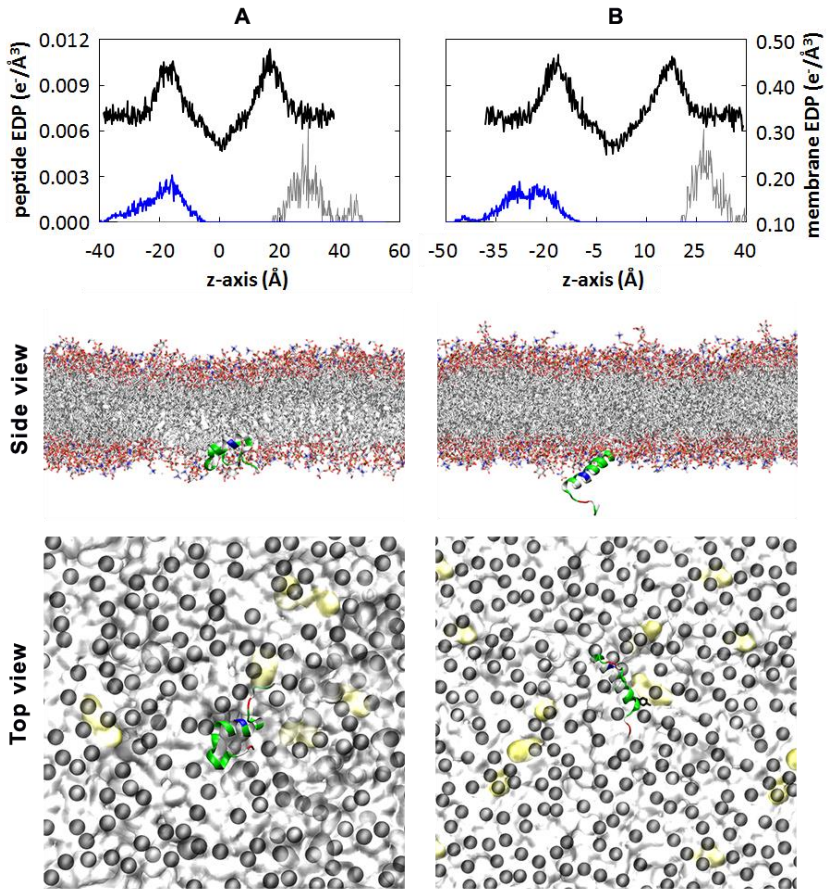

Figure 38 - EDPs of the peptide at its initial and final positions (complex systems) Total membrane (black), bound peptide (blue), and initial peptide location (gray) for the (A) horizontally and (B) vertically bound conformations in the 20er1 and 20er systems. The top view shows the hydrophobic core in white and the phosphorus atoms of the interacting leaflet in black (membrane images included). ERG molecules are shown in yellow

embedded in these models than in the simpler PC-PS ones. Panel C in this figure shows FOC between the heavy atoms in the peptide (all atoms that conform a particular residue) and the membrane for the sample systems that have been discussed throughout

this chapter. The data reported on **Figure 39.A&B** was averaged among all systems sharing a given bound conformation (*pc-ps-h*, *pc-ps-v*, *yeast-h*, and *yeast-v*).

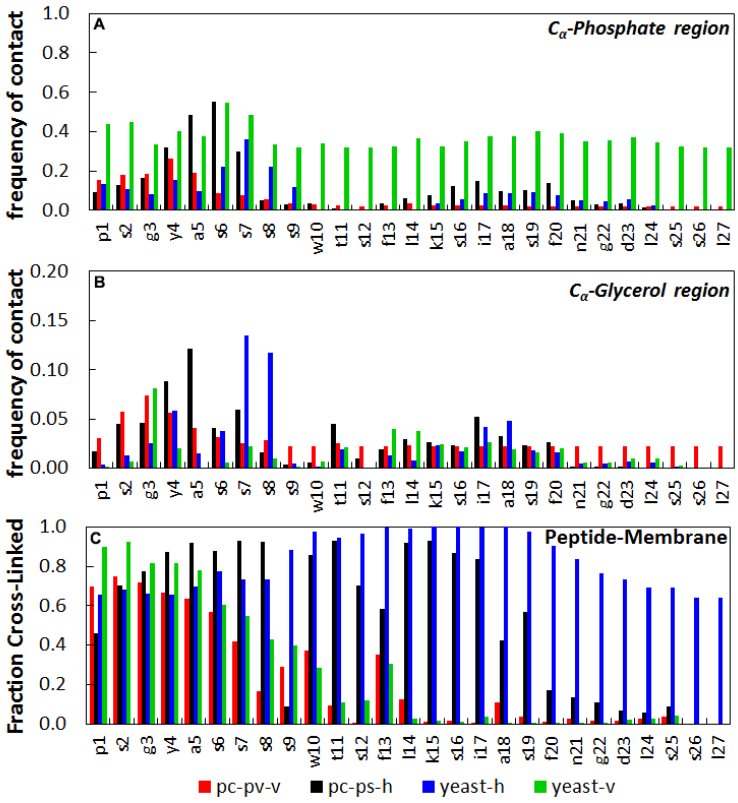

Figure 39 – Frequency of contact (FOC) between peptide and membrane Interactions were evaluated between the C_α in all residues in the peptide and (A) the phosphorus atoms in the interacting leaflet, and (B) the second carbon in the lipid glycerol at 3Å around the peptide C_α atoms. (These results were averaged among all the systems sharing that bound conformation). (C) FOC between the heavy atoms in the peptide (no hydrogens) and the membrane (cut-off 5Å)

6.2 Full Osh4 protein simulations

6.2.1 Binding events

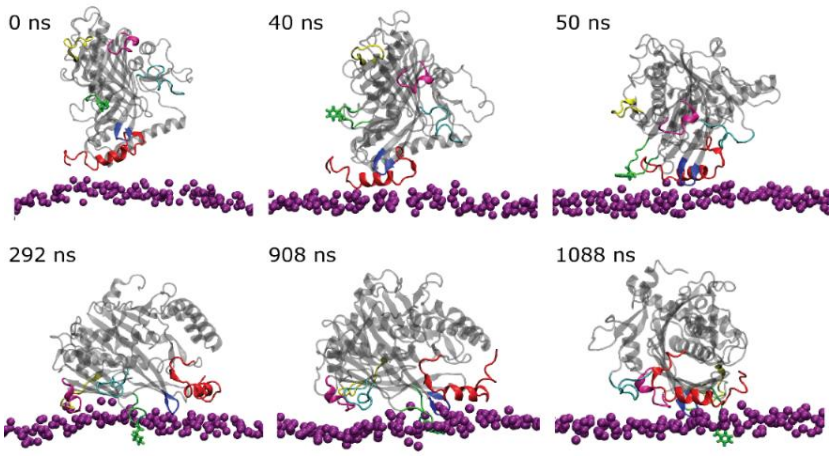

Figure 40 – Osh4 binding sequence for a simulation with the TGN model The binding sites are colored as described in **Figure 5**; the PHE239 residue, shown in detail, remains in the hydrophobic core upon stable binding (~200 ns) well below the phosphorus atoms (purple).

Simulations of the entire protein with the symmetric ER and TGN models show the phenylalanine loop (PHE-loop) is one of the most important binding regions of Osh4 in the interaction with anionic membranes, followed by the ALPS-like motif and the β6-β7 loop. These last two regions are the first to interact with the bilayer as early as 45ns into the simulation; after which the PHE-loop pulls the protein sideways towards the membrane surface. Within the first 200ns of simulation, the protein rotates from a vertical position (mouth facing the membrane surface) to lay horizontally on the surface with F239 in the PHE-loop fully embedded in the hydrophobic core (see **Figure 40**). Initial interaction with the membrane and stable binding, marked by the full penetration of residue F239 into the hydrophobic core, were both reached faster in the TGN membrane models (see **Table 15**) due to

their higher anionic lipid content. In all runs, F239 in the PHE-loop, one of the six binding regions observed by Rogaski and Klauda in a previous study [97], served as an anchor stabilizing protein-membrane interaction. In addition, S240, K242, and R249 were among the most common residues consistently interacting with the bilayer through hydrogen bonds or transient penetration into the hydrophobic core. Based on the hydrogen bond analysis done in VMD [147], most of the interaction with the bilayer was at the location of anionic lipids, PS and PI, as in previous studies [97]; but there was some interaction with PC and PE lipids as well.

Table 15 - Full protein interaction with model membranes (binding events time scale)

	oer	oer-1	otgn	otgn-1
size (atoms)	121,240	121,240	138,560	138,560
sim time (ns)	2,040	2,040	2,066	2,040
1st contact (ns)	46	80	11	12
F-loop binding (ns)	80	46	63	90
stable binding (ns)	480	212	214	204

ΔE^{bind} between the full protein and the membrane as well as between the binding regions of the protein and the membrane are reported on **Table 16**. These values show ΔE^{bind} is stronger for the TGN systems by 50% since these have more anionic character. The largest contribution comes from the PHE-loop, with -847.51 ± 0.35 and -420.18 ± 12.96 kcal/mol for the TGN and ER systems, respectively. Note the ΔE^{bind} contribution for the TGN is nearly twice as much as that for the ER, a similar trend was observed for the β14-β15 loop but to a lesser extent. These results differ from those reported by Rogaski and Klauda [97], who reported the β14-β15 loop as the largest contributor to

the ΔE^{bind} for simulations with neutral and less charged membranes compared to those presented here.

Table 16 – Interaction energies between Osh4 and membrane models
The standard errors are based on 10-ns block averages after stable binding of the full protein as well as the protein binding regions. The total interaction energy includes long-range electrostatic interactions, which contribute to most to the total value reported in this table.

	ΔEbind (kcal/mol)	
	ER	TGN
Total	-4166.98 ± 17.26	-6185.35 ± 48.21
ALPS-like	-230.94 ± 6.43	-288.29 ± 16.99
PHE-loop	-420.18 ± 12.96	-847.51 ± 0.35
β6-β7	-240.30 ± 3.87	-375.06 ± 12.37
β14-β15	-143.51 ± 0.04	-244.13 ± 7.10
β16-β17	-221.58 ± 10.77	-296.56 ± 50.10
β-crease	-223.96 ± 2.25	-224.85 ± 2.34

Figure 41 shows two of the most interesting ΔE^{bind} time series out of the six binding regions, the PHE-loop and the ALPS-like motif. They both show the protein has a stronger interaction with the TGN membranes over the ER, but the PHE-loop contributes nearly twice as much to the ΔE^{bind} than the ALPS-like motif. From these observations, it is clear lipid composition does play a critical role in protein-membrane interactions and can influence the attraction of proteins to the membrane surface.

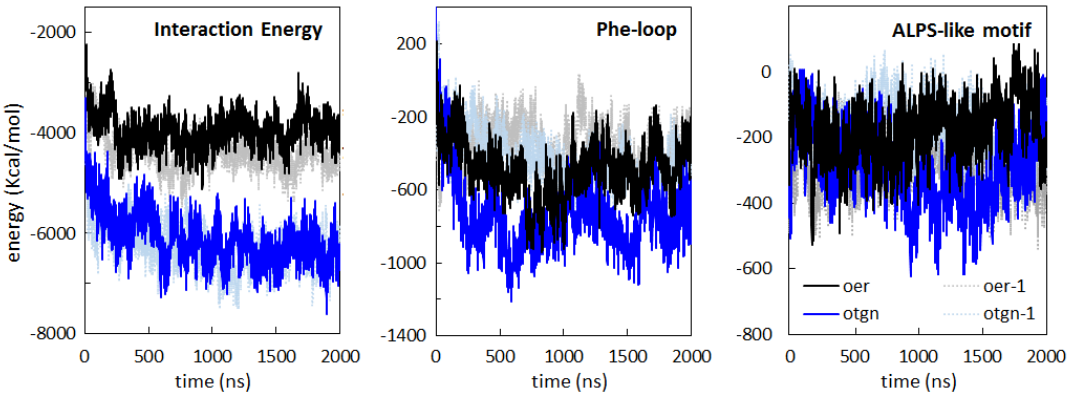

Figure 41 – Interaction energies between Osh4 and the ER and TGN
The time series for the PHE-loop and the ALPS-like motif and each model are also shown

Figure 41 – Interaction energies between Osh4 and the ER and TGN
The time series for the PHE-loop and the ALPS-like motif and each model are also shown

6.2.2 Protein-lipid interactions

In general, F239 remained well below the phosphate region of lipids during the entire trajectory after its initial penetration, but transiently moved upwards during protein rotation. The last two time snapshots in **Figure 41** show F239 exits the hydrophobic core when the ALPS-like motif interacts with the bilayer more closely; at the same time, the β14-β15 and β-crease loops pull away from the membrane as the protein rotates. Once rotation takes places, F239 embeds deep into the hydrophobic

core again and remains there until the end of the simulation. Protein rotation was stochastic and only took place in one of the two replicas for each system. Rotation (defined by movement around the axis perpendicular to the membrane normal) was greater on the ER membrane (~180º) vs. the TGN model (~90º) possibly because the ER model is more fluid than the TGN; the rotation time scales were 500 and 250 ns for the protein-ER and protein-TGN systems respectively.

As a final analysis on these system, the frequency of contact between the protein and membrane was computed for certain residues to compare with cysteine-replacement cross-linking studies performed by Schulz *et al* [95]. The non-hydrogen protein-membrane contacts within 10 Å of each other were counted after stable binding for all the residues studied in the experiment publication (**Figure 42**), which were also examined for all systems in a previous computational study [97]. The contact distance was selected to mimic the distance required for experimental cross-linking between a cysteine in the protein and a liposome. Seven of the nine cysteine-replaced interacting residues identified in the experimental study were found within 10 Å of the ER and TGN membranes: S8, A169, S174, G241, E261, E284, and E412. Three of the seven residues, S174 from the β6-β7 loop, G241 from the PHE-loop, and E261 from the β14-β15 loop were in close contact with the membrane surface at all times upon stable binding. Residues S8, from the ALPS-like motif, and A169 were close to the surface at least 60% and 28% of the time respectively. E412 was a residue that showed distinct preference for the TGN membranes, where it was in close contact to the surface 84% of the time vs 48% of the time at the ER membranes

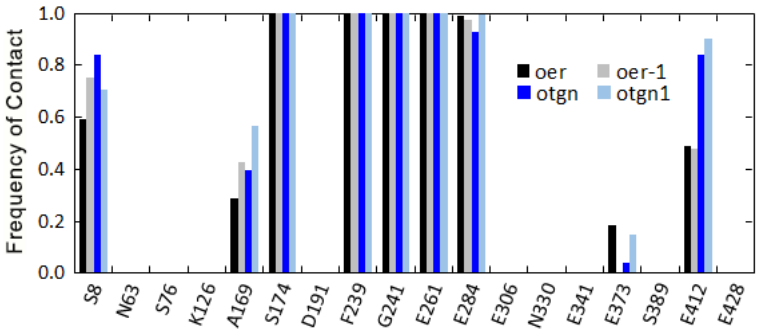

Figure 42 – Frequency of close contact between selected Osh4 and membrane lipids.
Selected residues correspond to those studied by Schulz et al [95] (experiment) and Rogaski & Klauda [97] (computation).

surface. These simulations show lipid composition does influence protein-membrane interactions; thus, accurate membrane models are desirable when studying protein function and binding mechanisms.

Residues that were not significantly cross-linked with liposomes experimentally (N63C, S76C, K126C, H144C, E306C, E341C, E373C, S389C, E248C) were also found to have no close contact with the membrane surface in this study as sown in **Figure 42**. Except residue E373 that was in contact with the membrane surface between 5% and 18% of the time indistinct of the membrane model. In addition, residues E306 and N330 were not found within 10 Å of the membrane surface with the ER or TGN models, but found to interact experimentally.

Chapter 7: Water-Oil Interface Simulation Results

7.1 Interfacial Tension

7.1.1 Hydrotrope effect at the interface

Figure 43 shows the interfacial tension for systems at varying concentration of the hydrotrope (**Table 17** lists the values with their standard errors). The bottom panel in this Figure shows from experimental data [168-170] of other water-organic-hydrotrope systems and serves as a qualitative comparison to show the simulation data follows the expected trend. The experimental data points show that for very small alcohols such as methanol

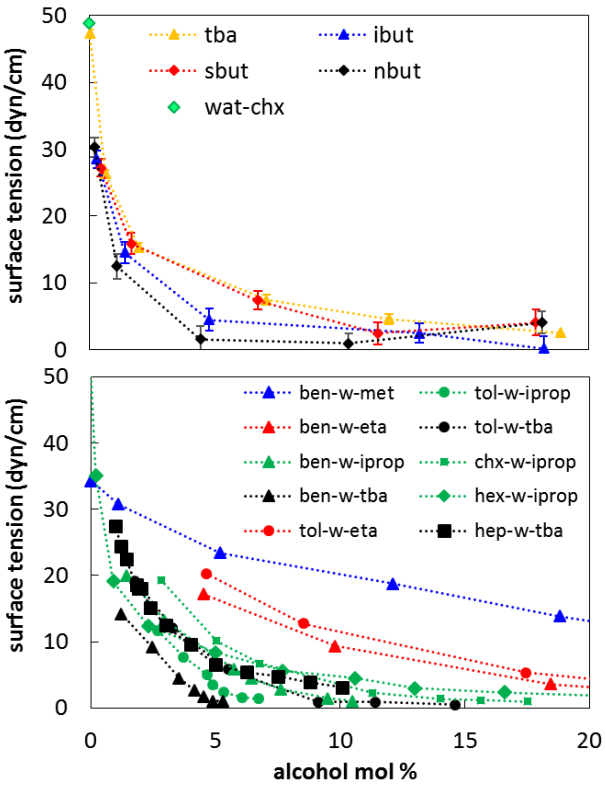

Figure 43 – Disruption of the interfacial tension at the water-oil interface
(only simulation data are presented in the top graph, comparison with TBA experimental systems is discussed in section 7.3) The bottom plot summarizes experimental data from [167],[168], and [169]

and ethanol, the effect on interfacial tension between water and an organic solvent is not that large. However, for *i*-propanol and TBA, green and black sets, the effect is readily seen at as little as 0.11% molar hydrotrope concentration in the aqueous phase.

Table 17 – Average interfacial tension of the butanol isomers systems
The system name was kept consistent with the names of the TBA systems used for comparison with experimental data to avoid confusion. The names of the other butanol isomers use the same system number as the TBA runs with the same overall concentration of each species as listed on **Table 4**

	System	mol % in water	Interfacial tension (dyn/cm)
Wat-chx	T0	-	48.92 ± 0.03
TBA	T5	0.67 ± 0.02	26.39 ± 0.49
	T7	2.64 ± 0.21	15.31 ± 0.56
	T11	7.23 ± 0.22	7.41 ± 0.63
	T12	12.09 ± 0.09	4.58 ± 0.76
	T13	18.59 ± 0.08	2.52 ± 0.78
IBUT	I5	0.39 ± 0.09	28.54 ± 1.31
	I7	1.55 ± 0.19	14.53 ± 1.60
	I11	5.82 ± 0.53	4.43 ± 1.66
	I12	12.22 ± 0.65	2.44 ± 1.44
	I13	18.50 ± 0.06	0.18 ± 1.83
SBUT	S5	0.46 ± 0.01	27.22 ± 1.34
	S7	1.73 ± 0.03	15.89 ± 1.64
	S11	6.39 ± 0.18	7.36 ± 1.39
	S12	11.87 ± 0.22	2.45 ± 1.67
	S13	18.66 ± 0.39	4.08 ± 1.97
NBUT	N5	0.19 ± 0.01	30.29 ± 1.42
	N7	1.07 ± 0.05	12.48 ± 1.87
	N11	4.46 ± 0.45	1.54 ± 1.97
	N12	11.03 ± 0.32	0.96 ± 1.40
	N13	18.26 ± 0.22	4.08 ± 1.68

7.1.2 Hydrotrope orientation at the interface

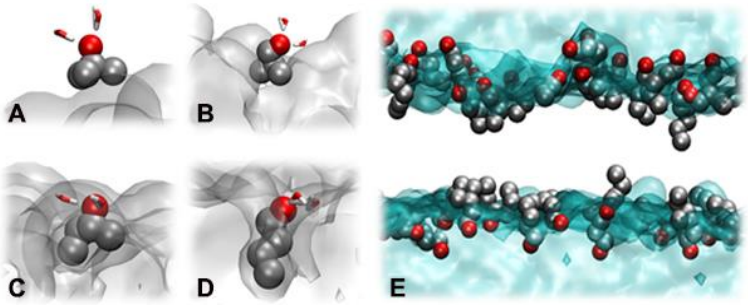

Figure 44 - Spatial orientation of butanol isomers at the interface Two water molecules are shown as reference of hydrogen bonds with (A) TBA, (B) IBUT, (C) SBUT, and (D) NBUT; cyclohexane is shown in gray. (E) NBUT partition at the interface, only its hydroxyl groups are in contact with water, CHX was omitted for clarity.

Figure 44 shows the spatial orientation of each isomer at the interface. At low alcohol concentrations most of the isomer molecules migrate to the water-oil interface to reduce the interfacial tension; however, alcohol concentration increases in the aqueous phase when the concentration at the interface is saturated. For alcohol concentrations greater than 10% molar in water, there are CHX clusters transiently detaching from the bulk oil phase surrounded by alcohol molecules, but these were not stable and returned to the oil phase within 3-5 ns. In general, short hydrotropes orient themselves so that their hydroxyl group forms hydrogen bonds with the aqueous phase while the carbon atoms interact with the oily phase (see **Figure 44**.e). The difference in chemical structure of short hydrotrope isomers like those of butanol may seem irrelevant at first glance. However, even at low alcohol concentrations, their effect is noticeable. Two extremes are the bulkier molecule (TBA, **Figure 44**.a) that does not penetrate into the oily phase, and the elongated isomer that partitions more into the CHX phase and interacts with water

only through its hydroxyl group (NBUT, **Figure 44**.d). Of course this difference arises from the structure of the molecules and the freedom or limitation each has to rotate and stretch.

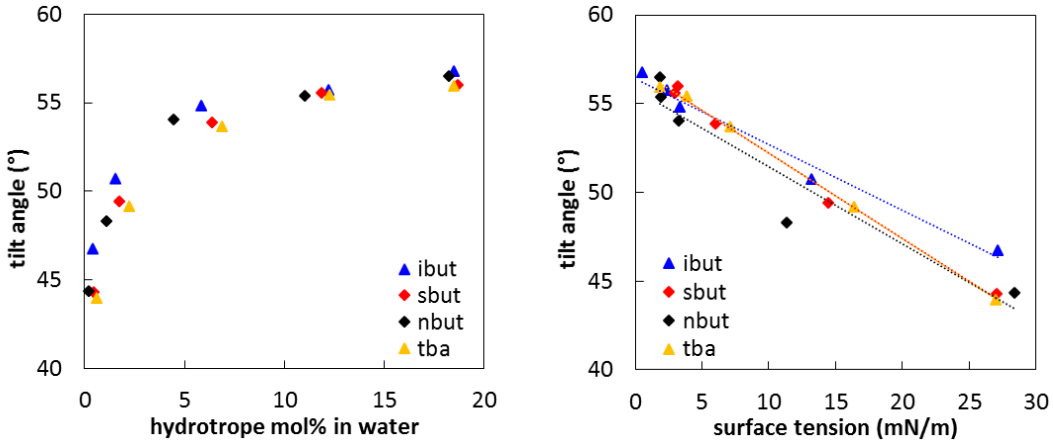

Figure 45 – Tilt angles of the C-OH bond of the isomers at the interface with respect to (left) the hydrotrope concentration in water, and (right) the surface tension

Values are reported for all isomers at the equilibrium concentrations of each alcohol listed in **Table 17** (lowest to highest concentration from left to right). The tilt angle between the C-OH bond for each isomer and the z-axis was also calculated for all the systems (see **Figure 45**). The left figure shows how the hydrotrope orients its hydroxyl group at the interface with respect to its concentration in the aqueous phase. The more alcohol in solution, the more it accumulates at the interface; once the interface saturates, the rest remains in the water phase. The simulation model does not properly represent the alcohol-oil interactions at high alcohol concentration, i.e. no alcohol molecules partition to the oily phase (cyclohexane) once the interface is saturated. However, the tilt angle of the hydroxyl group seems to level off once the interface is saturated in

alcohol, i.e. the lateral organization of the alcohol molecules at the interface is fixed. At low concentrations, the alcohol molecules at the interface have more space to orient themselves with their hydroxyl group pointing straight towards the aqueous phase. The packing of alcohol molecules becomes tighter as the molecules accumulate at the interface, and the hydroxyl groups result in a more tilted orientation. All the isomers follow this behavior as observed in **Figure 45** (left panel). Additionally, the right panel of this figure shows the tilt angle of the interface molecules has a linear dependence with respect to surface tension. **Table C.1** lists the block averages of the tilt angle of every isomer along with their respective standard error.

7.1.3 Lateral organization of the isomers at the interface

Figure 46 shows the 2D RDF between the hydroxyl oxygen (O) of the hydrotrope molecules and between the carbons attached to the hydroxyl group (C_α) for the molecules located at the interface. For this analysis the hydrotrope molecules at the interface were counted at each frame using CHARMM, with a buffer of 12 Å above and below the coordinates of the cyclohexane region in the simulation box. The RDFs for each system are non-zero at very short distances, even more so as the hydrotrope concentration increases. This occurs because 2D RDFs are evaluated at the x-y plane, and because of the way alcohol atoms were selected for this analysis, there are some molecules lying on top of other when observed from the top (**Figure 46.B**).

Figure 46.**A** shows the C_α- C_α interactions, which occur essentially at the same distance for all concentrations of a given isomer. The only variation is the frequency of these interactions; the distributions show a higher peak of the first solvation shell for systems with lower hydrotrope concentration. This is a direct result of the number of molecules taken into account at the interface for this analysis. The O-O distributions, **Figure 46.C**, have two solvation shells at similar distances for all systems, and a third one for more of the low to moderate butanol concentrations. As expected, the O-O 2D RDFs for NBUT present a higher peak for the first solvation shell, which arises from the linear chemical structure of this isomer and the alignment of the hydrotrope molecules at the interface (see also **Figure 44**.**D&E**)

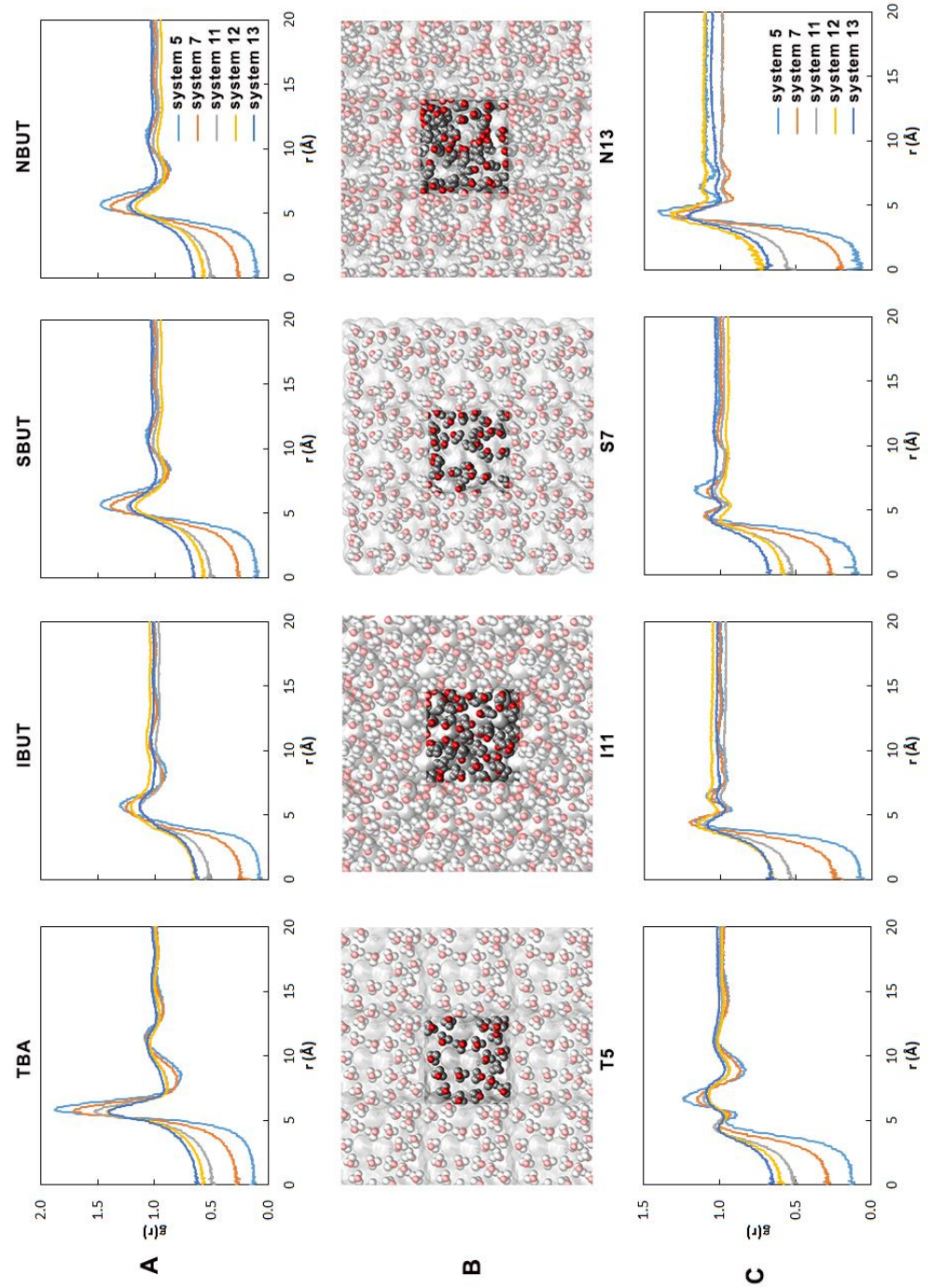

Figure 46 – 2D RDFs between hydrotrope groups at the interface
(A) Butanol C_α- C_α interactions; (B) top-view for selected systems showing the hydrotropes at the interface; (C) Hydroxyl O-O interactions

7.1.4 Atom number density profiles (ADP)

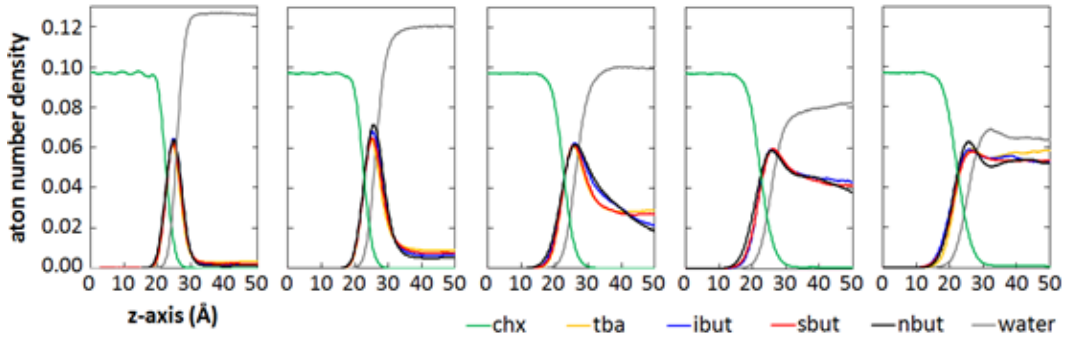

Figure 47 – Symmetrized ADPs for the water-CHX-hydrotrope systems.
The plateau of the isomer's profile was used to estimate its equilibrium concentration in the aqueous phase (values reported in **Table 17**)

A clearer picture of the hydrotrope layer at each interface can be observed on **Figure 47**, on the equilibrium ADPs for each system. The position of the isomers is nearly identical in all the systems, except at the highest concentration, where NBUT (black line) is present in larger concentration at the interface compared to the other three isomers. Despite the subtle difference in amount of hydrotrope at the interface, the chemical structure of each isomer does differ on its effect on the interfacial tension. It is remarkable to note that even at concentrations below 0.11% molar, a hydrotrope drops the interfacial tension to at least 60% of the 48.92 ± 0.03 dyn/cm of a pure water-CHX system. TBA and SBUT, more similar in structure from the perspective of the hydroxyl group, disrupt the water-oil interface in the same fashion reducing the interfacial tension by the same amount (no statistical difference with a 95% confidence interval). Similarly, IBUT and NBUT, with a longer "arm" between the hydroxyl group and the rest of the molecule, lower the water-oil interfacial tension following the same

trend (no statistical difference between them) but as much as 40% more than the other two isomers at low hydrotrope concentrations. Above the 5% molar concentration, there is no statistical difference between the isomers and the interfacial tension approaches zero.

7.2 Thickness of the interface

MDPs were obtained dividing the ADP for each molecule by the corresponding number of atom in that molecule. The total symmetric MDP was use to estimate the thickness of the interface from the parameters of the hyperbolic tangent function fitted to the profile data (refer to **Figure 15**). As expected the interface becomes thicker and smoother as the interfacial tension decreases, i.e. with increasing hydrotrope concentration. **Table 18** summarizes the thickness for all isomers, and **Figure 48** shows a universal density profile obtained by reducing the dependent and independent variables of equation 10 by the corresponding parameter for the TBA systems. From this profile, it is possible to infer that theoretical predictions true for the ternary solution near the critical point

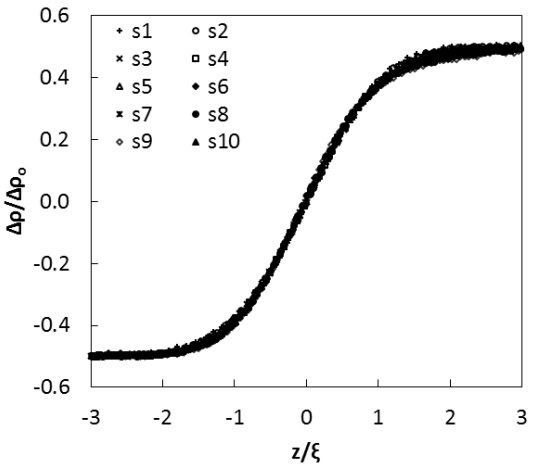

Figure 48 – Universal density profile for TBA systems derived using the fitted parameters to the total MDP for each concentration

(high TBA concentrations), should also be true far away from the critical point of the mixture. This topic is discussed more in the next section.

Table 18 – Thickness of the interface at varying hydrotrope concentrations
The coefficient of the fitted function, $\Delta\rho_o$, is included for the TBA and was used to compute the universal density profile shown in **Figure 48**.

System	Thickness (nm)	$\Delta\rho_o$ (molec/nm^3)
T0	0.322 ± 0.004	26.580 ± 0.151
T1	0.324 ± 0.000	27.100 ± 0.004
T2	0.359 ± 0.001	27.018 ± 0.004
T3	0.387 ± 0.000	26.966 ± 0.004
T4	0.422 ± 0.002	26.688 ± 0.015
T5	0.449 ± 0.004	26.509 ± 0.011
T6	0.606 ± 0.005	25.886 ± 0.024
T7	0.573 ± 0.007	25.273 ± 0.020
T8	0.624 ± 0.015	24.520 ± 0.032
T9	0.658 ± 0.021	23.687 ± 0.012
T10	0.685 ± 0.016	22.761 ± 0.047
I5	0.462 ± 0.000	
I7	0.634 ± 0.005	
I11	1.009 ± 0.048	
I12	0.738 ± 0.052	
I13	0.703 ± 0.045	
S5	0.460 ± 0.001	
S7	0.609 ± 0.012	
S11	0.835 ± 0.049	
S12	0.775 ± 0.021	
S13	0.783 ± 0.056	
N5	0.462 ± 0.003	
N7	0.650 ± 0.010	
N11	1.089 ± 0.096	
N12	0.694 ± 0.042	
N13	0.578 ± 0.026	

7.3 Comparison with experimental results

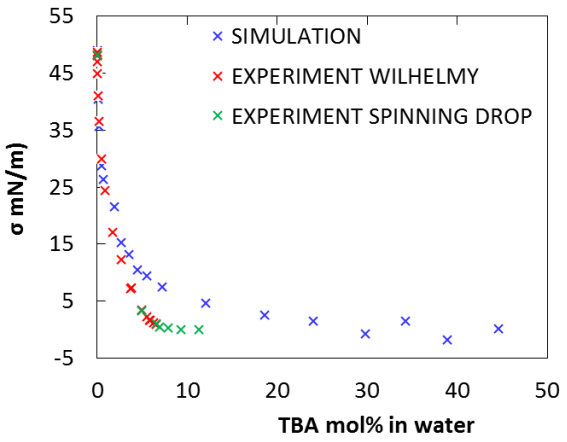

Figure 49 – Interfacial tension from experiments and simulation

TBA systems were directly compared with experimental studies done on ternary systems with the same overall composition (as listed on **Table 4**). These were carried out at a slightly lower temperature than the simulations; nonetheless, simulation values are in agreement with experiments for low to moderate TBA concentrations. **Figure 49** shows the simulation values for the interfacial tension are in good agreement with experiment at low hydrotrope concentrations (refer to **Table C.2** for the specific values). However, as TBA concentration increases, the values deviate from experiment. The simulation overestimates for the interfacial tension most likely arise from misrepresentation of the TBA-CHX interactions in the force field. These interactions are not yet fine-tuned to reflect TBA solvation in the organic phase.

The systems with high TBA concentration do not reproduce the correct alcohol concentration in the bulk oil phase, which should be non-zero as the alcohol molecules partition between the aqueous and oil phases, respectively, once the interface is saturated (see also the hydotropes' ADP in **Figure 47**). Due to this reason, the last data

points obtained from simulation were not included in the interface thickness analysis of data (Section 7.2).

The behavior of the hydrotrope varies between two extremes, one where it acts as a surfactant-like molecule due to its amphiphilic character, and another where it has a smoothing effect on the interface mimicking what happens around the critical point of the ternary mixture. The first regime, at low hydrotrope concentration, follows Gibbs theory of adsorption. While the other regime follows van der Waals theory of smooth interfaces, where the hydrotrope behaves as a co-solvent smoothing the interfacial tension until it vanishes [161]. Such behavior is described by a suggested cross-over function (equation 11); a fitted function to the entire data set (**Table C.2**) is shown in **Figure 50** as a dotted line. The experimental critical concentration was used for the experimental data set, and the concentration of the first simulated system with σ=0mN/m as an estimate of the critical concentration for the simulation data set.

$$\sigma/\sigma_o = \frac{\psi_1\psi_2}{\psi_1+\psi_2} \qquad \psi_1 = \frac{1}{1+a_1 x} \qquad \psi_2 = a_2\left(\frac{x_c - x}{x}\right)^{3.865} \qquad \textbf{(11)}$$

where a_1=1.1324; a_2=0.0085; $x_{c\text{-}exp}$=15.55mol% of TBA in aqueous solution.

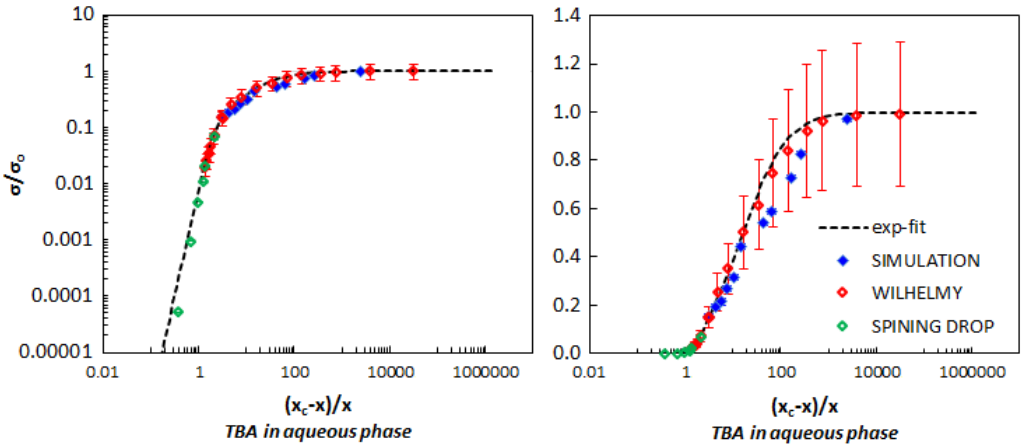

Figure 50 – Cross-over function to describe hydrotrope behavior at the interface both as a surfactant and as smoothing the interface (critical-like phenomena); representations show the behavior in (left) log-log scale and (right) semi-log scale to appreciate the simulation agreement and deviation from experiment

Figure 51 plots the relationship between the interface thickness and the reduced surface tension for the simulation data set and additional experimental measurements near the critical point of the ternary system (wat-CHX-TBA) using dynamic light scattering. The relationship is linear, which was expected from the van der Waals theoretical prediction at high hydrotrope concentrations, near the critical point of the mixture, where the interfacial thickness is to be proportional to the correlation length [160]. The large fluctuations of the interface as the critical point is approached are responsible for such

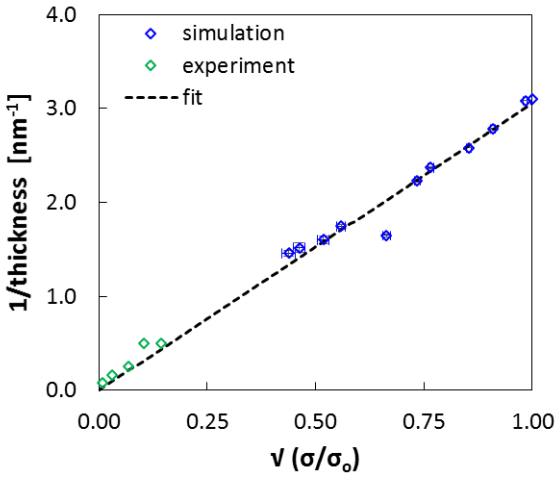

Figure 51 – Correlation between the thickness and tension at the interface

a wide interface thickness, 12 nm for the experimental system with lowest surface tension. On the other hand, simulations were carried at concentrations far away from the critical point of the mixture; remarkably the relationship between the interfacial thickness and the surface tension is still linear, which was expected given the collapse of the reduced density profiles into a universal profile that follows the Gibbs-Szyszkowski isotherm (modeled by a hyperbolic tangent in **Figure 48**).

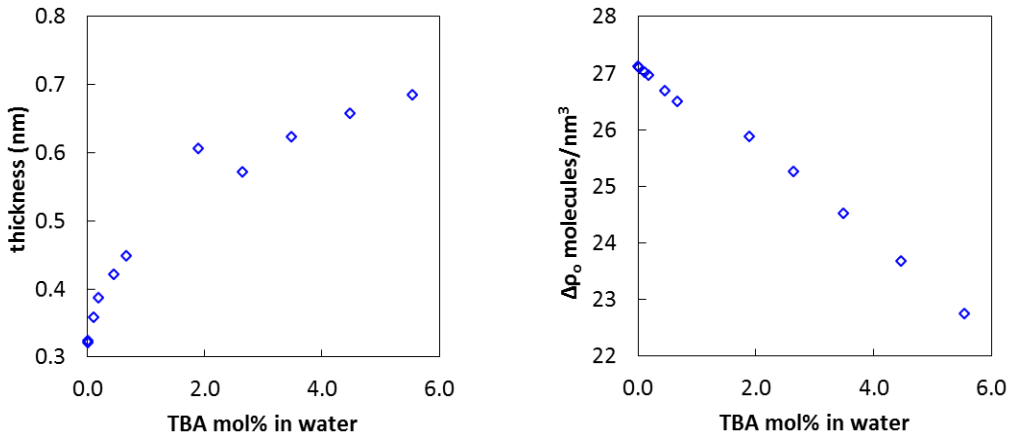

Figure 52 – Trends of the interface thickness

Examining the trend of the interface thickness (left panel in **Figure 52**) with respect to the concentration of TBA in the aqueous phase shows the same trend as the tilt angle (left panel in **Figure 45**). In addition, the difference between the bulk densities of water and cyclohexane shown in the right panel decreases linearly as more alcohol is added to the mixture. This linear trend may be steeper in the real (physical) system because TBA does not partition into the oil phase accurately in our model at higher concentrations. Nonetheless, the simulation results provide important insights in the

interfacial dynamics between water and cyclohexane when TBA, a model hydrotrope, is introduced to the solution.

Chapter 8: Future Directions

8.1 Membrane Modeling

8.1.1 Symmetric models

In a complex environment as the cell, processes take place by constantly adjusting the membrane lipid composition. Interactions between lipids themselves modulate this regulation to some extent, and affect interactions with other molecules in the cell. The results discussed in Chapter 4, as well as other cited studies, show the sterol structure not only influences the mechanical and structural properties of a membrane, but the membrane environment also affects sterol dynamics. More studies are needed to better understand the effect of lipid unsaturation and headgroup on sterol dynamics, and to characterize the effect of sterol structure on complex membrane models with enough lipid diversity to model a biological membrane, but simple enough to easily handle them with current computational tools.

The yeast organelle specific models were the first to examine the effect of sterol structure on lipid-lipid interactions in 9-lipid-component membranes with all-atom molecular dynamics. Despite their simplicity, these models are an improvement in lipid

diversity and resemblance to the membrane environments of the ER and TGN. These models serve to study important lipid-lipid interactions that modulate membrane structure and mechanical properties. Future computational studies could focus on different sterols and their interaction in complex membrane models (7+ lipid types) to understand their impact in cell health. The computation of lipid diffusion constants still remains a challenge from simulations [171]. Longer simulations trajectories and refined methods are needed to study the effect of sterol type and concentration on lipids lateral diffusion.

Additionally, the quantitative analysis of lipid clusters in symmetric, and eventually asymmetric models, can be improved to characterize the shape of clusters and interleaflet coupling. 2D RDFs can track the interactions of individual lipid clusters with respect to clusters in the opposite leaflet, which can also be used as a tool to study interleaflet coupling.

8.1.2 Asymmetric models

The production run and equilibration of these models needs to be further refine to account for lipid concentration changes in each leaflet. Specifically, the rate of sterol flip flop needs to reach proper equilibrium. A concise explanation of this issue is presented in the supplementary information of the MARTINI model for the plasma membrane study (coarse-grained model) [172]. As the sterol flips from one leaflet to the other, the increased concentration in one leaflet adds tension to the system due to

its finite size and prevents further translocation of sterols to that leaflet. That study used an iterative method by which some lipids where removed from the leaflet to which sterols were flipping to prevent additional pressure build up on the system. The method included several iterations between an asymmetric model and symmetric bilayers for each leaflet each time lipids were removed to allow proper sterol translocation between leaflets. This iteration method is not practical for all-atom simulation models due to the computational resources needed even for small membrane patches as those in presented in this study. An alternate method is needed for all-atom MD studies to achieve proper sterol distribution in the bilayer in asymmetric models. For example, combine all-atom and coarse-grained MD, or a modified version of the Highly Mobile Membrane-Mimetic (HMMM) model [173], originally developed to accelerate protein-membrane interactions while maintaining all-atom details for the lipid head group region in a bilayer.

A method to measure bilayer thickness of lipid domains in these asymmetric models is also needed. EDPs provide an estimate of the bilayer thickness based on the average location of molecules in the system, but do not explicitly show the changes in membrane thickness due to local clusters/domains. The scripts used to evaluate EDPs for this work need to be modified to account for lipid clustering and discriminate between L_o and L_d phases.

8.1.3 The role of neutralizing ions

This topic has been studied in the context of lipid-lipid interactions for the past twenty years [175]. Especially the sodium and lithium ions have been studied to determine their effect on charged membranes and on the electric field around the membrane. In recent years, other ions were examined to determine their influence on membrane structural and mechanical properties, and membrane fusion processes [176-178]. There is still need to study the binding conformations of the ions with membrane lipids to understand how they modify the membrane environment to facilitate membrane-membrane interactions. The location and coordination number of the ion-lipid complex are also of interest (see **Figure 53**), as this can shed light on lipid cluster formation and membrane electrostatics [174, 176]. It follows then, that protein-membrane interactions will be affected, mainly between proteins that bind to membranes through non-specific electrostatic interactions. The studies presented in this work used potassium ions (K^+) to neutralize the systems; calcium (Ca^{2+}) and magnesium (Mg^{2+}) ions could be systematically studied with complex bilayer models to expand current research that examines the effect of ions only in symmetric binary or

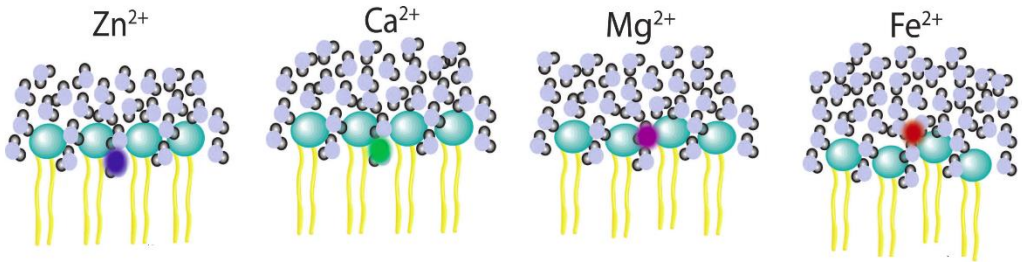

Figure 53 – Effect of ion-lipid interactions on membrane structure
Adapted from Fig. 7 in [174]

ternary lipid mixtures. Finally, study the effect of neutralizing ion and their concentration on protein binding time scales and conformation/orientation. A polarizable FF should be use capture ion-lipid interactions accurately, which in turn raises the issue of whether the current polarizable FFs are accurate enough to study biological systems, or if FF optimization would be needed prior to simulating ion-membrane dynamics.

8.2 Protein-lipid interactions

8.2.1 HMMM studies

None of the presented runs showed interaction of the mouth region of the Osh4 protein with the membrane, nor was lipid uptake observed even though the initial orientation of the protein presented its mouth region directly above the bilayer. The Osh4 studies should be revisited to use alternative methods to determine its lipid update mechanism. Osh4, and Osh3 – and another member of this family, are believed to operate similarly. Osh4 may actually bind two membranes simultaneously, facilitating membrane contact sites and lipid transport. The HMMM model [173] reduces the detail

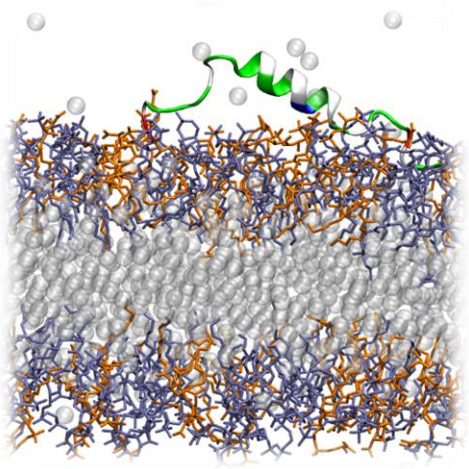

Figure 54 – Snapshot of a system build using the HMMM model
Example of one of the PC-PS systems with the ALPS-like motif using lipids with six-carbon-chains instead of the full lipid molecules.

of the hydrophobic core of the membrane by replacing it with an organic solvent, but retains the atomic detail of the lipid headgroups to study protein-lipid interactions at the surface of the bilayer (see). This model can be used to study dual-membrane models or examine other protein regions that could bind to two membranes at a time.

8.2.3 Advanced Simulation Techniques

Besides simulating the natural binding of the full protein to model bilayers, temperature replica exchange coupled with umbrella sampling can be used to obtain energy landscapes to predict a binding conformation that allows protein lipid uptake. Alternatively, energy landscapes of protein-ligand-membrane systems can be studied to work the problem backwards. A set of possible conformations for lipid unload based on the energy landscape of the system can later be simulated with MD to determine a mechanism for this process. As mentioned in section 8.1.3, inclusion of different ions at varying concentration can be simulated to see the influence of lipid-lipid interactions (as modulated by ion-lipid complexes) on protein-membrane dynamics.

8.3 Water-oil interfacial studies

8.3.1 Butanol-oil interactions

As discussed in Chapter 7, the current FF parameters do not accurately represent the interactions between butanol and the organic phase at high alcohol concentrations. Once the water-oil interface is saturated by butanol molecules, the alcohol does not

partition correctly into the organic phase, which results in an overestimate of the equilibrium alcohol concentration in water. Fine tuning of the alcohol-CHX interaction is highly needed to properly represent the behavior of this system.

Additionally, pressure profiles of the simulation would be valuable to analyze the trend of the spontaneous curvature of the interface at varying alcohol concentrations. Debugging of the pressure profile computations on NAMD needs to be done to obtain the correct pressure tensor components that can be later integrated to get the interfacial tension of the system (as an alternate method to that used in this work), and to compute the first moment of the pressure profile to study the trend of spontaneous curvature of the interface.

8.3.2 Behavior of the interface near the critical point

To test the accuracy of the tuned FF parameters for alcohol-oil interaction, simulations could be carried at different temperatures and pressures to compute a simulation phase diagram for the water-CHX-TBA ternary system to compare with the experimental one. From this diagram, a better estimate of the simulation critical point can be obtained and compared with the experimental value. Challenges to obtain the phase diagram from simulations could arise when the behavior of the system gets closer to that observed in critical phenomena (large thermal fluctuations and very smooth interface until it disappears).

Computational Resources

Stampede: Extreme Science and Engineering Discovery Environment (XSEDE) allocation on Stampede (MCB-100139)

Anton1: Anton computer time was provided by the National Center for Multiscale Modeling of Biological Systems (MMBioS) through Grant P41GM103712-S1 from the National Institutes of Health and the Pittsburgh Supercomputing Center (PSC) and our specific time is associated with the grants PSCA12035P, PSCA13048P, and PSCA14030P.

Anton2: Anton computer time was provided by the National Institutes of Health grant (R01GM116961) and the Pittsburgh Supercomputing Center (PSC) and our specific time is associated with the grant PSCA16007P.

NSF (general funding): DBI-1145652 and MCB-1149187

Deepthought and Deepthought2: Simulations and analysis were also performed in the high performance computing cluster (HPCC) of the Division of Information Technology at the University of Maryland.

Appendices

Appendix A. Symmetric ERG/CHL models

Table A.1 – Component surface areas ($Å^2$/lipid) and their standard errors

	ERG		CHL	
Lipid	er	tgn	er	tgn
sterol	25.1±0.3	32.0±0.9	33.4±1.6	22.6±0.1
dypc	61.8±0.8	64.9±0.4	65.6±0.4	67.0±0.1
dype	57.6±1.4	64.5±0.4	64.1±1.9	66.9±0.2
popi	63.1±0.4	64.3±0.7	63.8±0.7	67.0±0.2
pops	61.6±0.3	-	67.0±0.7	-
pypi	61.7±0.8	65.2±0.4	65.2±0.2	67.0±0.1
yopa	63.8±1.1	65.2±0.4	66.3±3.2	67.0±0.2
yopc	60.8±1.1	64.4±0.9	66.5±1.2	66.9±0.3
yope	53.1±1.8	63.6±0.7	66.1±3.2	66.9±0.4
yops	-	64.2±1.8	-	66.9±0.5

Table A.2 – Weighted averages of the S_{CD} values in models with ERG and CHL

Model		ER-CHL		ER-ERG			TGN-CHL		TGN-ERG	
chain		C2	C3	C2	C3		C2	C3	C2	C3
lipids	#lipids/ leaflet					#lipids/ leaflet				
dypc	42	0.119	0.126	0.123	0.124	40	0.125	0.131	0.123	0.131
dype	10	0.113	0.125	0.120	0.123	8	0.127	0.131	0.120	0.131
popi	21	0.121	0.166	0.128	0.166	13	0.128	0.177	0.128	0.175
pops	12	0.127	0.174	0.127	0.170	-	-	-	-	-
pypi	14	0.121	0.165	0.127	0.164	42	0.129	0.172	0.127	0.172
yopa	6	0.118	0.125	0.125	0.124	4	0.124	0.136	0.125	0.131
yopc	28	0.119	0.129	0.119	0.125	12	0.121	0.130	0.119	0.133
yope	10	0.114	0.123	0.115	0.124	8	0.113	0.126	0.115	0.125
yops	-	-	-	-	-	5	0.128	0.140	0.128	0.137
wt. avg		0.114	0.133	0.117	0.131		0.111	0.131	0.109	0.130

Table A.3 – Time constants (in ns) for the 3 exponential fittings to the $C_2(t)$ of the cross chain (CC) vectors for each lipid. The values here reported are the weighted averages of individual lipid wobble times for each system

	model	CC-$C_2(t)$ (3exp)		
		τ1	τ2	τ3
ERG	er	0.153 ± 0.037	1.878 ± 0.474	9.701 ± 3.285
	tgn	0.174 ± 0.172	2.141 ± 1.079	11.504 ± 2.590
CHL	er	0.090 ±0.030	1.107 ±0.204	7.258 ± 1.268
	tgn	0.109 ±0.047	1.164 ±0.391	6.416 ± 1.141

Appendix B. Asymmetric membrane models

Table B.1 – Weighted S_{CD} averages in the symmetric templates for the asymmetric models

PM-cyto	sn-1	sn-2		TGN-cyto	sn-1	sn-2
DYPC	0.010	0.009		DYPC	0.008	0.007
POPE	0.029	0.020		DYPE	0.012	0.011
POPI	0.029	0.021		POPI	0.048	0.035
POPS	0.034	0.026		PYPI	0.052	0.037
PYPI	0.021	0.015		YOPC	0.006	0.006
YOPC	0.009	0.009		YOPE	0.013	0.012
YOPE	0.018	0.016		YOPS	0.009	0.008
YOPS	0.008	0.007				
wt. avg	*0.157*	*0.122*		*wt. avg*	*0.148*	*0.115*
PM-noncyto	sn-1	sn-2		TGN-noncyto	sn-1	sn-2
DYPC	0.010	0.056		DYPC	0.045	0.043
POPE	0.019	0.011		YOPA	0.008	0.007
YOPC	0.010	0.047		YOPC	0.035	0.032
IPC	0.021	0.021		IPC	0.011	0.015
MIP2	0.059	0.028		MIP2	0.017	0.020
wt. avg	*0.119*	*0.163*		*wt. avg*	*0.116*	*0.117*

Appendix C. Additional TBA results

Table C.1 – Tilt angles of the C-OH vector in the hydrotrope molecules at the interface.

system		average molecule angle (^{o})
TBA	T5	43.97 ± 0.21
	T7	49.16 ± 0.05
	T11	53.68 ± 0.34
	T12	55.43 ± 0.28
	T13	55.94 ± 0.11
IBUT	I5	46.76 ± 0.04
	I7	50.74 ± 0.05
	I11	54.81 ± 0.21
	I12	55.75 ± 0.02
	I13	56.77 ± 0.00
SBUT	S5	44.30 ± 0.21
	S7	49.43 ± 0.25
	S11	53.89 ± 0.38
	S12	55.58 ± 0.37
	S13	56.01 ± 0.36
NBUT	N5	44.36 ± 0.14
	N7	48.29 ± 0.28
	N11	54.06 ± 0.47
	N12	55.39 ± 0.10
	N13	56.49 ± 0.07

Table C.2 – Comparison between experiment and simulation for TBA
Experimental values were provided by A.A. Novikov and A.P. Semenov from the Oil and Gas Research Institute of the Russian Academy of Sciences; and by V. N. Kuryakov and M. Anisimov from the Chemical and Biomolecular Engineering Dept. at the Univ. of Maryland

system	mol%		mass%		γ (dyn/cm)	
	sim	exp	sim	exp	simulation	experiment
S0	0.00	0.00	0.00	0.00	48.92 ± 0.03	48.8 ± 0.3
		0.00		0.002		48.3 ± 0.3
		0.00		0.016		48.2 ± 0.3
T1	0.01	0.02	0.07	0.085	47.37 ± 0.48	47.0 ± 0.3
		0.04		0.179		45.0 ± 0.3
T2	0.11	0.11	0.38	0.44	40.48 ± 0.48	41.0 ± 0.3
T3	0.18	0.22	0.70	0.90	35.67 ± 0.46	36.5 ± 0.3
T4	0.44	0.44	2.48	1.78	28.71 ± 0.52	30.0 ± 0.3
T5	0.67	0.88	2.47	3.52	26.39 ± 0.49	24.5± 0.3
T6	1.89	1.73	8.40	6.77	21.54 ± 0.58	17.1 ± 0.3
T7	2.64	2.67	8.58	10.14	15.31 ± 0.56	12.4 ± 0.3
T8	3.48	3.77	11.67	13.89	13.13 ± 0.66	7.3 ± 0.3
		3.67		13.56		7.2 ± 0.3
T9	4.47	4.95	15.42	17.64	10.46 ± 0.63	3.5 ± 0.3
T10	5.54	5.53	18.38	19.41	9.37 ± 0.63	2.3 ± 0.3
		5.79		20.18		1.7 ± 0.3
		5.91		20.54		1.7± 0.3
		6.23		21.48		1.3 ± 0.3
		6.51		22.27		0.95 ± 0.3
T11	7.23		23.27		7.41 ± 0.63	
T12	12.09		36.49		4.58 ± 0.76	
T13	18.59		48.23		2.52 ± 0.78	
T14	24.05		56.59		1.56 ± 0.38	
T15	29.79		63.62		-0.71 ± 1.36	
T16	34.24		68.20		1.44 ± 0.67	
T17	38.91		72.40		-1.77 ± 0.47	
T18	44.61		76.83		0.12 ± 1.19	
tba 0		0.00		0.00		48.30 ± 0.1932905
tba 21.6		4.95		17.64		3.26 ± 0.1430379
tba 47.98		6.51		22.27		0.98 ± 0.0414459
tba 41.3		6.96		23.53		0.52 ± 0.0197582
tba 42.2		7.89		26.06		0.23 ± 0.0133875
tba 42.67		9.32		29.71		0.05 ± 0.0014513
tba 42.92		11.32		34.42		0.00 ± 0.0017
CP_{exp}		15.55		43.10		0.00

Publications and Presentations

Accepted Publications

Graduate Work

1. **Monje-Galvan, V.**; Klauda, J.B. Two sterols, two bilayers: Insights on Membrane Structure from Molecular Dynamics. (Molecular Simulation, *submitted*)
2. Boughter, C.T.; **Monje-Galvan, V.**; Im, W.; Klauda, J.B. Influence of Cholesterol on Phospholipid Bilayer Structure and Dynamics. *J. Phys. Chem. B.*, 120(45): 11761-11772. DOI: 10.1021/acs.jpcb.6b08574
3. **Monje-Galvan, V.**; Klauda, J.B. 2016. Peripheral Membrane Proteins: Tying the Knot between Experiment and Computation. *BBA: Biomembranes*, 1858: 1584-1593 (2016).
4. **Monje-Galvan, V.**; Klauda, J.B. 2015. Modelling Yeast Organelle Membranes and How Lipid Diversity influences Bilayer Properties. *Biochemistry*. 54(45), 6852-6861. DOI: 10.1021/acs.biochem.5b00718
5. Wu, E.L.; Cheng, X.; Jo, S.; Rui, H.; Song, K.C.; Davila-Contreras, E.M.; Qi, Y.; Lee, J.; **Monje-Galvan, V.**; Venable, R.M.; Klauda, J.B.; Im, W. CHARMM-GUI Membrane Builder toward Realistic Biological Membrane Simulations. *J. Comput. Chem.* 35(27), 1997-2004 (2014).
6. Jeong, J.C.; Jo, S.; Wu, E.L.; Qi, Y.; **Monje-Galvan, V.**; Yeom, M.S.; Gorenstein, L.; Chen, F.; Klauda, J.B.; Im, W. ST-Analyzer: A web-based user interface for simulation trajectory analysis. *J. Comput. Chem.* 35(12), 957-963 (2014).

Undergraduate Work

7. Klauda, J.B.; **Monje, V.**; Kim, T.; Im, W. Improving the CHARMM Force Field for Polyunsaturated Fatty Acid Chains. *J. Phys. Chem. B.* 116(31), 9424-9431 (2012).

Accepted Book Chapters

1. Khakbaz, P; **Monje-Galvan, V**.; Zhuang, X.; Klauda, J.B. Modeling Lipid Membranes in *Handbook of Hydrocarbon and Lipid Microbiology Series*. *Biogenesis of Fatty Acids, Lipids and Membranes*. Otto Geiger, Ed. Springer, 2016 (doi:10.1007/978-3-319-43676-0_52-1).

Publications under preparation

1. **Monje-Galvan, V.**; Klauda, J.B. Peptide-membrane interactions: molecular dynamics studies on the ALPS-like motif (N-terminus) of Osh4.
2. Wildermuth, K.; **Monje-Galvan, V.**; Klauda, J.B. Peptide-membrane interactions: HMMM studies on the ALPS-like motif (N-terminus) of Osh4.
3. **Monje-Galvan, V.**; Sanchez, Edgar; Klauda, J.B. Interfacial properties of aqueous solutions of butanol isomers and cyclohexane.
4. Novikov, A; Semenov, A.; Kuryakov, V.; **Monje-Galvan, V.**; Klauda, J.B.; Anisimov, M. Crossover between surfactant-like and critical interfacial phenomena in solutions of a hydrotrope
5. **Monje-Galvan, V**.; Klauda, J.B. Asymmetric models for the plasma and trans-Golgi network membranes of yeast *S. cerevisiae*.

Presentations (delivered)

1. **Monje-Galvan, V.** & Klauda, J.B. "Asymmetric membrane models for the PM and TGN of yeast, an all-atom molecular dynamics study." *Biophysical Society* (2017)
2. **Monje-Galvan, V.** & Klauda, J.B. "L_o/L_d Phase Coexistence and Interaction in Model Membranes with IPC Lipids." *Delaware Membrane Protein Symposium* (2016, poster presentation)
3. **Monje-Galvan, V.** & Klauda, J.B. "L_o/L_d Phase Coexistence and Interaction in Model Membranes with IPC Lipids." *Biophysical Society* (2016)
4. **Monje-Galvan, V.** & Klauda, J.B. "Interfacial Properties of Aqueous Solutions of TBA and Cyclohexane." *Congress of Theoretical Chemists of the Latin Expression, Chitel* (2015, Poster in Spanish)
5. **Monje-Galvan, V.** & Klauda, J.B. "Membrane binding of the Osh4 curvature-sensing peptide." *Delaware Membrane Protein Symposium* (2015, poster presentation)
6. **Monje-Galvan, V.** & Klauda, J.B. "Membrane binding of the Osh4 curvature-sensing peptide." *Biophysical Society* (2015)
7. **Monje-Galvan, V.** & Klauda, J.B. "Binding studies of a *Saccharomyces Cerevisiae* peripheral protein Osh4" *American Chemical Society* (2015)
8. **Monje-Galvan, V.** & Klauda, J.B. "Membrane binding of a curvature-sensing peptide of a lipid transport protein in yeast." *XL Congress of Theoretical Chemists of the Latin Expression QUITEL* (2014, Talk in Spanish).

9. **Monje-Galvan, V.** & Klauda, J.B. "Molecular dynamic studies on organelle-specific yeast membrane models and amphipathic lipid packing sensor motif binding mechanism." *Biophysical Society* (2014).
10. **Monje-Galvan, V.** & Klauda, J.B. "Simulation studies on organelle-specific yeast membrane models and amphipathic lipid packing sensor motif binding mechanism." *AIChE National Meeting* (2013).
11. **Monje-Galvan, V.** & Klauda, J.B. "Improved CHARMM Force Field for Polyunsaturated Fatty Acid Chains, a Study on DAPC Membranes." *Biophysical Society* (2013)

Invited talks (delivered and scheduled)

1. **Monje-Galvan, V.;** Klauda, J.B. "Symmetric and asymmetric computational membrane models for yeast, insights on lipid-lipid interactions." Universidad Mayor de San Andrés - Instituto de Investigaciones Físicas (La Paz, Bolivia) (2017).
2. **Monje-Galvan, V.;** Klauda, J.B. "Interfacial behavior of hydrotropes in aqueous solutions." Universidad Mayor de San Andrés – Facultad de Ingeniería Química (La Paz, Bolivia) (2017).
3. **Monje-Galvan, V.;** Klauda, J.B. "Mejorando el campo de fuerza para simulaciones moleculares de ácidos grasos poliinsaturados en membranas celulares." Universidad Mayor de San Andrés - Instituto de Investigaciones Físicas (La Paz, Bolivia) (2013).

References

1. van Meer G, Voelker DR, Feigenson GW. Membrane lipids: where they are and how they behave. Nature Reviews Molecular Cell Biology. 2008;9(2):112-24. doi: 10.1038/nrm2330. PubMed PMID: ISI:000252676600012.
2. Fletcher DA, Mullins RD. Cell mechanics and the cytoskeleton. Nature. 2010;463(7280):485-92. Epub 2010/01/30. doi: 10.1038/nature08908. PubMed PMID: 20110992; PubMed Central PMCID: PMCPmc2851742.
3. Holthuis JCM, Menon AK. Lipid landscapes and pipelines in membrane homeostasis. Nature. 2014;510(7503):48-57. doi: 10.1038/nature13474. PubMed PMID: WOS:000336768900031.
4. Engelman DM. Membranes are more mosaic than fluid. Nature. 2005;438(7068):578-80. doi: doi:10.1038/nature04394.
5. Altmann K, Dürr M, Westermann B. Saccharomyces cerevisiae as a Model Organism to Study Mitochondrial Biology. In: Leister D, Herrmann JM, editors. Mitochondria: Practical Protocols. Totowa, NJ: Humana Press; 2007. p. 81-90.
6. Nelson DL, Cox MM. Principles of Biochemistry. 5th ed. New York: W.H. Freeman and Company.
7. Klug L, Daum G. Yeast lipid metabolism at a glance. FEMS Yeast Research. 2014;14(3):369-88. doi: 10.1111/1567-1364.12141.
8. Seelig A, Seelig J. Dynamic structure of fatty acyl chains in a phospholipid bilayer measured by deuterium magnetic resonance. Biochemistry. 1974;13(23):4839-45. doi: 10.1021/bi00720a024.
9. Seelig A, Seelig J. Bilayers of dipalmitoyl-3-sn-phosphatidylcholine. Conformational differences between the fatty acyl chains. Biochimica et biophysica acta. 1975;406(1):1-5. Epub 1975/09/16. PubMed PMID: 1242107.
10. Seelig J, Waespe-Sarcevic N. Molecular order in cis and trans unsaturated phospholipid bilayers. Biochemistry. 1978;17(16):3310-5. Epub 1978/08/08. PubMed PMID: 687586.
11. Klauda JB, Eldho NV, Gawrisch K, Brooks BR, Pastor RW. Collective and noncollective models of NMR relaxation in lipid vesicles and multilayers. J Phys Chem B. 2008;112(19):5924-9. Epub 2008/01/09. doi: 10.1021/jp075641w. PubMed PMID: 18179193.
12. Perly B, Smith IC, Jarrell HC. Acyl chain dynamics of phosphatidylethanolamines containing oleic acid and dihydrosterculic acid: 2H NMR relaxation studies. Biochemistry. 1985;24(17):4659-65. Epub 1985/08/13. PubMed PMID: 4063348.
13. Rest MEvd, Kamminga AH, Nakano A, Anraku Y, Poolman B, Konings WN. The plasma membrane of Saccharomyces cerevisiae: structure, function, and biogenesis. Microbiology and Molecular Biology Reviews. 1995;59(2):304-22.

14. Maxfield FRT, Ira. Role of cholesterol and lipid organization in disease. Nature. 2005;438(7068):612-21. doi: doi:10.1038/nature04399.
15. Klemm RW, Ejsing CS, Surma MA, Kaiser H-J, Gerl MJ, Sampaio JL, et al. Segregation of sphingolipids and sterols during formation of secretory vesicles at the trans-Golgi network. The Journal of Cell Biology. 2009;185(4):601-12. doi: 10.1083/jcb.200901145.
16. Santos AXS, Riezman H. Yeast as a model system for studying lipid homeostasis and function. FEBS Letters. 2012.
17. Zwier MC, Chong LT. Reaching biological timescales with all-atom molecular dynamics simulations. Curr Opin Pharmacol. 2010;10(6):745-52. doi: 10.1016/j.coph.2010.09.008. PubMed PMID: 20934381.
18. Arora A, Raghuraman H, Chattopadhyay A. Influence of cholesterol and ergosterol on membrane dynamics: a fluorescence approach ☆. Biochimica et Biophysica Acta (BBA) Reseach Communications. 2004;318(4):920–6. doi: 10.1016/j.bbrc.2004.04.118.
19. Ferreira TM, Coreta-Gomes F, Ollila OHS, Moreno MJ, Vaz WLC, Topgaard D. Cholesterol and POPC segmental order parameters in lipid membranes: solid state 1H-13C NMR and MD simulation studies. Physical Chemistry Chemical Physics. 2013;15(6):1976-89. doi: 10.1039/C2CP42738A.
20. Róg T, Pasenkiewicz-Gierula M, Vattulainen I, Karttunen M. Ordering effects of cholesterol and its analogues. Biochimica et Biophysica Acta (BBA) - Biomembranes. 2009;1788(1):97-121. doi: http://dx.doi.org/10.1016/j.bbamem.2008.08.022.
21. Klose C, Ejsing CS, Garcia-Siez AJ, Kaiser H-J, Sampaio JL, Surma MA, et al. Yeast Lipids Can Phase-separate into Micrometer-scale Membrane Domains. Journal of Biological Chemistry. 2010;285(39):30224-32. doi: 10.1074/jbc.M110.123554.
22. Bennett WFD, Tieleman DP. Computer simulations of lipid membrane domains. Biochimica et Biophysica Acta (BBA) - Biomembranes. 2013;1828(8):1765-76. doi: http://dx.doi.org/10.1016/j.bbamem.2013.03.004.
23. Davis JH, Clair JJ, Juhasz J. Phase equilibria in DOPC/DPPC-d62/cholesterol mixtures. Biophysical journal. 2009;96(2):521-39. Epub 2009/01/27. doi: 10.1016/j.bpj.2008.09.042. PubMed PMID: 19167302; PubMed Central PMCID: PMCPmc2716451.
24. Engberg O, Nurmi H, Nyholm TKM, Slotte JP. Effects of Cholesterol and Saturated Sphingolipids on Acyl Chain Order in 1-Palmitoyl-2-oleoyl-sn-glycero-3-phosphocholine Bilayers—A Comparative Study with Phase-Selective Fluorophores. Langmuir : the ACS journal of surfaces and colloids. 2015;31(14):4255-63. doi: 10.1021/acs.langmuir.5b00403.
25. Yasuda T, Matsumori N, Tsuchikawa H, Lönnfors M, Nyholm TKM, Slotte JP, et al. Formation of Gel-like Nanodomains in Cholesterol-Containing Sphingomyelin or Phosphatidylcholine Binary Membrane As Examined by Fluorescence Lifetimes and

2H NMR Spectra. Langmuir : the ACS journal of surfaces and colloids. 2015;31(51):13783-92. doi: 10.1021/acs.langmuir.5b03566.
26. Monje-Galvan V. Computational Studies on Organelle-Specific Yeas Membrane Models: University of Maryland, College Park; 2014.
27. Monje-Galvan V, Klauda JB. Modelling Yeast Organelle Membranes and How Lipid Diversity influences Bilayer Properties. Biochemistry. 2015;54:6852-61. Epub October 26, 2015. doi: 10.1021/acs.biochem.5b00718.
28. Bankaitis VA, Garcia-Mata R, Mousley CJ. Golgi Membrane Dynamics and Lipid Metabolism. Current Biology. 2012;22(10):R414-24. doi: 10.1016/j.cub.2012.03.004. PubMed PMID: 22625862.
29. Leber A, Hrastnick C, Daum G. Phospholipid-synthesizing enzymes in Golgi membranes of the yeast, Saccharomyces cerevisiae. FEBS Letters. 1995;377(2):271-4. doi: 10.1016/0014-5793(95)01361-X.
30. Bastos AEP, Marinho HS, Cordeiro AM, de Soure AM, de Almeida RFM. Biophysical properties of ergosterol-enriched lipid rafts in yeast and tools for their study: characterization of ergosterol/phosphatidylcholine membranes with three fluorescent membrane probes. Chemistry and Physics of Lipids. 2012;165(5):577-88. doi: 10.1016/j.chemphyslip2012.06.002. PubMed PMID: WOS:000308681700009.
31. Schneiter R, Brügger B, Sandhoff R, Zellnig G, Leber A, Lampl M, et al. Electrospray Ionization Tandem Mass Spectrometry (Esi-Ms/Ms) Analysis of the Lipid Molecular Species Composition of Yeast Subcellular Membranes Reveals Acyl Chain-Based Sorting/Remodeling of Distinct Molecular Species En Route to the Plasma Membrane. The Journal of Cell Biology. 1999;146(4):741-54. doi: 10.1083/jcb.146.4.741.
32. Fagone P, Jackowski S. Membrane phospholipid synthesis and endoplasmic reticulum function. Journal of Lipid Research. 2009;50:S311-S6. doi: 10.1194/jlr.R800049-JLR200.
33. Niemela PS, Hyvonen MT, Vattulainen I. Influence of chain length and unsaturation on sphingomyelin bilayers. Biophysical journal. 2006;90(3):851-63. doi: 10.1529/biophysj.105.067371. PubMed PMID: 16284257; PubMed Central PMCID: PMCPMC1367110.
34. Sadeghi S, Muller M, Vink RLC. Raft Formation in Lipid Bilayers Coupled to Curvature. Biophysical journal. 2014;107:1591-600. doi: 10.1016/j.bpj.2014.07.072.
35. Sodt AJ, Sandar ML, Gawrisch K, Pastor RW, Lyman E. The Molecular Structure of the Liquid-Ordered Phase of Lipid Bilayers. Journal of the American Chemical Society. 2014;136(2):725-32. doi: 10.1021/ja4105667.
36. Eggeling C, Ringemann C, Medda R, Schwarzmann G, Sandhoff K, Polyakova S, et al. Direct observation of the nanoscale dynamics of membrane lipids in a living cell. Nature. 2009;457(7233):1159-62.
37. Sezgin E, Levental I, Grzybek M, Schwarzmann Gn, Mueller V, Honigmann A, et al. Partitioning, diffusion, and ligand binding of raft lipid analogs in model and

cellular plasma membranes. Biochimica et Biophysica Acta (BBA) - Biomembranes. 2012;1818(7):1777-84. doi: http://dx.doi.org/10.1016/j.bbamem.2012.03.007.
38. Holthuis JCM, Pomorski T, Raggers RJ, Sprong H, Van Meer G. The Organizing Potential of Sphingolipids in Intracellular Membrane Transport. Physiological Reviews. 2001;81(4):1689-723.
39. Lindberg L, Santos AX, Riezman H, Olsson L, Bettiga M. Lipidomic profiling of Saccharomyces cerevisiae and Zygosaccharomyces bailii reveals critical changes in lipid composition in response to acetic acid stress. PLoS One. 2013;8(9):e73936. doi: 10.1371/journal.pone.0073936. PubMed PMID: 24023914; PubMed Central PMCID: PMCPMC3762712.
40. Chiantia S, London E. Acyl Chain Length and Saturation Modulate Interleaflet Coupling in Asymmetric Bilayers: Effects on Dynamics and Structural Order. Biophysical journal. 2012;103(11):2311-9. doi: http://dx.doi.org/10.1016/j.bpj.2012.10.033.
41. Klemm RW, Ejsing CS, Surma MA, Kaiser H-J, Gerl MJ, Sampaio JL, et al. Segregation of sphingolipids and sterols during formation of secretory vesicles at the trans-Golgi network. The Journal of Cell Biology. 2009;185(4):601-12. doi: 10.1083/jcb.200901145.
42. Simons K, Ikonen E. How Cells Handle Cholesterol. Science. 2000;290(5497):1721-26. doi: 10.1126/science.290.5497.1721.
43. Vanegas JM, Contreras MF, Faller R, Longo ML. Role of unsaturated lipid and ergosterol in ethanol tolerance of model yeast biomembranes. Biophysical journal. 2012;102(3):507-16. Epub 2012/02/14. doi: 10.1016/j.bpj.2011.12.038. PubMed PMID: 22325273; PubMed Central PMCID: PMCPmc3274781.
44. Collins MD. Interleaflet Coupling Mechanisms in Bilayers of Lipids and Cholesterol☆. Biophysical journal. 2008;94(5):L32-4. doi: 10.1529/biophysj.107.124362. PubMed PMID: 18096628; PubMed Central PMCID: PMC2242768.
45. Venable RM, Sodt AJ, Rogaski B, Rui H, Hatcher E, MacKerell AD, et al. CHARMM All-Atom Additive Force Field for Sphingomyelin: Elucidation of Hydrogen Bonding and of Positive Curvature. Biophysical journal. 2014;107(1):134-45. doi: 10.1016/j.bpj.2014.05.034. PubMed PMID: WOS:000338411600017.
46. Jo S, Lim JB, Klauda JB, Im W. CHARMM-GUI Membrane Builder for mixed bilayers and its application to yeast membranes. Biophysical journal. 2009;97(1):50-8. Epub 2009/07/08. doi: 10.1016/j.bpj.2009.04.013. PubMed PMID: 19580743; PubMed Central PMCID: PMCPmc2711372.
47. Marquardt D, Kucerka N, Wassall SR, Harroun TA, Katsaras J. Cholesterol's location in lipid bilayers. Chem Phys Lipids. 2016;199:17-25. doi: 10.1016/j.chemphyslip.2016.04.001. PubMed PMID: 27056099.
48. Kessel A, Ben-Tal N, May S. Interactions of cholesterol with lipid bilayers: the preferred configuration and fluctuations. Biophysical journal. 2001;81:643-58.

49. Martinez-Seara H, Rog T, Karttunen M, Vattulainen I, Reigada R. Cholesterol induces specific spatial and orientational order in cholesterol/phospholipid membranes. PLoS One. 2010;5(6):e11162. doi: 10.1371/journal.pone.0011162. PubMed PMID: 20567600; PubMed Central PMCID: PMCPMC2887443.
50. Boughter CT, Monje-Galvan V, Im W, Klauda JB. Influence of Cholesterol on Phospholipid Bilayer Structure and Dynamics. J Phys Chem B. 2016;120(45):11761-72. doi: 10.1021/acs.jpcb.6b08574. PubMed PMID: 27771953.
51. Khelashvili G, Harries D. How cholesterol tilt modulates the mechanical properties of saturated and unsaturated lipid membranes. J Phys Chem B. 2013;117(8):2411-21. doi: 10.1021/jp3122006. PubMed PMID: 23323733.
52. Marquardt D, Heberle FA, Greathouse DV, Koeppe RE, Standaert RF, Van Oosten BJ, et al. Lipid bilayer thickness determines cholesterol's location in model membranes. Soft matter. 2016;12(47):9417-28. doi: 10.1039/c6sm01777k.
53. Róg T, Pasenkiewicz-Gierula M. Cholesterol effects on the phospholipid condensation and packing in the bilayer: a molecular simulation study. FEBS Letters. 2001;502(1-2):68-71. doi: 10.1016/s0014-5793(01)02668-0.
54. Bui TT, Suga K, Umakoshi H. Roles of Sterol Derivatives in Regulating the Properties of Phospholipid Bilayer Systems. Langmuir : the ACS journal of surfaces and colloids. 2016;32(24):6176-84. doi: 10.1021/acs.langmuir.5b04343. PubMed PMID: 27158923.
55. Czub J, Baginski M. Comparative molecular dynamics study of lipid membranes containing cholesterol and ergosterol. Biophysical journal. 2006;90(7):2368-82. Epub 2006/01/10. doi: 10.1529/biophysj.105.072801. PubMed PMID: 16399829; PubMed Central PMCID: PMCPmc1403193.
56. Poyry S, Róg T, Karttunen M, Vattulainen I. Significance of cholesterol methyl groups. J Phys Chem B. 2008;112(10):2922-9.
57. Cournia Z, Ullmann GM, Smith JC. Differential Effects of Cholesterol, Ergosterol and Lanosterol on a Dipalmitoyl Phosphatidylcholine Membrane: A Molecular Dynamics Simulation Study. The Journal of Physical Chemistry B. 2007;111(7):1786-801. doi: 10.1021/jp065172i.
58. Endress E, Bayerl S, Prechtel K, maier C, Merkel, Bayerl TM. The Effect of Cholesterol, Lanosterol, and Ergosterol on Lecithin Bilayer Mechanical Properties at Molecular and Microscopic Dimensions: A Solid-State NMR and Micropipet Study. Langmuir : the ACS journal of surfaces and colloids. 2002;18(8):3293-9. doi: 10.1021/la011596m.
59. Rog T, Pasenkiewicz-Gierula M, Vattulainen I, Karttunen M. What happens if cholesterol is made smoother: importance of methyl substituents in cholesterol ring structure on phosphatidylcholine-sterol interaction. Biophysical journal. 2007;92(10):3346-57. doi: 10.1529/biophysj.106.095497. PubMed PMID: 17293396; PubMed Central PMCID: PMCPMC1853147.

60. Mannock DA, Lewis RN, McMullen TP, McElhaney RN. The effect of variations in phospholipid and sterol structure on the nature of lipid-sterol interactions in lipid bilayer model membranes. Chem Phys Lipids. 2010;163(6):403-48. doi: 10.1016/j.chemphyslip.2010.03.011. PubMed PMID: 20371224.
61. Mannock DA, Lewis RN, McElhaney RN. A calorimetric and spectroscopic comparison of the effects of ergosterol and cholesterol on the thermotropic phase behavior and organization of dipalmitoylphosphatidylcholine bilayer membranes. Biochimica et biophysica acta. 2010;1798(3):376-88. doi: 10.1016/j.bbamem.2009.09.002. PubMed PMID: 19761759.
62. Hung W-C, Lee M-T, Chung H, Sun Y-T, Chen H, Charron NE, et al. Comparative Study of the Condensing Effects of Ergosterol and Cholesterol. Biophysical journal. 2016;110(9):2026-33. doi: 10.1016/j.bpj.2016.04.003.
63. Stryer L. Molecular Design of Life. New York, USA: W.H. Freeman and Company; 1989.
64. Paloncýová M, DeVane R, Murch B, Berka K, Otyepka M. Amphiphilic Drug-Like Molecules Accumulate in a Membrane below the Head Group Region. The Journal of Physical Chemistry B. 2014;118(4):1030-9. doi: 10.1021/jp4112052.
65. Yoo B, Shah JK, Zhu Y, Maginn EJ. Amphiphilic interactions of ionic liquids with lipid biomembranes: a molecular simulation study. Soft matter. 2014;10(43):8641-51. doi: 10.1039/C4SM01528B.
66. Jackson CL, Bouvet S. Arfs at a Glance. Journal of Cell Science. 2014;127(19):4103.
67. Drin G, Casella J-F, Gautier R, Boehmer T, Schwartz TU, Antonny B. A general amphipathic alpha-helical motif for sensing membrane curvature. Nature structural & molecular biology. 2007;14(2):138-46. doi: 10.1038/nsmb1194. PubMed PMID: WOS:000244031900012.
68. Bigay J, Casella JF, Drin G, Mesmin B, Antonny B. ArfGAP1 responds to membrane curvature through the folding of a lipid packing sensor motif. Embo Journal. 2005;24(13):2244-53. doi: 10.1038/sj.emboj.7600714. PubMed PMID: WOS:000230956500002.
69. Vanni S, Vamparys L, Gautier R, Drin G, Etchebest C, Fuchs PFJ, et al. Amphipathic Lipid Packing Sensor Motifs: Probing Bilayer Defects with Hydrophobic Residues. Biophysical journal. 2013;104(3):575-84. doi: 10.1016/j.bpj.2012.11.3837. PubMed PMID: WOS:000314619900008.
70. Miller CM, Brown AC, Mittal J. Disorder in Cholesterol-Binding Functionality of CRAC Peptides: A Molecular Dynamics Study. The Journal of Physical Chemistry B. 2014;118(46):13169-74. doi: 10.1021/jp5106423.
71. Ikeda K, Kameda T, Harada E, Akutsu H, Fujiwara T. Combined Use of Replica-Exchange Molecular Dynamics and Magic-Angle-Spinning Solid-State NMR Spectral Simulations for Determining the Structure and Orientation of Membrane-

Bound Peptide. The Journal of Physical Chemistry B. 2011;115(29):9327-36. doi: 10.1021/jp205290t.
72. Brice AR, Lazaridis T. Structure and Dynamics of a Fusion Peptide Helical Hairpin on the Membrane Surface: Comparison of Molecular Simulations and NMR. The Journal of Physical Chemistry B. 2014;118(17):4461-70. doi: 10.1021/jp409412g.
73. Monje-Galvan V, Klauda JB. Peripheral membrane proteins: Tying the knot between experiment and computation. Biochimica et biophysica acta. 2016;1858(7 Pt B):1584-93. doi: 10.1016/j.bbamem.2016.02.018. PubMed PMID: 26903211.
74. D'Angelo G, Vicinanza M, De Matteis MA. Lipid-transfer proteins in biosynthetic pathways. Current Opinion in Cell Biology. 2008;20(4):360–70. doi: 10.1016/j.ceb.2008.03.013.
75. Lev S. Non-vesicular lipid transport by lipid-transfer proteins and beyond. Nature Reviews Molecular Cell Biology. 2010;11(10):739-50. doi: 10.1038/nrm2971. PubMed PMID: WOS:000282152800016.
76. Seaton BA, Roberts MF. Peripheral membrane Proteins: Birkhäuser Boston; 1996.
77. Prinz WA. Lipid Trafficking sans Vesicles: Where, Why, How? Cell. 2010;143(6):870-4. doi: 10.1016/j.cell.2010.11.031. PubMed PMID: WOS:000285182600005.
78. Hanada K, Kumagai K, Yasuda S, Miura Y, Kawano M, Fukasawa M, et al. Molecular machinery for non-vesicular trafficking of ceramide. Nature. 2003;426:803-9.
79. Holthuis JCM, Levine TP. Lipid traffic: Floppy drives and a superhighway. Nature Reviews Molecular Cell Biology. 2005;6(3):209-20. doi: 10.1038/nrm1591. PubMed PMID: WOS:000227303200014.
80. Lahiri S, Toulmay A, Prinz WA. Membrane contact sites, gateways for lipid homeostasis. Curr Opin Cell Biol. 2015;33:82-7. Epub 2015/01/09. doi: 10.1016/j.ceb.2014.12.004. PubMed PMID: 25569848; PubMed Central PMCID: PMCPMC4380522.
81. Menon AK, Levine TP. Countercurrents in flipid flow. Nature. 2015;525:191-2. doi: 10.1038/525191a.
82. Lehto M, Olkkonen VM. The OSBP-related proteins: a novel protein family involved in vesicle transport, cellular lipid metabolism, and cell signalling. Biochimica Et Biophysica Acta-Molecular And Cell Biology Of Lipids. 2003;1631(1):1-11. PubMed PMID: ISI:000180998200001.
83. Raychaudhuri S, Im YJ, Hurley JH, Prinz WA. Nonvesicular sterol movement from plasma membrane to ER requires oxysterol-binding protein-related proteins and phosphoinositides. J Cell Biol. 2006;173(1):107-19. PubMed PMID: ISI:000236766900013.

84. Ngo MH, Colbourne TR, Ridgway ND. Functional implications of sterol transport by the oxysterol-binding protein gene family. Biochemical Journal. 2010;429(1):13-24. doi: 10.1042/bj20100263.
85. Schulz TA, Prinz WA. Sterol transport in yeast and the oxysterol binding protein homologue (OSH) family. Biochimica Et Biophysica Acta-Molecular and Cell Biology of Lipids. 2007;1771(6):769-80. PubMed PMID: ISI:000247554900013.
86. Tong J, Yang H, Yang HY, Eom SH, Im YJ. Structure of Osh3 Reveals a Conserved Mode of Phosphoinositide Binding in Oxysterol-Binding Proteins. Structure. 2013;21(7):1203-13. doi: 10.1016/j.str.2013.05.007. PubMed PMID: WOS:000321681600017.
87. de Saint-Jean M, Delfosse V, Douguet D, Chicanne G, Payrastre B, Bourguet W, et al. Osh4p exchanges sterols for phosphatidylinositol 4-phosphate between lipid bilayers. The Journal of cell biology. 2011;195(6):965-78. doi: 10.1083/jcb.201104062. PubMed PMID: 22162133; PubMed Central PMCID: PMC3241724.
88. von Filseck JM, Copic A, Delfosse V, Vanni S, Jackson CL, Bourguet W, et al. Phosphatidylserine transport by ORP/Osh proteins is driven by phosphatidylinositol 4-phosphate. Science. 2015;349(6246):432-6. doi: 10.1126/science.aab1346. PubMed PMID: WOS:000358381400044.
89. Ling Y, Hayano S, Novick P. Osh4p is needed to reduce the level of phosphatidylinositol-4-phosphate on secretory vesicles as they mature. Molecular Biology of the Cell. 2014;25:3389-400. doi: 10.1091/mbc.E14-06-1087.
90. Moser von Filseck J, Copic A, Delfosse V, Vanni S, Jackson CL, Bourguet W, et al. INTRACELLULAR TRANSPORT. Phosphatidylserine transport by ORP/Osh proteins is driven by phosphatidylinositol 4-phosphate. Science. 2015;349(6246):432-6. Epub 2015/07/25. doi: 10.1126/science.aab1346. PubMed PMID: 26206936.
91. Levine TP. Lipid traffic: Osh4p makes an unexpected exchange. The Journal of cell biology. 2011;195(6):927-9. doi: 10.1083/jcb.201111074.
92. LeBlanc MA, McMaster CR. Lipid Binding Requirements for Oxysterol-binding Protein Kes1 Inhibition of Autophagy and Endosome-trans-Golgi Trafficking Pathways. Journal of Biological Chemistry. 2010;285(44):33875-84. doi: 10.1074/jbc.M110.147264.
93. Li XM, Rivas MP, Fang M, Marchena J, Mehrotra B, Chaudhary A, et al. Analysis of oxysterol binding protein homologue Kes1p function in regulation of Sec14p-dependent protein transport from the yeast Golgi complex. Journal of Cell Biology. 2002;157(1):63-77. doi: 10.1083/jcb.200201037. PubMed PMID: WOS:000176426600005.
94. LeBlanc MA, Fairn GD, Russo SB, Czyz O, Zaremberg V, Cowart LA, et al. The Yeast Oxysterol Binding Protein Kes1 Maintains Sphingolipid Levels. Plos One. 2013;8(4):6. doi: 10.1371/journal.pone.0060485. PubMed PMID: WOS:000319108100047.

95. Schulz TA, Choi M-G, Raychaudhuri S, Mears JA, Ghirlando R, Hinshaw JE, et al. Lipid-regulated sterol transfer between closely apposed membranes by oxysterol-binding protein homologues. The Journal of cell biology. 2009;187(6):889-903.
96. Rogaski B, Lim JB, Klauda JB. Sterol binding and membrane lipid attachment to the Osh4 protein of yeast. J Phys Chem B. 2010;114(42):13562-73.
97. Rogaski B, Klauda JB. Membrane-Binding Mechanism of a Peripheral Membrane Protein through Microsecond Molecular Dynamics Simulations. Journal of Molecular Biology. 2012;423(5):847-61. doi: 10.1016/j.jmb.2012.08.015. PubMed PMID: WOS:000310666400015.
98. Moser von Filseck J, Vanni S, Mesmin B, Antonny B, Drin G. A phosphatidylinositol-4-phosphate powered exchange mechanism to create a lipid gradient between membranes. Nature Communications. 2015;6:6671:1-12. doi: doi:10.1038/ncomms7671.
99. Antonny B. Mechanisms of Membrane Curvature Sensing. Annual Review of Biochemistry, Vol 80. 2011;80:101-23. doi: 10.1146/annurev-biochem-052809-155121. PubMed PMID: WOS:000292895600005.
100. Doucet CM, Esmery N, de Saint-Jean M, Antonny B. Membrane Curvature Sensing by Amphipathic Helices Is Modulated by the Surrounding Protein Backbone. PLOS ONE. 2015;10(9):e0137965. doi: 10.1371/journal.pone.0137965.
101. Safran S. Statistical Thermodynamics Of Surfaces, Interfaces, And Membranes: Westview Press; 2003.
102. Small DM. Handbook of Lipid Research. Hanahan DJ, editor. New York: Plenum Press; 1986.
103. Robertson AE, Phan DH, Macaluso JE, Kuryakov VN, Jouravleva EV, Bertrand CE, et al. Mesoscale solubilization and critical phenomena in binary and quasi-binary solutions of hydrotropes. Fluid Phase Equilibria. 2016;407:243-54. doi: http://dx.doi.org/10.1016/j.fluid.2015.06.030.
104. Hodgdon TK, Kaler EW. Hydrotropic solutions. Current Opinion in Colloid & Interface Science. 2007;12(3):121-8. doi: 10.1016/j.cocis.2007.06.004.
105. Neuberg C. Hydrotropische erscheinungen. Biochem Z. 1916;76(107-176).
106. Subramanian D, Boughter CT, Klauda JB, Hammouda B, Anisimov MA. Mesoscale inhomogeneities in aqueous solutions of small amphiphilic molecules. Faraday Discussions. 2013;167:217-38. doi: 10.1039/C3FD00070B.
107. Subramanian D, Klauda JB, Collings PJ, Anisimov MA. Mesoscale Phenomena in Ternary Solutions of Tertiary Butyl Alcohol, Water, and Propylene Oxide. The Journal of Physical Chemistry B. 2014;118(22):5994-6006. doi: 10.1021/jp4125183.
108. Leach AR. Molecular Modeling Principles and Applications. 2 ed. Great Britain: Pearson Education; 2001. 727 p.
109. Frenkel D, Smit B. Understanding Molecular Simulation From Algorithms to Applications. 2 ed: Academic Press; 2001 24 October 2001. 664 p.

110. Brooks BR, Brooks CL, Mackerell J. AD, Nilsson L, Petrella RJ, Roux B, et al. CHARMM: The biomolecular simulation program. Journal of Computational Chemistry. 2009;30(10):1545-614. doi: 10.1002/jcc.21287.
111. Dickson CJ, Madej BD, Skjevik ÅA, Betz RM, Teigen K, Gould IR, et al. Lipid14: The Amber Lipid Force Field. Journal of Chemical Theory and Computation. 2014;10(2):865-79. doi: 10.1021/ct4010307.
112. Case DA, Betz RM, Botello-Smith W, Cerutti DS, Cheatham TE, Darden T, et al. AMBER16. Amber16 ed. University o California, San Francisco2016.
113. Reif MM, Winger M, Oostenbrink C. Testing of the GROMOS Force-Field Parameter Set 54A8: Structural Properties of Electrolyte Solutions, Lipid Bilayers, and Proteins. Journal of Chemical Theory and Computation. 2013;9(2):1247-64. doi: 10.1021/ct300874c.
114. Marrink SJ, Risselada HJ, Yefimov S, Tieleman DP, H. dV. The MARTINI Force Field: Coarse Grained Model for Biomolecular Simulations. The Journal of Physical Chemistry B. 2007;111(27):7812-24. doi: S1520-6106(07)01097-8.
115. Harder E, Damm W, Maple J, Wu C, Reboul M, Xiang JY, et al. OPLS3: A Force Field Providing Broad Coverage of Drug-like Small Molecules and Proteins. Journal of Chemical Theory and Computation. 2016;12(1):281-96. doi: 10.1021/acs.jctc.5b00864.
116. Sandler SI. An Introduction to Applied Statistical Thermodynamics. USA: John Wiley & Sons, Inc.; 2010. 341 p.
117. Assael MJ, Goodwin ARH, Stamatoudis M, Wakeham WA, Will S. Commonly Asked Questions in Thermodynamics. USA: CRC Press, Taylor & Francis Group; 2011. 346 p.
118. Brooks BR, Brooks CL, Mackerell AD, Nilsson L, Petrella RJ, Roux B, et al. CHARMM: The biomolecular simulation program. Journal of Computational Chemistry. 2009;30(10):1545-614.
119. Phillips JC, Braun R, Wang W, Gumbart J, Tajkhorshid E, Villa E, et al. Scalable molecular dynamics with NAMD. Journal of Computational Chemistry. 2005;26:1781-802. doi: 10.1002/jcc.20289.
120. Feller SE, Zhang Y, Pastor RW, Brooks BR. Constant pressure molecular dynamics simulation: The Langevin piston method. The Journal of chemical physics. 1995;103(11):4613-21. doi: doi:10.1063/1.470648.
121. Martyna GJ, Tobias DJ, Klein ML. Constant pressure molecular dynamics algorithms. The Journal of chemical physics. 1994;101(5):4177-89. doi: doi:10.1063/1.467468.
122. Shaw DE, Bowers KJ, Chow E, Eastwood MP, Ierardi DJ, Klepeis JL, et al., editors. Millisecond-Scale Molecular Dynamics Simulations on Anton. ACM/IEEE Conference on Supercomputing (SC09); 2009; Portland, OR.
123. Shaw DE, Grossman JP, Bank JA, Batson B, Butts JA, Chao JC, et al., editors. Anton 2: Raising the Bar for Performance and Programmability in a Special-Purpose

Molecular Dynamics Supercomputer. SC14: International Conference for High Performance Computing, Networking, Storage and Analysis; 2014 16-21 Nov. 2014.
124. Bowers KJ, Chow E, Xu H, Dror RO, Eastwood MP, Gregersen BA, et al., editors. Scalable Algorithms for Molecular Dynamics Simulations on Commodity Clusters. Proceedings of the ACM/IEEE Conference on Supercomputing; 2006 November 11-17, 2006; Tampa, FL.
125. Lippert RA, Predescu C, Ierardi DJ, Mackenzie KM, Eastwood MP, Dror RO, et al. Accurate and efficient integration for molecular dynamics simulations at constant temperature and pressure. The Journal of chemical physics. 2013;139. doi: doi:10.1063/1.4825247.
126. Klauda JB, Venable RM, Freites JA, O'Connor JW, Tobias DJ, Mondragon-Ramirez C, et al. Update of the CHARMM all-atom additive force field for lipids: Validation on six lipid types. J Phys Chem B. 2010;114(23):7830-43. doi: 10.1021/jp101759q. PubMed PMID: 20496934; PubMed Central PMCID: PMC2922408.
127. Lim JB, Rogaski B, Klauda JB. Update of the Cholesterol Force Field Parameters in CHARMM. The Journal of Physical Chemistry B. 2011;116(1):203-10. doi: 10.1021/jp207925m.
128. Darden T, York D, Pedersen L. Particle mesh Ewald: An N·log(N) method for Ewald sums in large systems. The Journal of chemical physics. 1993;98. doi: doi:10.1063/1.464397.
129. Jo S, Kim T, Iyer VG, Im W. CHARMM-GUI: A web-based graphical user interface for CHARMM. Journal of Computational Chemistry. 2008;29(11):1859-65. doi: 10.1002/jcc.20945.
130. Jo S, Kim T, Im W. Automated Builder and Database of Protein/Membrane Complexes for Molecular Dynamics Simulations. PLOS one. 2007;(9):e880. doi: 10.1371/journal.pone.0000880.
131. Wu EL, Cheng X, Jo S, Rui H, Song KC, Davila-Contreras EM, et al. CHARMM-GUI Membrane Builder toward realistic biological membrane simulations. Journal of Computational Chemistry. 2014. doi: 10.1002/jcc.23702.
132. Pandit KR, Klauda JB. Membrane models of E. coli containing cyclic moieties in the aliphatic lipid chain. Biochimica et biophysica acta. 2012;1818(5):1205-10. Epub 2012/01/26. doi: 10.1016/j.bbamem.2012.01.009. PubMed PMID: 22274566.
133. The PyMOL Molecular Graphics System, Version 1.3, Schrödinger, LLC.: Schrödinger, LLC; 2010.
134. Huang CC, Cough GS, Pettersen EF, Ferrin TE, editors. Chimera: An Extensible Molecular Modeling Application Constructed Using Standard Components. Pacific Symposium on Biocomputing; 1996.
135. Tuller G, Nemec T, Hrastnik C, Daum G. Lipid composition of subcellular membranes of an FY1679-derived haploid yeast wild-type strain grown on different carbon sources. Yeast. 1999;15(14):1555-64. doi: 10.1002/(SICI)1097-0061.

136. Klemm RW, Ejsing CS, Surma MA, Kaiser H-J, Gerl MJ, Sampaio JL, et al. Segregation of sphingolipids and sterols during formation of secretory vesicles at the trans-Golgi network. The Journal of cell biology. 2009;185(4):601-12. doi: 10.1083/jcb.200901145.
137. Jorgensen WL, Chandrasekhar J, Madura JD, Impey RW, Klein ML. Comparison of simple potential functions for simulating liquid water. The Journal of chemical physics. 1983;79. doi: doi:10.1063/1.445869.
138. Hoover WG. Canonical dynamics: Equilibrium phase-space distributions. Physical Review A. 1985;31. doi: http://dx.doi.org/10.1103/PhysRevA.31.1695.
139. Ryckaert J-P, Ciccotti G, Berendsen HJC. Numerical integration of the cartesian equations of motion of a system with constraints: molecular dynamics of n-alkanes. Journal of Computational Physics. 1977;23(3):327–41. doi: 10.1016/0021-9991(77)90098-5.
140. Steinbach PJ, Brooks BR. New spherical-cutoff methods for long-range forces in macromolecular simulation. Journal of Computational Chemistry. 1994;15(7):667-83. doi: 10.1002/jcc.540150702.
141. Klose C, Ejsing CS, Garcia-Saez AJ, Kaiser HJ, Sampaio JL, Surma MA, et al. Yeast Lipids Can Phase-separate into Micrometer-scale Membrane Domains. Journal of Biological Chemistry. 2010;285(39):30224-32. doi: 10.1074/jbc.M110.123554. PubMed PMID: WOS:000281984300059.
142. Shan Y, Klepeis JL, Eastwood MP, Dror RO, Shaw DE. Gaussian split Ewald: A fast Ewald mesh method for molecular simulation. The Journal of chemical physics. 2005;122(5). Epub 2005/03/03. doi: 10.1063/1.1839571. PubMed PMID: 15740304.
143. Im YJ, Raychaudhuri S, Prinz WA, Hurley JH. Structural mechanism for sterol sensing and transport by OSBP-related proteins. Nature. 2005;437(7055):154-8. PubMed PMID: ISI:000231560400060.
144. Martinez L, Andrade R, Birgin EG, Martinez JM. PACKMOL: A package for building initial configurations for molecular dynamics simulations. Journal of Computational Chemistry. 2009;30(13):2157-64. doi: 10.1002/jcc.21224.
145. Berman HM, Westbrook J, Feng Z, Gilliland G, Bhat TN, Weissig H, et al. The Protein Data Bank. Nucleic Acids Reserach. 2000;28(1):235-42. doi: 10.1093/nar/28.1.235.
146. Hunter AD. ACD/ChemSketch 1.0 (freeware); ACD/ChemSketch 2.0 and its Tautomers, Dictionary, and 3D Plug-ins; ACD/HNMR 2.0; ACD/CNMR 2.0. Journal of Chemical Education. 1997;74(8). doi: 10.1021/ed074p905.
147. Humphrey W, Dalke A, Schulten K. VMD: Visual molecular dynamics. Journal of Molecular Graphics. 1996;14(1):33–8. doi: 10.1016/0263-7855(96)00018-5.
148. Vanommeslaeghe K, Hatcher E, Acharya C, Kundu S, Zhong S, Shim J, et al. CHARMM General Force Field: A Force Field for Drug-Like Molecules Compatible with the CHARMM All-Atom Additive Biological Force Fields. Journal of

Computational Chemistry. 2010;31(4):671-90. doi: 10.1002/jcc.21367. PubMed PMID: WOS:000274922000002.
149. Horn HW, Swope WC, Pitera JW, Madura JD, Dick TJ, Hura GL, et al. Development of an improved four-site water model for biomolecular simulations: TIP4P-Ew. Journal Of Chemical Physics. 2004;120(20):9665-78. PubMed PMID: ISI:000221268300028.
150. Subramanian D, Boughter CT, Klauda JB, Hammouda B, Anisimov MA. Mesoscale inhomogeneities in aqueous solutions of small amphiphilic molecules. Faraday Discussions. 2013;167(1):217-38. doi: 10.1039/c3fd00070b.
151. Martínez JM, Martinez L. Packing optimization for automated generation of complex system's initial configurations for molecular dynamics and docking. Journal of Computational Chemistry. 2003;24(7):819-25. doi: 10.1002/jcc.10216.
152. Barber CB, Dobkin DP, Huhdanpaa H. The quickhull algorithm for convex hulls. ACM Transactions on Mathematical Software (TOMS). 1996;22(4):469-83. doi: 10.1145/235815.235821.
153. Kučerka N, Nagle JF, Sachs JN, Feller SE, Pencer J, Jackson A, et al. Lipid bilayer structure determined by the simultaneous analysis of neutron and X-ray scattering data. Biophysical journal. 2008;95(5):2356-67. Epub 2008/05/27. doi: 10.1529/biophysj.108.132662. PubMed PMID: 18502796; PubMed Central PMCID: PMCPmc2517047.
154. Pan J, Marquardt D, Heberle FA, Kucerka N, Katsaras J. Revisiting the bilayer structures of fluid phase phosphatidylglycerol lipids: Accounting for exchangeable hydrogens. Biochimica et biophysica acta. 2014;1838(11):2966-9. doi: 10.1016/j.bbamem.2014.08.009. PubMed PMID: 25135659.
155. Kučerka N, Katsaras j, Nagle JF. Comparing Membrane Simulations to Scattering Experiments: Introducing. Journal of Membrane Biology. 2010;235(1):43-50. doi: 10.1007/s00232-010-9254-5.
156. Lomize MA, Lomize AL, Pogozheva ID, Mosberg HI. OPM: orientations of proteins in membranes database. Bioinformatics (Oxford, England). 2006;22(5):623-5. Epub 2006/01/07. doi: 10.1093/bioinformatics/btk023.
157. Leftin A, Brown MF. An NMR database for simulations of membrane dynamics. Biochimica et biophysica acta. 2011;1808(3):818-39. Epub 2010/12/08. doi: 10.1016/j.bbamem.2010.11.027. PubMed PMID: 21134351.
158. Klauda JB, Roberts MF, Redfield AG, Brooks BR, Pastor RW. Rotation of Lipids in Membranes: Molecular Dynamics Simulation, 31P Spin-Lattice Relaxation, and Rigid-Body Dynamics. Biophysical journal. 2008;94(8):3074-83. doi: 10.1529/biophysj.107.121806. PubMed PMID: 18192349.
159. Shaw DE, al e, editors. Millisecond-Scale Molecular Dynamics Simulations on Anton. ACM/IEEE Conference on Supercomputing (SC09); 2009; Portland, OR.

160. Anisimov MA, Bertrand CE. Thermodynamics of Fluids at Meso and Nano Scales. In: Goodwin ARH, Sengers JV, Peters CJ, editors.: Royal Society of Chemistry; 2010. p. 172-214.
161. Rowlinson JS, Widom B. Molecular Theory of Capillarity. Dover Publications.
162. Pan JJ, Tristram-Nagle S, Nagle JF. Effect of cholesterol on structural and mechanical properties of membranes depends on lipid chain saturation. Physical Review E. 2009;80(2):12. doi: 10.1103/PhysRevE.80.021931. PubMed PMID: WOS:000269637800115.
163. Long RA, Hruska F, Gesser HD. Membrane condensing effect of cholesterol and the role of its hydroxyl group. Biochem Biophys Res Commun. 1970;41(2):321-7.
164. O'Connor JW, Klauda JB. Lipid Membranes with a Majority of Cholesterol: Applications to the Ocular Lens and Aquaporin 0. Journal of Physical Chemistry B. 2011;115(20):6455–64.
165. Sodt AJ, Pastor RW, Lyman E. Hexagonal Substructure and Hydrogen Bonding in Liquid-Ordered Phases Containing Palmitoyl Sphingomyelin. Biophysical journal. 2015;109(5):948-55. doi: 10.1016/j.bpj.2015.07.036. PubMed PMID: 26331252; PubMed Central PMCID: PMCPMC4564825.
166. Matsumori N, Yasuda T, Okazaki H, Suzuki T, Yamaguchi T, Tsuchikawa H, et al. Comprehensive molecular motion capture for sphingomyelin by site-specific deuterium labeling. Biochemistry. 2012;51(42):8363-70. Epub 2012/09/29. doi: 10.1021/bi3009399. PubMed PMID: 23016915.
167. Sada E, Kito S, Yamashita M. Interfacial tensions of two-phase ternary systems. Journal of Chemical and Engineering Data. 1975;20(4):376-7. Epub 2002. doi: 10.1021/je60067a026.
168. Rivas I, Castellanos Suárez AJ, García Sucre M, Urbina Villalba G. Interfacial entropy of tert-butyl alcohol. Interciencia. 2012;37(1):59-64.
169. Paul GW, Chazal LEMd. Interfacial Tensions in Ternary liquid-liquid Systems. Journal of Chemical & Engineering Data. 1967;12(1):105-7.
170. Sada E, Kito S, Yamashita M. Interfacial Tensions of Two-Phase Ternary Systems. Journal of Chemical & Engineering Data. 1975;20(4):376-7.
171. Venable RM, Ingólfsson HI, Lerner MG, Perrin BS, Camley BA, Marrink SJ, et al. Lipid and Peptide Diffusion in Bilayers: The Saffman–Delbrück Model and Periodic Boundary Conditions. The Journal of Physical Chemistry B. 2016. doi: 10.1021/acs.jpcb.6b09111.
172. Ingólfsson HI, Melo MN, van Eerden FJ, Arnarez C, Lopez CA, Wassenaar TA, et al. Lipid Organization of the Plasma Membrane. Journal of the American Chemical Society. 2014;136(41):14554-9. doi: 10.1021/ja507832e.
173. Ohkubo YZ, Pogorelov TV, Arcario MJ, Christensen GA, Tajkhorshid E. Accelerating membrane insertion of peripheral proteins with a novel membrane mimetic model. Biophysical journal. 2012;102(9):2130-9. Epub 2012/07/25. doi:

10.1016/j.bpj.2012.03.015. PubMed PMID: 22824277; PubMed Central PMCID: PMCPMC3341550.
174. Alsop RJ, Maria Schober R, Rheinstadter MC. Swelling of phospholipid membranes by divalent metal ions depends on the location of the ions in the bilayers. Soft matter. 2016;12(32):6737-48. doi: 10.1039/C6SM00695G.
175. López Cascales JJ, Garcia de la Torre J. Effect of lithium and sodium ions on a charged membrane of dipalmitoylphosphatidylserine: A study by molecular dynamics simulation. Biochimica et Biophysica Acta (BBA) - Biomembranes. 1997;1330(2):145-56. doi: http://dx.doi.org/10.1016/S0005-2736(97)00156-9.
176. Böckmann RA, Hac A, Heimburg T, Grubmüller H. Effect of Sodium Chloride on a Lipid Bilayer. Biophysical journal. 2003;85(3):1647-55. PubMed PMID: PMC1303338.
177. Martín-Molina A, Rodríguez-Beas C, Faraudo J. Effect of Calcium and Magnesium on Phosphatidylserine Membranes: Experiments and All-Atomic Simulations. Biophysical journal. 2012;102(9):2095-103. doi: http://dx.doi.org/10.1016/j.bpj.2012.03.009.
178. Tsai H-HG, Lai W-X, Lin H-D, Lee J-B, Juang W-F, Tseng W-H. Molecular dynamics simulation of cation–phospholipid clustering in phospholipid bilayers: Possible role in stalk formation during membrane fusion. Biochimica et Biophysica Acta (BBA) - Biomembranes. 2012;1818(11):2742-55. doi: http://dx.doi.org/10.1016/j.bbamem.2012.05.029.